UKAEA-CCFE-PR(21)35

A R Field, P Carvalho, D Frigione, L Garzotti, Hyun-Tae Kim, M Lenholm, E Lerche, J Mailloux, F Rimini, C M Roach, M Sertoli, G Szepeisi, D van Eester.

The impact of fuelling and W radiation on the performance of high-power, ITER-baseline scenario plasmas in JET-ILW

The impact of fuelling and W radiation on the performance of high-power, ITER-baseline scenario plasmas in JET-ILW

A R Field, P Carvalho, D Frigione, L Garzotti, Hyun-Tae Kim, M Lenholm, E Lerche, J Mailloux, F Rimini, C M Roach, M Sertoli, G Szepeisi, D van Eester.

The impact of fuelling and W radiation on the performance of high-power, ITER-baseline scenario plasmas in JET-ILW

A R Field[1], S Aleiferis[2], É Belonohy[1,3], P Carvalho[4], I Coffey[5],
D Frigione[6], L Garzotti[1], L Horvath[1], Hyun-Tae Kim[1,7],
M Lennholm[8], E Lerche[1,9], P Lomas[1], C G Lowry[8],
J Mailloux[1], F Rimini[1], C M Roach[1], M Sertoli[3], Ž Štancar[10]
G Szepesi[1], D van Eester[9] and JET contributors[*]

EUROfusion Consortium, JET, Abingdon, Oxon, OX14 3DB, UK

[1]CCFE, Culham Science Centre, Abingdon, Oxon, OX14 3DB, UK

[2]NCSR 'Demokritos' 153 10, Agia Paraskevi Attikis, Greece

[3] Max-Planck-Institut für Plasmaphysik, Boltzmannstrasse 2, D-58748, Garching, Germany

[4]IPFN, Instituto Superior Téchnico, Universidade de Lisboa, 1049-001, Lisboa, Portugal

[5]Dept. of Pure and Applied Physics, Queens University Belfast, BT7 1NN, UK

[6]Associazione ENEA, Fusion and Nuclear Safety Department, C R Frascati, Via E. Fermi 45, 00044 Frascati (Roma), Italy

[7]EUROfusion Programme Management Unit, Culham Science Centre, Abingdon, OX14 3DB, UK

[8]European Commission, B-1049 Brussels, Belgium

[9]LPP-ERM-KMS, EUROfusion Consortium Member–Trilateral Euregio Cluster, TEC partner, Brussels, Belgium

[10] Slovenian Fusion Association (SFA), Joseph Stefan Institute, Jamova 39, SI-1000 Ljubljana, Slovenia

[*]see the author list of E. Joffrin et al., Nucl. Fusion **59** (2019) 112021

E-mail: anthony.field@ukaea.uk

Abstract.

Sustained operation of high-performance, ITER-baseline scenario plasmas at the high levels of input power ($\lesssim 40\,\mathrm{MW}$) required to achieve $\sim 15\,\mathrm{MW}$ of D-T fusion power in JET-ILW requires careful optimisation of the fuelling to avoid an unacceptable disruption rate due to excessive radiation, primarily from W impurities, which are sputtered by edge-localised modes (ELMs) from the divertor targets. By using a train of ELM-pacing pellets from a high-frequency pellet injector to promote regular ELMs, which flush W and other impurities from the confined plasma, such high-performance plasmas can be sustained (for $\sim 5\,\mathrm{s}$) while maintaining a high normalised confinement factor $H_{98,y2} \sim 1$, which would otherwise be degraded by reducing the pedestal confinement were a higher rate of D_2 gas fuelling used instead of the pellets to mitigate the W contamination. The causes underlying the improved performance

and energy confinement obtained using this combined, gas and pellet fuelling scheme is investigated here in some detail.

PACS numbers: 52.55.-s, 52.65.-y

Submitted to: *Plasma Phys. Control. Fusion*

1. Introduction

High-performance plasma scenarios are being prepared for the achievement of high levels of fusion power $P_{DT} \lesssim 15\,\mathrm{MW}$ sustained for $\sim 5\,\mathrm{s}$ in a future D-T campaign on JET-ILW. Two different ELMy H-mode scenarios are under preparation: the ITER-baseline scenario operating at $\beta_N \sim 1.8 - 2$ and low edge safety factor $q_{95} \sim 3$ and the hybrid scenario with $\beta_N \sim 2 - 3$ and high $q_{95} \sim 4$ [1]. High input powers of $P_{in} \lesssim 40\,\mathrm{MW}$, primarily from neutral beam injection (NBI) heating are required to achieve such a level of fusion power. Hence, one of the key-performance indicators (KPI) for the current C38 experimental campaign is to achieve a D-D neutron rate $\Gamma_{n,DD} \sim 5 \times 10^{16}\,\mathrm{n/s}$ (equivalent to $P_{DT} \sim 15\,\mathrm{MW}$) sustained for $5\,\mathrm{s}$ in either scenario.

Early experience with high-Z (Mo or W) target materials, e.g. low-density experiments on the PLT tokamak with Mo limiters, showed that core accumulation of only small concentrations $(\sim \mathcal{O}(10^{-4}))$ of such impurities could cause radiative collapse of the plasma [2]. It was later realized that tritium retention by co-deposition onto graphite plasma-facing components (PFCs) would pose an unacceptable hazard in ITER or a reactor, so the use of high-Z PFCs was again revisited, with trials of W as a target material in ASDEX-U [3], leading later to successful demonstration of high-density divertor operation of H-mode plasmas with a full metal wall.

At the $\sim 40\,\mathrm{MW}$ power levels required to demonstrate this KPI in JET-ILW with the all-metal (Be and W) wall, a high fraction of the input power $\mathcal{F}_{Rad} \lesssim 40\%$ is typically radiated, primarily by W impurities in the confined plasma, which are sputtered from the divertor targets by ELMs. Due to the very high emissivity of partially ionized W impurities at electron temperatures in the range $1 - 10\,\mathrm{keV}$, which is $\times \mathcal{O}(50)$ that of any of the other elements in typical plasma facing materials [4], only tiny concentrations of W $C_W (= n_W/n_e) \sim \mathcal{O}(10^{-4})$ are able to radiate this level of power.

Hence, it is essential to take mitigating measures to avoid excessive W impurity erosion from the targets and to prevent accumulation of the W and other high-Z impurities (Ni, Cu & Fe) into the plasma core, where it can result in hollowing of the electron temperature T_e profile and radiation induced disruption of the plasma due to the triggering of tearing modes [5]. Possible mitigation measures, aimed at reducing the W impurity influx by reducing the temperature at the targets, include: sweeping of the strike-point location; increasing the gas fuelling rate and seeding with a low-Z impurity gas, e.g. Ne. Ion-cyclotron-resonance heating (ICRH) is also used to heat the core plasma to mitigate high-Z impurity accumulation [6].

In the baseline scenarios discussed here [1], the strike point location on the outer target is swept radially by $\Delta R \sim 3\,\mathrm{cm}$ at $4\,\mathrm{Hz}$, which is sufficient to prevent excessive local heating of the W coated, graphite tile (T6) and hence avoid melting and vaporisation of the W coating of the carbon-fibre-reinforced graphite (CFC) tiles.

A relatively high level of D_2 gas puffing into the main chamber ($\Gamma_{D2} \sim 2 - 3 \times 10^{22}\,\mathrm{e/s}$) increases the ELM frequency to typically $f_{ELM} \sim 20 - 50\,\mathrm{Hz}$ and hence the rate of W flushing from the confined plasma. Also, the higher particle flux along the scrape-off layer (SOL) increases D^0 recycling in the divertor, reducing T_i at the target and thereby the inter-ELM sputtered W influx.

A deleterious effect of using a higher D_2 puffing rate is to reduce the pedestal temperature [7] by increasing the conducted power across the pedestal between the ELMs [8, 9], which reduces the pedestal pressure [10] and thereby the overall confinement. Increasing the fuelling rate increases the density at the separatrix $n_{e,sep}$ relative to that at the pedestal top $n_{e,ped}$ [11]. This flattens the n_e gradient across the pedestal, reducing the parameter $\eta_e = L_{n_e}/L_{T_e}$, which

provides the drive for turbulent heat transport [12–14]. Also, if the pedestal heat transport is 'stiff', i.e. clamped at a threshold η_e required to destabilise turbulent transport, a consequence is that an increased ratio of separatrix to pedestal density $n_{e,sep}/n_{e,ped}$ would also result in a lower temperature $T_{e,ped}$ at the pedestal top [8].

Ion-cyclotron-resonance heating (ICRH) also has to be used in high-power H-mode JET-ILW discharges, both to avoid core impurity accumulation, particularly during the plasma termination, and to promote an early L/H transition [6, 15]. By using distributed main-chamber fuelling to optimize antenna-plasma coupling, an RF power $P_{RF} \sim 4 - 6$ MW can be routinely coupled into the plasma, minimizing the RF-induced plasma-wall interactions due to sheath-rectification effects.

Central ICRH power deposition and low concentrations of the H^+ minority ions give the best results for core electron heating, achieving absorption efficiencies up to $\sim 90\%$. In these conditions, peaked temperature profiles, together with relatively flat density profiles, allow efficient high-Z impurity screening to be achieved with $P_{RF} \gtrsim 4$ MW.

In spite of these mitigation measures, excessive W radiation can still hamper the achievement of steady, ELMy H-mode operation at high power. Unstable plasma conditions caused by runaway radiation 'events', result in an unacceptably high rate of disruptions, which are particularly dangerous to the device at the high plasma currents ($I_p \sim 3 - 4.5$ MA) typical of the ITER-baseline scenario pulses.

The role of W radiation cooling in the termination of ITER-baseline pulses in JET-ILW has been investigated statistically [5]. Depending on whether the W radiates from the plasma core or periphery, the resulting broadening or shrinking of the current profile, increases the probability of destabilising 2/1 tearing modes, which can induce disruptions. This analysis is used to develop disruption alerts based on T_e-profile shape parameters. Here, we investigate the underlying mechanism of these processes in terms of the behaviour of the W impurities.

The W content of the plasma, and hence the level of radiation, is governed by a balance between the ingress of W impurities from the scrape-off-layer (SOL) by inward neo-classical convection across the pedestal and their removal *aka* 'flushing' from the plasma by ELMs. Too high a fraction of W radiation can dominate the plasma power balance, reducing the ELM frequency, allowing a further increase of the W content. This 'vicious circle' can either trigger an H/L-transition and subsequent W accumulation or cause radiative cooling and MHD-induced collapse from the plasma edge.

Fortuitously, the relatively high plasma current $I_p \sim 3-4.5$ MA of baseline-scenario pulses compared to that of hybrid pulses $\sim 2.2 - 2.3$ MA results in a high pedestal density $n_{e,ped}$ and, consequently, rather flat core n_e profiles, which favours outward neo-classical impurity convection *aka* 'screening', localising the impurities to the peripheral 'mantle' region of the plasma. This screening is not so effective in hybrid scenario pulses, which typically have more peaked n_e profiles.

In hybrid pulses, accumulation of high-Z impurities, triggered by low-n neo-classical tearing modes (NTMs) [16], which are destabilised by the higher poloidal-β, $\beta_p \sim 1.0$ of these plasmas compared to that of baseline pulses ($\beta_p \sim 0.6$), has hampered sustained, high-performance operation. By optimising the gas fuelling during the initial current ramp phase, it has recently been demonstrated that, with sufficient heating power, it is possible to achieve a hot, low collisionality pedestal, resulting in sufficiently strong T_i' across the pedestal to screen out the W from the confined plasma, thereby effectively mitigating this problem [17].

Such unstable, radiative conditions can be avoided by triggering regular ELMs by the injection of a train of small, cryogenic D_2 'ELM-pacing' pellets, thereby maintaining the rate of W flushing from the confined plasma. For this purpose, a high-frequency pellet injector

(HFPI) is available on JET-ILW for injection of both ELM-pacing and fuelling pellets [18,19]. The small ($\sim 2\varnothing$ mm) pacing pellets can be injected at frequencies $f_{Pel} \sim 10 - 45$ Hz from a flight line located at the upper high-field side (HFS) of the main vessel.

Partially replacing some of the gas fuelling by injection of such ELM-pacing pellets, typically resulting in a lower total fuelling rate, is found both to extend the duration of the ELMy H-mode phase and to enhance the overall confinement compared to that achieved with gas fuelling alone [1]. Here, we investigate the underlying causes of both the improved confinement and greater longevity of the high-performance phase of high-power, baseline-scenario pulses obtained using a combination of D_2 gas fuelling and ELM-pacing pellets.

In order to illustrate the effect of the level of gas fuelling on the performance of high-power, ITER-baseline scenario, H-mode pulses in JET-ILW, in §2, we compare the evolution of three similar 3.5 MA pulses with injected heating power $P_{in} \sim 29 - 33$ MW, two with low and high rates of gas fuelling ($\Gamma_{D2} \sim 1.5$ and 2.3×10^{22} e/s) and a third with ELM pacing pellets (at a requested frequency of $f_{Pel} \sim 45$ Hz) with a total fuelling rate from gas puffing and pellets matching that of the pulse with the higher fuelling rate.

In §2.1, kinetic profiles are shown for two of the pulses discussed in §2 to compare the core and pedestal confinement achieved with either gas-fuelling alone or pellet+gas fuelling. In §Appendix A, the effect of the gas fuelling rate and the ELM pacing pellet frequency on the ELMs is quantified by a statistical analysis of their characteristics.

In §2.2, the effect of the fuelling on the core heat and momentum transport is investigated. Ion and electron thermal and momentum diffusivities across the core and pedestal are compared for the two pulses discussed in §2.1, which are obtained from an interpretive transport analysis using TRANSP. Further, detailed results on the ion and electron power balances and the momentum balance are presented in §Appendix C.

In §2.3, the effect of this ELM flushing on the W content and the evolution of the total radiation is investigated. Firstly, in §2.4, the method used to quantify the W flushing by the ELMs, based on an analysis of fast bolometric measurements of the radiated power, is explained. Results from application of this analysis to a high-power, gas-fuelled 3 MA pulse #92432, which also exhibits a core W accumulation 'event', are presented in §2.5. In §2.6 results of the ELM-flushing analysis from the pulses discussed in §2 are then compared.

By classifying the ELMs as either 'pellet-triggered' or spontaneous, 'natural' events, we can investigate the influence of the ELM type on the their efficiency of flushing out the W impurities. In §2.7, a statistical analysis of the ELM flushing and inter-ELM ingress of W, is presented, classifying the data by ELM type.

As the ELM-sputtered, 'intra-ELM' W impurity source dominates that during the inter-ELM periods, in §2.8 we compare relative intra-ELM Be and W impurity fluences $\Phi_{Be,W}$, i.e. the influxes integrated over the ELM duration, for the different ELM types. These are evaluated from visible Be II and W I line intensities from a multi-channel spectrometer viewing the divertor targets.

To determine whether any of the improvements in plasma performance caused by modification of the W behaviour is induced by the pellets, the effect of the pacing pellets on the inter-ELM evolution of the kinetic profiles (and associated gradient parameters) in the pedestal and mantle regions is investigated in §2.9.

In the discussion §3, the main results from each section are first summarised in §3.1, then in §3.2 we propose a mechanism for the interaction of fuelling, ELMs and W impurities in high-power, ITER-baseline pulses, which is applied to understanding the radiation event in pulse #92432 in §3.3. The possible influence of fuelling on the retention of sputtered impurities in the divertor is discussed in §3.4.

Finally in §4, we present the main conclusions of this study and an outlook to future work. Some detailed material, supplementary to each of the preceding sections is presented in Appendices A-F.

2. Comparison of high-power, 3.5 MA pulses with different fuelling sources

To illustrate the importance of optimising the particle fuelling in achieving maximal energy confinement (and hence fusion yield) and pulse duration at high-performance, in this section, the evolution of three, 3.5 MA ITER-baseline (BL) scenario pulses with 29-33 MW of additional heating power are compared. Two of these, #94915 and #94980 have low and high rates of D_2 gas fuelling during the sustained H-mode phase of $\Gamma_{D2} \sim 1.5$ and 2.3×10^{22} e/s respectively from gas-inlet modules (GIMs) at octants #1, 6 & 8) in the main chamber. The other pulse #96713 has both D_2 gas fuelling at a low rate of $\sim 1.0 \times 10^{22}$ e/s and D_2 ELM-pacing pellets. The key parameters of these three pulses are given in Table 1 and a comparison of their evolution is shown in Fig. 1.

Pulse	P_{in}	$\Gamma_{D2} \times 10^{22}$ [s^{-1}]			f_{Pel}	$W_{th,max}$	$\Gamma_{n,DD}$	Δt_{HP}	C_{min}	
#	[MW]	Gas	Pellet	Total	[Hz]	[MJ]	10^{16} [s^{-1}]	[s]	H [%]	^3He [%]
94915	28	1.5	-	1.5	-	8.8	2.2	~ 1	~ 1.5	-
94980	29	2.3	-	2.3	-	7.5	1.2	~ 3	~ 1	~ 2.5
96713	33	1.0	1.3	2.3	45-35	10.5	3.5	~ 3	~ 3	-

Table 1: *Parameters of analysed* 3.5 MA/3.3 T *ITER-baseline scenario pulses, showing: total heating power* P_{in}*; fuelling rates* Γ_{D2} *from gas puffing, pacing pellets and total; the requested ELM-pacing pellet frequency* f_{Pel}*; peak plasma stored energy* $W_{pl,max}$*; peak D-D neutron rate* $\Gamma_{n,DD}$*; duration of 80% peak-performance, ELMy H-mode phase* Δt_{HP}*; and the concentrations* C_{min} *of H and* ^{3}He *minority ions for the ICRH.*

The D_2 pellets used for triggering, *aka* 'pacing' ELMs on JET-ILW have dimensions $\varnothing$ 2 mm and length ~ 2 mm with an average particle content $\Phi_{D2,pel} \sim 3 \pm 0.2 \times 10^{20}$ e/pellet, measured by the last microwave cavity along the flight tube. At the requested pellet rate of $f_{Pel} \sim 45$ Hz for pulse #96713, this results in a time-averaged fuelling rate into the vessel of $\Gamma_{D2,pel} \sim 1.3 \pm 0.2 \times 10^{22}$ e/s. As shown in Fig. 1 (b), the resulting total, time-averaged fuelling rate from the gas and pellets $\Gamma_{D2} = \Gamma_{D2,gas} + \Gamma_{D2,pel} \sim 2.2 \times 10^{22}$ e/s almost matches that in pulse #94980 with the higher rate of gas fuelling alone.

Although the thermal stored energy W_{th} is somewhat higher ($\sim 15\%$) in pulse #94915 than in pulse #94980 with the higher fuelling rate, i.e. ~ 8.8 MJ c.f. ~ 7.5 MJ, as shown in Fig. 1 (e) pulse #94915 is non-stationary, exhibiting complex ELM behaviour, with some large, type-I ELMs, each followed by a period of small ELMs and then a long ELM-free phase of duration ~ 0.2 s. During the final ELM-free, H*-phase, the radiated power fraction $\mathcal{F}_{Rad}$ (see Fig. 1 (a)) increases to $\gtrsim 40\%$ of the input power, at which point this triggers a controlled termination of the pulse, which commences with a strong increase of the gas puffing rate (not shown).

Stronger gas puffing into the main chamber is required to achieve steady operation, e.g. as in pulse #94980, resulting in more frequent, smaller amplitude, type-I ELMs, some of which are followed rapid bursts of small, type-III ELMs and subsequent, shorter H*-phases, as shown in Fig. 1 (f). A relative measure of the time-averaged ($\tau_{sm} = 0.25$ s) ELM-sputtered Be II influx $\langle \Gamma_{Be} \rangle \propto \langle I_{BeII} \rangle$ shown in the figure (cyan), indicates that the impurity source is, on-average,

probably not very different to that in the non-stationary pulse #94915. However, the more frequent ELMs manage to expel sufficient of the highly radiative W impurities to maintain $\mathcal{F}_{Rad} \lesssim 30\%$ (see Fig. 1 (a)). Statistical analysis of the response of the ELM characteristics to the gas puffing rate and the pellet injection frequency is presented in §Appendix A.

The achievement of sustained, ELMy H-mode operation at high-power with the stronger gas puffing does, however, come at the cost of reduced pedestal temperature and, consequently, lower overall energy confinement (see Ref. [8] and references therein.) The effect of the different fuelling on the pedestal parameters in these pulses is quantified in §2.9 below. In terms of the normalised confinement, as shown in Fig. 1 (c), the H-mode confinement enhancement factor $H_{98,y2}$ † is reduced by the stronger gas puffing to ~ 0.8 c.f. ~ 1.0 in pulse #94915, while the input power in these two pulses is similar $P_{in} \sim 29\,\mathrm{MW}$.

Note that, although the rates and method of fuelling are different, the achieved, line-average density $\bar{n}_e \lesssim 0.8 \times 10^{20}\,\mathrm{m}^{-3}$ (corresponding to a Greenwald density fraction $f_{GW} = \bar{n}_e/n_{e,GW} \lesssim 0.7\ddagger$) is similar in these three pulses. The line-averaged, effective ion charge $Z_{eff} \sim 1.6$, inferred from a horizontal mid-plane, visible bremsstrahlung measurement, is also similar for the three pulses.

As shown in Fig. 1 (d), the $\sim 50\%$ reduction in the D-D neutron rate $\Gamma_{n,DD}$ caused by the increased gas puffing rate in pulse #94980 is more severe than the reduction in thermal energy, the former being $\Gamma_{n,DD} \lesssim 1.0 \times 10^{16}\,\mathrm{n/s}$ c.f. $\lesssim 2.0 \times 10^{16}\,\mathrm{n/s}$ in pulse #94915. This is a consequence of the lower peak ion temperature $T_{i,0} \sim 6\,\mathrm{keV}$ in pulse #94980 compared to $\sim 8\,\mathrm{keV}$ in pulse #94915 and the fact that the Maxwell-averaged rate coefficient $\langle \sigma_{DD} \rangle$ increases strongly with temperature (approximately $\propto T_i^2$) [20].

The injection of ELM-pacing pellets to trigger ELMs in conditions which would otherwise result in long H*-phases (and potentially a high disruptivity) offers a means of extending the duration of the high-performance, ELMy H-mode phase, whilst maintaining the high pedestal temperature and overall confinement that is achieved at lower gas fuelling rates. In the pulse #96713 the gas fuelling rate of $\Gamma_{D2,gas} \sim 1.0 \times 10^{22}\,\mathrm{e/s}$ is lower than that in pulse #94915 but the total fuelling rate, including that from the 45 Hz pellets is close to that from the gas puffing alone in #94980.

As shown in Fig. 1 (g), this combined fuelling scheme results in higher frequency, lower amplitude ELMs, even than those in the pulse #94980 with the higher fuelling rate. Although most but not all pellets trigger ELMs, the statistical analysis presented in §Appendix A shows that the overall ELM frequency does not lock to the pellet frequency. Instead, there are typically bursts of small amplitude, high-frequency ELMs that follow the pellet triggered ELMs, resulting in a higher average ELM frequency than that of the pellets.

As a result of the small ELM amplitude, the time-averaged, relative ELM-sputtered Be II influx $\langle \Phi_{Be} \rangle$ is lower than in either of the other two pulses with the gas fuelling alone. In spite of this, the radiated power fraction $\mathcal{F}_{Rad} \lesssim 40\%$ is higher than in the high-gas pulse #94980, lying just below that required to trigger an early pulse termination by the safety interlock. Note that the duration of the pulse with gas and pellets #96715 is not limited by a high radiation fraction or W accumulation but by the control system, which was programmed to commence pulse termination by strongly increasing the gas puffing rate at 52 s.

† The H-mode confinement enhancement factor $H_{98,y2}$ is defined as the ratio of the thermal energy confinement time $\tau_{E,th}$ to the energy confinement time $\tau_{E,98y2}$ from the ITER $H_{98,y2}$ energy confinement scaling [21], i.e. $H_{98,y2} = \tau_{E,th}/\tau_{E,98y2}$.
‡ The Greenwald density is defined as $n_{e,GW} = I_p/(\pi a^2)$, where I_p is the plasma current in MA and a is the geometrical minor radius in m
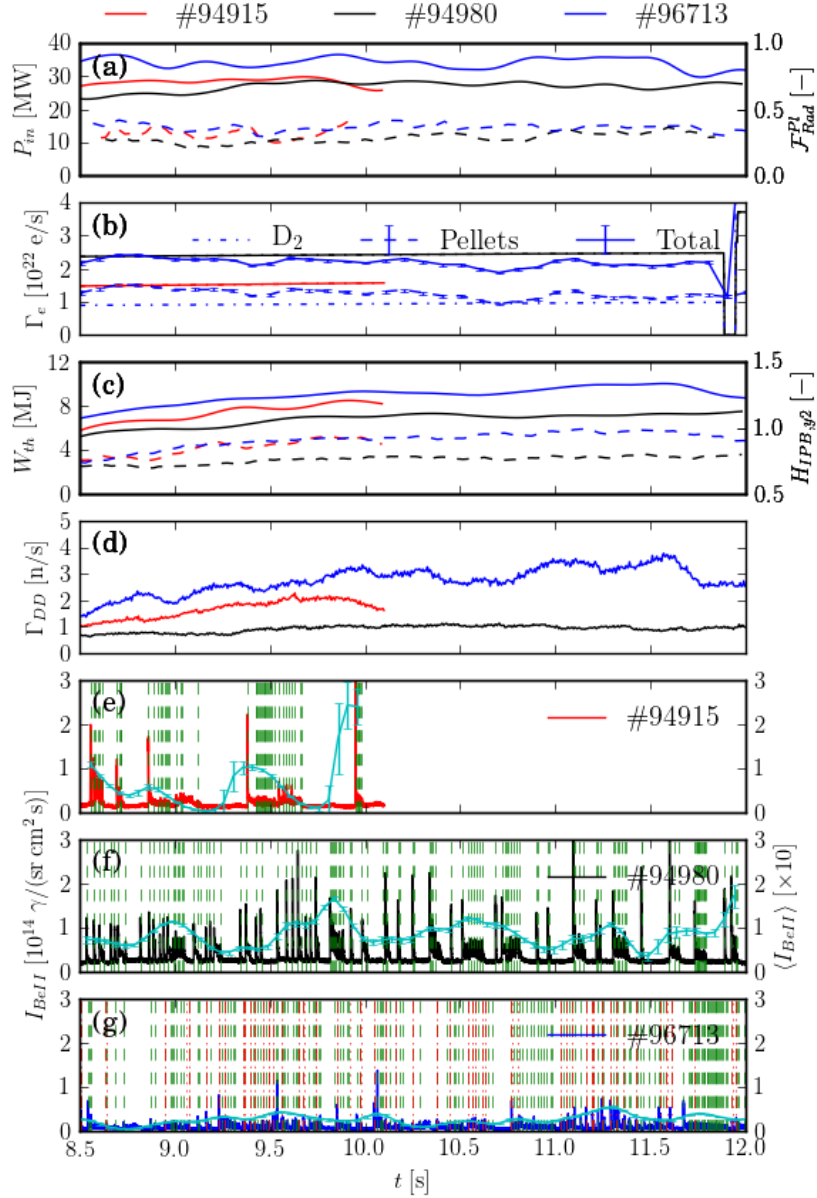
Figure 1: *Comparison of evolution of* 3.5 MA/3.3 T *ITER-baseline scenario pulses with different fuelling sources #94915 (red), #94980 (black) and #96713 (blue) with the key parameters given in Table 1 showing: (a) total absorbed additional heating power P_{abs} and radiated power fraction $\mathcal{F}_{Rad} = P_{Rad}/P_{abs}$; (b) fuelling rates Γ_{D2} [e/s] from D_2 gas $\Gamma_{D2,gas}$ (dot-dashed), pacing pellets $\Gamma_{D2,pel}$ (smoothed, $\tau_{sm} = 0.25$ s) (dashed) and total fuelling rate $\Gamma_{D2} = \Gamma_{D2,gas} + \Gamma_{D2,pel}$ (solid); (c) total MHD stored energy W_{th} (solid) and H-mode confinement enhancement factor $H_{98,y2}$ (dashed); (d) total D-D neutron rate $\Gamma_{n,DD}$; (e-g) the ELM behaviour from a visible Be II line viewing the outer divertor target, where the smoothed ($\tau_{sm} = 0.25$ s), intra-ELM integrated signal $\langle I_{BeII} \rangle$ is also shown (cyan, ×10) and the ELM peaks are marked by the vertical lines (natural ELMs (dashed/green) & pellet triggered ELMs (red/dot-dashed)).*

The pulse #96713, with gas and pellet fuelling, has a higher input power of 33 MW, i.e. $\sim 15\%$ more than the ~ 29 MW in the pulses with gas puffing alone. The resulting stored energy $W_{th} \lesssim 10.5$ MW is relatively higher than in the two gas-fuelled pulses with low and high puffing rates, in which $W_{th} \sim 8.8$ MW and ~ 7.5 MW respectively. The confinement enhancement factor $H_{98,y2}$, which offers a means of comparing the quality of confinement taking into account the difference in heating power, is restored to the same level in the pulse #96713 with gas and pellets to that in the low-gas pulse #94915, i.e. $H_{98,y2} \lesssim 1.0$.

Remarkably, at the same stage of the pulse, the D-D neutron rate is considerably higher ($\sim \times 1.5$) in pulse #96713 with the pellets and gas than in the low-gas pulse #94980. In the next section §2.1, we show that this can be attributed to a higher axial ion temperature $T_{i,0}$, which may result from increased rotational shear across the core plasma due to an overall higher toroidal rotation rate Ω_ϕ. The enhanced rotation in pulse #96713 may in part arise from the $\sim \times 1.1$ higher rotation at the pedestal top $\Omega_{\phi,ped}$ (see Table 2 and Fig. 7 (f)) below).

It is conjectured that the increase in Ω_ϕ at the plasma periphery would reduce charge-exchange (CX) friction with neutral D^0 atoms due to the lower rate of main-chamber gas puffing used in #96713. As the pellets provide $\sim 50\%$ of the fuelling and are injected at the HFS, while the main-chamber gas puffing at the low-field side (LFS) is reduced, a lower D^0 density at the LFS would result in less frictional drag on the plasma [22].

2.1. Comparison of energy confinement in pulses #94980 and #96713

A beneficial effect of operating at a reduced gas fuelling rate with the ELM pacing pellets is an enhancement of the core energy confinement, which is associated with increased toroidal rotation and reduced ion temperature gradient stiffness [23]. A comparison of kinetic profiles averaged over a 2 s period of the ELMy H-mode phase of the 3.5 MA ITER-baseline pulses #94980 with only gas fuelling and pulse #96713 with pellets+gas fuelling is shown in Fig. 2. As stated previously in §2, these pulses have similar total fuelling rates of $\Gamma_{D2} \sim 2.3 \times 10^{22}$ e/s, however, the pulse #96713 has only $\sim 43\%$ of the gas fuelling rate $\Gamma_{D2,gas}$ of #94980.
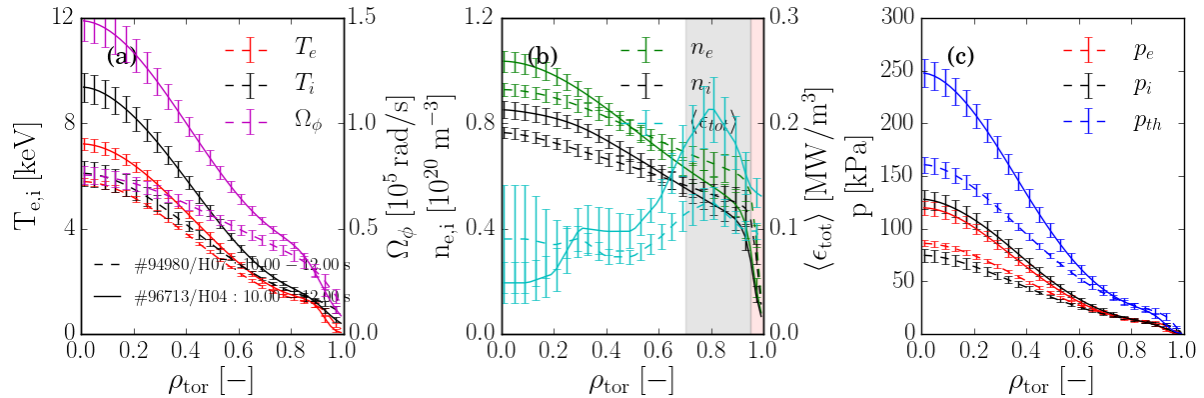

Figure 2: *Comparison of fitted, time-averaged kinetic profiles for the three pulses shown in Fig. 1 #94915 (low gas fuelling rate) and #94980 (high gas fuelling rate) and #96713 (pellet and gas fuelling, with total rate matched to that for #94980) showing radial profiles vs ρ_{tor} of: (a) ion and electron temperatures $T_{i,e}$ and toroidal rotation Ω_ϕ rates: (b) ion and electron densities $n_{i,e}$ and flux-surface averaged total emissivity $\langle \epsilon_{tot} \rangle$; (c) ion, electron $p_{i,e}$ and total thermal p_{th} pressures. The radial coordinate $\rho_{tor} = \sqrt{\Phi_N}$, where Φ_N is the normalised toroidal magnetic flux.*

These profiles are from an interpretive transport analysis using the TRANSP code [24], which is based on input kinetic profiles which are mapped onto the radial coordinate $\rho_{tor} = \sqrt{\Phi_N}$, where Φ_N is the normalised toroidal flux using a pressure-constrained, magnetic equilibrium obtained from the EFIT++ equilibrium reconstruction code [25, 26]. More details of the TRANSP run, including the origin of the input data and the assumptions made are given in §Appendix C.

It can be seen from Fig. 2 (a), that across the core plasma, both the ion temperature T_i and the toroidal rotation rate Ω_ϕ are higher in the pellet+gas-fuelled pulse #96713 than in the gas fuelled pulse #94980, on-axis by factors of ~ 1.5 and ~ 2 respectively. However, at the pedestal top, these parameters are approximately equal. It should be noted that the additional heating power P_{in} is $\sim \times 1.13$ higher in #96713 than in pulse #94980.

Average values of pedestal parameters over the high-performance, ELMy H-mode phase for the same 3.5 MA pulses as in Table 1 are stated in Table 2. Note that, in spite of the $\sim \times 2$ higher fuelling rate in pulse #94980 as in pulse #96713, the pedestal temperatures for the two pulses are quite similar. However, there are significant differences in the edge rotation and density, with lower $\langle n_{e,ped} \rangle$ by $\sim \times 0.8$ and lower relative separatrix density $\langle n_{e,sep} \rangle / \langle n_{e,ped} \rangle$ by $\sim \times 0.9$ but higher $\langle \Omega_{\phi,ped} \rangle$ by $\sim \times 1.1$ in #96713 with the pellet+gas fuelling compared to those in #94980.

Pulse	$t_0 \rightarrow t_1$	$\langle T_{e,ped} \rangle$	$\langle n_{e,ped} \rangle$	$\langle T_{i,ped} \rangle$	$\langle \Omega_{\phi,ped} \rangle$	$\frac{\langle n_{e,sep} \rangle}{\langle n_{e,ped} \rangle}$
#	[s]	[keV]	$[\times 10^{20} m^{-3}]$	[keV]	$[\times 10^5 r/s]$	[-]
94915	8.5-10.0	0.78±0.02	0.52±0.02	1.17±0.03	23.1±0.8	0.18±0.03
94980	10.0-12.0	0.81±0.01	0.59±0.01	1.07±0.02	21.9±0.5	0.23±0.01
96713	10.0-12.0	0.76±0.03	0.48±0.01	1.00±0.02	24.3±0.6	0.20±0.01

Table 2: *Average pedestal parameters over the high-performance, ELMy H-mode phase of the same three pulses (#94915, #94980 & #96713) for which key parameters are stated in Table 1 over the period $t_0 \rightarrow t_1$. Further details of how these parameters are determined are given in §2.9. Note that the value of $\Omega_{\phi,ped}$ is that of Ω_ϕ at the top of the n_e pedestal, while the density ratio $n_{e,sep}/n_{e,ped}$ is determined by assuming a fixed value of $T_e \sim 100$ eV at the separatrix.*

Density profiles of the electrons and D^+ ions are shown in Fig. 2 (b). Although $n_{e,ped}$ is $\sim \times 1.1$ higher in the gas-fuelled pulse #94980 than in the pellet+gas fuelled pulse #96713, the line-averaged density $\bar{n}_e$ is the same in both pulses, so the density profile is somewhat more peaked in the pellet+gas fuelled pulse #96713, with $\bar{n}_e/n_{e,ped} \sim 1.67$ compared to ~ 1.35 in #94980. The effect of the lower pedestal density with the pellet+gas fuelling on the power and momentum deposition from the neutral-beam-injection (NBI) heating is discussed in detail in §Appendix C.

Also shown in Fig. 2 (b) are profiles of the flux-surface averaged total emissivity $\langle \epsilon_{tot} \rangle$ from tomographic reconstructions [27] of multi-chord, bolometric measurements of the total radiation [28]. In the peripheral, 'mantle' region (defined here as $0.7 \leq \rho_N \leq \rho_{N,ped} \sim 0.96$), we see that $\langle \epsilon_{tot} \rangle$ is $\lesssim \times 1.8$ higher in the pellet+gas fuelled pulse #96713 than in the gas-only fuelled pulse #94980, which is consistent with the higher concentration of W in the mantle (see Fig. 7) (a), which is the dominant radiator in such high-power H-mode pulses in JET-ILW. The effect of this strong mantle radiation on the ion and electron power balance is also discussed in §Appendix C.1 (see also §4 of Ref. [8]).

Finally, we see from Fig. 2 (c), that on-axis, the total thermal pressure p_{th} is $\sim \times 1.5$ higher in pulse #96713 than in pulse #94980, primarily due to the higher ion temperature

$T_{i,0}$, which is $\sim \times 1.5$ higher in #96713, while $T_{e,0}$ is only $\sim \times 1.23$ higher than in pulse #94980. The average volume-integrated, total stored energies $\langle W_{th} \rangle$ and those of the ions and electrons $\langle W_e \rangle$ and $\langle W_i \rangle$, obtained from the TRANSP runs for these pulses are stated in Table 3, together with the corresponding, averaged pedestal stored energies.

Pulse	$\langle W_{th} \rangle$	$\langle W_e \rangle$	$\langle W_i \rangle$	$\langle W_{th,ped} \rangle$	$\langle W_{e,ped} \rangle$	$\langle W_{i,ped} \rangle$	$\langle P_i/P_e \rangle$	$\frac{\langle W_i \rangle}{\langle W_e \rangle}$
#	[MJ]	[MJ]	[MJ]	[MJ]	[MJ]	[MJ]	[-]	[-]
94980	6.53 ± 0.02	3.18 ± 0.01	3.35 ± 0.01	2.00 ± 0.04	0.88 ± 0.02	1.12 ± 0.03	1.18 ± 0.06	1.05 ± 0.01
96713	8.54 ± 0.05	3.71 ± 0.02	4.84 ± 0.03	1.52 ± 0.03	0.64 ± 0.02	0.88 ± 0.02	1.33 ± 0.07	1.31 ± 0.01

Table 3: *Thermal stored energies (total and of either ions or electrons) of the whole plasma and that due to the pressures at the pedestal top, averaged over the period $50.0 \rightarrow 52.0s$ during the high-performance, ELMy H-mode phase of the two pulses (#94980 & #96713) for which key parameters are stated in Table 1. Also stated are the time-averaged ratios of total ion to electron heating power $\langle P_i/P_e \rangle$ and thermal energies of the ions and electrons $\langle W_i \rangle / \langle W_e \rangle$.*

From these stored energies in Table 3, we see that on-average, the pedestal energy $\langle W_{th,ped} \rangle$ is $\sim \times 1.3\%$ higher in the gas fuelled pulse #94980 than in the pellet+gas fuelled pulse #96713, primarily due to the higher $n_{e,ped}$ in the former. However, the total stored energy $\langle W_{th} \rangle$ is $\sim \times 1.3$ higher in pulse #96713, which has $\sim \times 1.13$ higher input power than pulse #94980. Comparing the ratios of the components of the total thermal energy stored in the ions to that in the electrons, we see that $\langle W_i \rangle / \langle W_e \rangle \sim 1.3$ is higher in pulse #96713 compared to ~ 1.05 in #94980.

This relative increase in ion energy confinement cannot be explained solely by an increase in the average ratio of ion to electron heating $\langle P_i/P_e \rangle$, which is higher in pulse #96713 compared to that in pulse #94980 by a factor ~ 1.12. Hence, there is also a relative improvement of the ion energy confinement with the pellet+gas fuelling compared to that with gas fuelling alone. The reason for this is discussed in more detail in section §2.2, in which the effect of the changes to the fuelling between pulses #94980 and #96713 on the ion and electron heat transport and the transport of toroidal angular momentum L_ϕ across the core plasma is investigated.

2.2. Comparison of core heat and momentum transport in pulses #94980 and #96713

The time-dependent, interpretive TRANSP analysis solves the balance equations for the transport of particles, ion and electron heat and toroidal momentum [24, 29], which are described for the power and momentum balances in more detail in §Appendix B. The source of kinetic profiles (T_e, n_e, T_i, Ω_ϕ and $\langle \epsilon_{tot} \rangle$) and other input data, the magnetic equilibrium used for mapping the profiles onto normalised radius ρ_{tor} and other assumptions in setting up the runs, e.g. on the impurity densities, are described in detail in §Appendix C.

A comparison of results from the solution of the power balances of the ions and electrons and of toroidal momentum are shown in Fig. 3 for the pulses #94980 with gas-fuelling alone and #96713 with pellet+gas fuelling, where the profile data is averaged over a 2 s period of the ELMy H-mode phase. Note that results of the power and momentum balances for these two pulses are described in more detail in §Appendix C.

It can be seen from Fig. 3 (a), that across the core plasma the normalised gradients R/L_{T_e}, R/L_{T_i} and R/L_{Ω_ϕ} are all larger in pulse #96713 than in pulse #94980, with R/L_{T_i} and $R/L_{T_i} \sim \times 1.5$ higher and $R/L_{\Omega_\phi} \sim \times 2$ higher at mid-radius. This increase is a signature
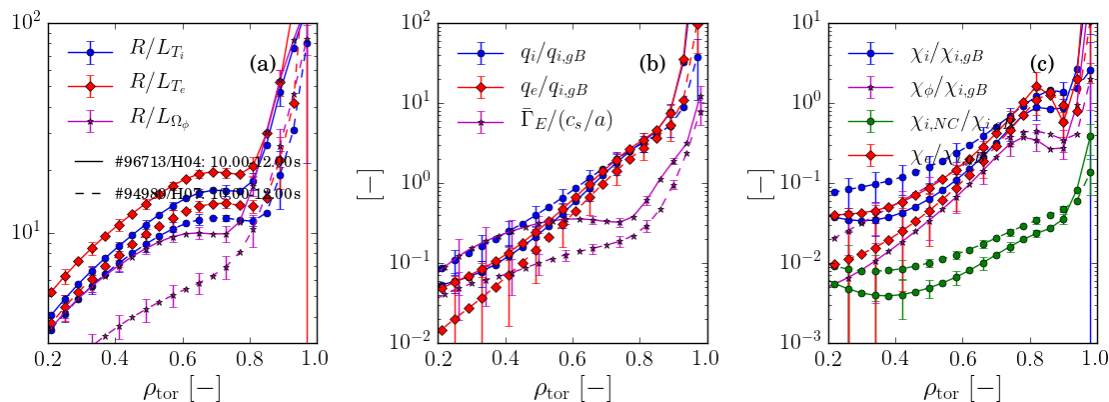
Figure 3: *Results of interpretive, TRANSP power balance analyses of JET-ILW pulses #94980 (H07, dashed) and #96713 (H04, solid) showing time-averaged profiles over the ELMy H-mode phase of: (a) the normalised gradients R/L_{T_e} ($\blacklozenge$) and R/L_{T_i} ($\bullet$) and of toroidal rotation R/L_{Ω_ϕ} ($\star$); (b) the electron and ion heat fluxes $q_e/q_{i,gB}$ ($\blacklozenge$) and $q_i/q_{i,gB}$ ($\bullet$) normalised to the ion gyro-Bohm level $q_{i,gB}$ and the normalised E×B shearing rate $\bar{\gamma}_E = \gamma_E/(c_s/a)$ (c_s is the sound speed) ($\star$); and (c) thermal diffusivities of the electrons $\chi_e/\chi_{i,gB}$ ($\blacklozenge$), ions $\chi_i/\chi_{i,gB}$ ($\bullet$) and the ion neo-classical diffusivity $\chi_{i,NC}/\chi_{i,gB}$, all normalised to the ion-gyro-Bohm thermal diffusivity $\chi_{i,gB}$.*

of improved energy and momentum confinement, particularly in the ion channel across the core plasma in the pellet+gas fuelled pulse.

The heat fluxes in the ion and electron channels $q_i/q_{i,gB}$ and $q_e/q_{i,gB}$, normalised to the ion-gyro-Bohm heat flux $q_{i,gB}$ are plotted in Fig. 3 (b)§. For pulse #96713 with gas+pellet fuelling, these normalised heat fluxes are almost equal with $q_i \sim q_e$ right across the core plasma. In contrast, for the gas fuelled pulse #94980, while $q_i \sim q_e$ in the mantle region ($0.7 \leq \rho_{tor} \leq 1$), deeper into the core plasma q_i progressively exceeds q_e, with $q_i/q_e \lesssim 10$ in the core.

The normalised, perpendicular $E \times B$ shearing rate $\bar{\gamma}_E = \gamma_E/(c_s/a)$ ‖, also shown in Fig. 3 (b), is considerably higher in pulse #96713 than in pulse #94980, by up to a factor ~ 3 at mid-radius. This shearing can suppress the amplitude of ion-scale turbulence when $\bar{\gamma}_E \gtrsim \mathcal{O}(1)$ [32, 33], thereby reducing the associated heat flux. Hence, it is likely that $E \times B$ shear plays a more significant role in regulating the level of turbulent ion heat transport in pulse #96713, in which $\bar{\gamma}_E \lesssim 0.3$ at mid-radius, than in pulse #94980.

Thermal diffusivities for the ion and electron channels, normalised to the ion-gyro-Bohm thermal diffusivity, $\chi_i/\chi_{i,gB}$ and $\chi_e/\chi_{i,gB}$ are compared in Fig. 3 (c) for the same two pulses, together with the normalised diffusivity of the toroidal angular momentum $\chi_\phi/\chi_{i,gB}$. These quantities are defined in terms the relevant power and momentum fluxes and profile gradients in §Appendix C. Also shown is an estimate of the gyro-Bohm normalised, neo-classical (NC) ion thermal diffusivity $\chi_{i,NC}/\chi_{i,gB}$, which is calculated in TRANSP using the NCLASS code [34].

It can be seen from Fig. 3 (c) that for both pulses, in the peripheral mantle region the normalised thermal diffusivities of the ions and electrons are approximately equal, i.e. $\chi_i/\chi_e \sim 1$. For pellet+gas fuelled pulse #96713 this is also the case right across the core

§ The ion gyro-Bohm heat flux is defined here as $q_{i,gB} = -n_i \chi_{i,gB} T_i'$, where the associated heat diffusivity $\chi_{i,gB} = v_{th,i}\rho_i^2/L_{T_i}$ and $v_{th,i} = \sqrt{2T_i/m_i}$ [21, 30].
‖ The parameter c_s/a, where c_s is the sound speed and a the minor radius, is an estimate for the typical growth rate γ_{lin} of ion-scale turbulence [30].)

plasma. In contrast, for the gas fuelled pulse #94980, further into the plasma χ_i progressively exceeds χ_e, with $\chi_i/\chi_e \lesssim 10$ in the core. In both pulses these thermal diffusivities far exceed the ion neo-classical level, with both $\chi_{i,e}/\chi_{i,NC} \sim \mathcal{O}(10)$. This certainly indicates that ion-scale turbulent transport is by no means fully suppressed in either pulse.

In both pulses, the Prandtl number $Pr = \chi_\phi/\chi_i$ decreases from $Pr \sim 0.5$ at $\rho_{tor} \sim 0.7$ both deeper into the core plasma and outward across the pedestal region, which is an indication that there is some degree of suppression of ion-scale turbulence (which results in stronger viscosity than electron scale turbulence) in the core and peripheral regions.

These results suggest that ion-scale transport (ITG or TEM) turbulence, which can result in both ion and electron heat transport with equal efficacy, is primarily responsible for the core heat transport in both pulses. However, in the higher performance pulse #96713 with pellet+gas fuelling, at least some of the increased ion pressure in the core may be caused by a modest relative reduction in the efficiency of ion-scale, turbulent heat transport, caused by the increased $E \times B$ flow shear across the core plasma.

In spite of the fact that in both pulses the integrated heating power to the ions is approximately equal at mid-radius, the $\sim \times 3$ higher χ_i in the gas fuelled pulse #94980 results in lower core T_i gradient and hence reduced core ion energy confinement than in the pellet+gas fuelled pulse #96713. This is a consequence of the more peaked ion heating and torque deposition profiles resulting from the reduced pedestal density with the pellet+gas fuelling compared to that with the gas fuelling alone (see §Appendix C).

2.3. W impurity behaviour in 3.5 MA baseline pulses

In high-power ITER-baseline scenario pulses with $\gtrsim 25$ MW of heating power, a substantial fraction of the input power is radiated from the core plasma, i.e. $\mathcal{F}_{Rad} \sim 30 - 40\%$. It has been shown in Ref. [8] that these losses are dominated by radiation from W impurities, which accounts for $\gtrsim 95\%$ of the total radiation. In such pulses, these impurities are typically localised to the outer 'mantle' region ($0.7 \leq \rho_N \leq \rho_{N,ped} \sim 0.96$) of the confined plasma, e.g. as shown for the 3 MA pulse #92432 with 32 MW heating power in Fig. E1 (a). The radially outward centrifugal force due to the toroidal rotation localises the heavy W ions to the LFS mid-plane where the total emissivity ϵ_m peaks [36]. However, because of the very high parallel electron thermal conductivity $\chi_{e,\parallel} >> \chi_e$, it is the flux-surface-averaged emissivity $\langle \epsilon_{tot} \rangle$ that is relevant to the electron power balance (see Fig. 2 (b)).

The reason why the impurity ions tend to remain localised to the mantle region in these ITER-baseline pulses is because the density gradient across the core plasma is much weaker than that of the ion temperature, i.e. there is a low degree of density peaking. As is discussed in Ref. [8] and references therein, the radial neo-classical convection velocity of impurity ions is proportional to the parameter $\zeta_{NC} = R/2L_{T_i} - R/L_{n_i}$ [37]. Hence, a *peaked* T_i profile and a *flat* n_e profile favours outward neo-classical convection, expelling the impurities from the plasma core. The converse is also true and, particularly in 'hybrid' scenario plasmas [1], which operate with a lower pedestal density $n_{e,ped}$ and consequently with a more peaked n_e profile, this can cause the W impurities to accumulate in the plasma core and lead to radiation collapse.

The evolution of the flux-surface-averaged W impurity density $\langle n_W \rangle$ is shown in Fig. 4,(a-c) for the three 3.5 MA ITER-baseline pulses discussed in §2, from which it can be seen that the W is typically localised to the mantle region, i.e. $0.7 \leq \rho_{tor} \leq 1$. Only in one of these pulses #94980 is there a brief period during which $\langle n_W \rangle$ peaks in the plasma core but these impurities are expelled again later.
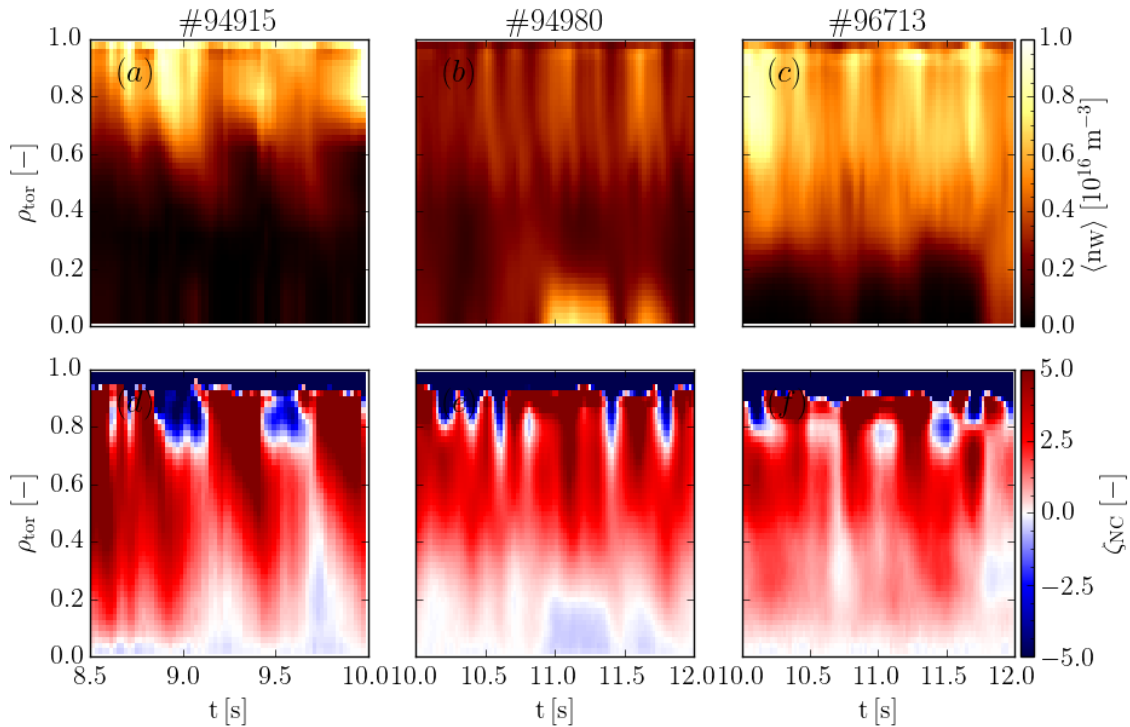
Figure 4: *Comparison for the three* $3.5\,\mathrm{MA}/3.3\,\mathrm{T}$ *ITER-baseline scenario pulses with different fuelling #94915 (a, d), #94980 (b, e) and #96713 (c, f) shown in Fig. 1 of: (a-c) the flux-surface-averaged W impurity density* $\langle n_W \rangle$ *(top); and (d-f) the neo-classical convection parameter* ζ_{NC} *(bottom), both as a function of* ρ_{tor}*. For #94980 and #96713 the W density is determined from the integrated analysis of Ref. [74], while for #94915 it is determined by assuming W radiation dominates the total emissivity from bolometer tomography, i.e. that* $\langle n_W \rangle = \langle \epsilon_{tot} \rangle / (n_e \mathcal{R}_\epsilon)$*, where* $\mathcal{R}_\epsilon \sim 4.5 \times 10^{-13}\,\mathrm{Wm^3}$ *is the total emissivity coefficient of W in the mantle region.*

Also shown in Fig. 4 (d-f) is a comparison of the evolution of profiles of the neo-classical convection parameter ζ_{NC}. This is calculated from the results of an interpretive TRANSP calculation, which is based on kinetic data provided from fits to electron density n_e and temperature T_e profile data measured by the high-resolution Thomson scattering system [38] and Ne^{10+} impurity ion temperature T_i and toroidal rotation Ω_ϕ profile data from the core and edge CXRS systems [39].

From these plots it can be seen that, while $\zeta_{NC} \sim \mathcal{O}(-100)$ is strongly negative in the pedestal region (off the color scale), hence driving the impurities across the pedestal into the confined plasma, it is weakly positive $\zeta_{NC} \gtrsim 5$ right across the core of the plasma. Consequently, once inside the confined plasma, the impurities are screened from the core plasma by outward convection, which concentrates them in the outer mantle region. Note that the convection velocity $V_{NC} \propto Zq^2 D_c \zeta_{NC}/R$, where Z is the impurity ion charge and D_c is the collisional diffusivity [37]. Typically, the W ions are in charge states W^{25-30+} in the mantle region (see Fig. 5 (c)), so this convection is strong for the W ions. Also, the strong polodial asymmetry enhances the convection by a further factor $1/(2\epsilon^2) \sim 5$, where the inverse aspect ratio $\epsilon = r/a$ [40].

Note that there are circumstances in these high-power, ITER-baseline pulses in which profile changes following an H- to L-mode transition, triggered by the strong W radiation

from the plasma periphery, causes a sudden accumulation of the impurities. This typically leads to termination of the high-performance phase, either triggering a 'pulse stop' or causing a disruption due to radiation collapse. Such a radiation event occurs in the 3 MA pulse #92432, the phenomenology of which is described in §2.5.

Note that in pulse #94915, during the periods of ELM-free H*-mode, radiative cooling of the mantle region by the increasingly strong W radiation together with a concomitant increase in density, causes stronger outward convection ($\zeta_{NC} >> 0$), localising the W to the plasma periphery. However, during the subsequent periods with rapid type-III ELMs, the resulting increase in the n_e gradient in the mantle causes this convection to reverse ($\zeta_{NC} < 0$), thereby allowing the W impurities to penetrate deeper in to the plasma, although they do not accumulate in the core.

While the W impurities are localised to the mantle region by the outward neo-classical convection, they can be efficiently expelled from the confined plasma by the ELMs. The ELMs typically expel a small fraction of the plasma particles, peeling off part of the pedestal plasma, causing relative density losses $\Delta \bar{n}_e / \bar{n}_e \sim 5 - 10\%$. If the impurities are concentrated in the periphery, the ELMs can 'flush' out a larger relative fraction of the impurity content than that of the main ions.

We define here the flushing efficiency of the W impurities by an ELM as $(\Delta \bar{n}_W / \bar{n}_W)_{ELM}$, i.e. the relative change in the W content of the plasma due to the ELM. Because the total radiation in high-power, JET-ILW pulses is dominated by that from W, this flushing efficiency can be evaluated from fast, bolometric measurements of the total radiation from the confined plasma, as described in detail in the following section §2.4.

2.4. Evaluation of ELM W 'flushing' efficiency

An estimate of the efficacy of each ELM at flushing the W impurities from the confined plasma (and also their influx during the inter-ELM periods) can be obtained from an analysis of fast, bolometric total radiation measurements, using a method first applied to JET-ILW plasmas described in Ref. [41]. For this analysis we use a fast radiated power signal P_{Rad}^{Hor} calculated from a weighted sum of intensities from a bolometer camera viewing the main chamber horizontally from the LFS [28].

As shown in Fig. 5 (b) for the high-power, 3 MA ITER-baseline pulse #92432, the total emissivity coefficient of W is reasonably constant over the mantle region ($0.7 \leq \rho_N \leq \rho_{N,ped} \sim 0.96$), i.e. $\mathcal{R}_\epsilon \sim 4.5 \times 10^{-31}$ MWm^3, where the W radiates most intensely (see Fig. 5 (a)). Typically, in the mantle region, where $T_e \sim 1 - 3$ keV, the average charge state $\bar{Z}$ of the impurities is W^{25-30+}. The atomic data shown in Fig. 5 is from the ADAS database of spectroscopic data [42] and uses total radiated line power ($\mathcal{PLT}$) data for W from Ref. [43].

As the W radiates mainly from the mantle region and the emissivity of W is reasonably constant over the relevant temperature range (1-3 keV), the average W density $\bar{n}_W$ in the mantle can be estimated from the expression: $\bar{n}_W \sim P_{Rad}^{man} / (\bar{n}_e \mathcal{R}_\epsilon V_{man})$, where $\bar{n}_e$ is the average density over the mantle region and V_{man} is the volume of the mantle ~ 22 m^3. We next explain how we obtain a fast enough signal P_{Rad}^{man} quantifying the radiated power from the mantle region to determine the ELM flushing efficiency, which requires a frequency response of order 1 kHz.

The power radiated from the confined plasma P_{Rad}^{Pl} can be calculated from a weighted sum of horizontally viewing, line-integrated measurements of total intensity measured using a multi-chord bolometer system [28]. This system has a sample rate of 5 kHz and uses an adaptive filtering algorithm so as not to smooth fast transients due to ELMs, while having lower
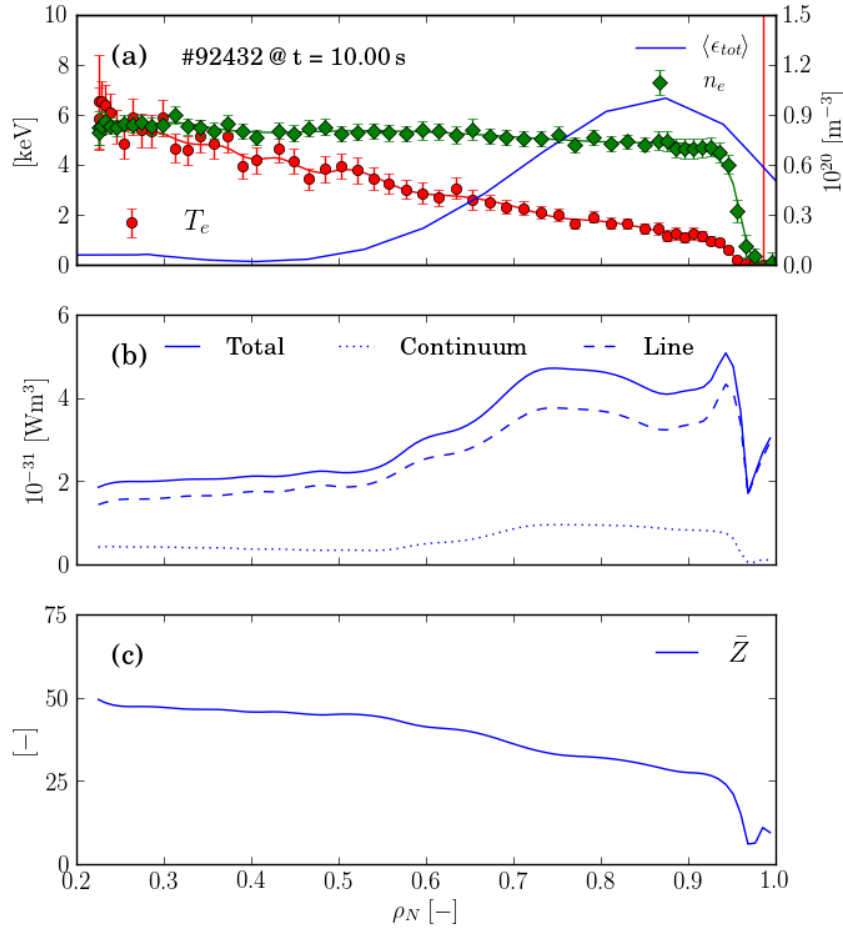
Figure 5: *Profiles for the high-power, JET-ILW pulse #92432 at 10 s of: (a) electron temperature T_e (●) and density n_e (◆) measured by high-resolution Thomson scattering and flux-surface averaged, total emissivity $\langle \epsilon_{tot} \rangle$ from bolometer tomography (solid-blue); (b) emissivity coefficients $\mathcal{R}_\epsilon$ for W radiation (total-solid, line-dashed and continuum-dotted) from ADAS [42, 43]; and (c) mean ionic charge $\bar{Z}$ of W, where coronal ionisation balance is assumed for the W atomic data.*

bandwidth of typically 0.2 kHz during steady phases. As this calculation relies on assumptions on the symmetry of the emissivity on flux surfaces, it tends to overestimate P_{Rad}^{Pl} by as much as 50% in the presence of highly in-out asymmetric emissivity distributions. Here, we refer to this fast radiated power signal as P_{Rad}^{Hor}.

In order to overcome this problem and accurately calculate the radiated power from the mantle region P_{Rad}^{man}, we use the total emissivity distribution $\epsilon_m(R, z)$ obtained from tomographic inversion [27] of the multi-chord bolometer data, which take proper account of the poloidal asymmetry. Reconstructions are calculated at the mid-times of each inter-ELM period, using input data averaged over 5 ms intervals. The resulting distributions are integrated over the volume of the mantle to form a 'slow' radiated power signal we refer to here as $\langle P_{Rad}^{man} \rangle$. Note that in these high-power, ITER-baseline scenario pulses, typically $\sim 70\%$ of the radiated power is emitted from the mantle region (see Fig. 6 (c)).

We can correct the fast radiated power signal P_{Rad}^{Hor} to provide a more accurate, fast

estimate of P_{Rad}^{man} by scaling it to the more accurate, slow signal $\langle P_{Rad}^{man} \rangle$ obtained from the tomography using a time-dependent scale factor. While this procedure may seem complicated, it is necessary if we are to use the resulting values of P_{Rad}^{man} to estimate the concentration of W in the mantle region. The algorithm used to perform this time-dependent scaling of the signal is described in §Appendix D.

From both the fast estimate of the radiated power from the mantle P_{Rad}^{man} and a fast measurement of the line-average density $\bar{n}_e$ from the lower, horizontal interferometer channel (#5), which passes through the outer half of the lower plasma cross-section, the ELM W flushing efficiency can be evaluated from the change in the signal $f_{fl} = P_{Rad}^{Hor}/\bar{n}_e$ between short averaging periods just before and after the ELM crash, i.e. from the expression $\Delta n_W/n_W \sim (f_{fl}^{pre-ELM} - f_{fl}^{post-ELM})/f_{fl}^{pre-ELM} = \Delta(f_{fl})/f_{fl}^{pre-ELM}$.

For our analysis we use pre- and post averaging times of $\Delta t_{ELM} = \{-7, -2\,\mathrm{ms}\}$ and $\{5, 10\,\mathrm{ms}\}$ relative to the time t_{ELM} of the peak Be II intensity signal. The post-ELM time period is delayed by $5\,\mathrm{ms}$ to avoid the transient increase in radiation that is caused by the ELM-sputtered W influx before the ionisation balance has had time to recover.

A similar measure, estimating the relative change in the W content between the ELMs, i.e. the relative inter-ELM ingress or 'fluence' of W $(\Delta\bar{n}_W/\bar{n}_W)_{i-ELM}$ can be calculated from the difference between the post-ELM value of f_{fl} and that prior to the subsequent ELM, i.e. $(\Delta\bar{n}_W/\bar{n}_W)_{i-ELM} = (f_{fl}^{pre-ELM_{i+1}} - f_{fl}^{post-ELM_i})$. These measures of the ELM W flushing efficiency $(\Delta\bar{n}_W/\bar{n}_W)_{ELM}$ and the relative, inter-ELM fluence $(\Delta\bar{n}_W/\bar{n}_W)_{i-ELM}$ can then be used to calculate net rates of change of the W impurity content, $\gamma_W = (d\bar{n}_W/dt)/\bar{n}_W$ from a time-dependent average, as described in Appendix B of Ref. [45].

In the case of a group of rapid ELMs, with an inter-ELM period shorter than the pre- and post-ELM averaging times of $\{-7, 10\,\mathrm{ms}\}$, it is only possible to determine the flushing for the group of ELMs, which we choose to split equally between the sub-ELMs, while the inter-ELM fluence is allocated to the last in the group. A property of this ad-hoc method of handling the compound ELMs does maintain valid, time-averaged flushing rates γ_W calculated from the $\Delta\bar{n}_W/\bar{n}_W$ data. Rates of change of the W content due to the ELM flushing γ_W^{ELM} and the inter-ELM influx γ_W^{i-ELM} are shown in Fig. 7 (c) of §2.6 below, together with the 'net' rate of change due to the balance between these competing fluences, i.e. $\gamma_W^{net} = \gamma_W^{ELM} - \gamma_W^{i-ELM}$.

By availing of fact that radiation from W dominates the radiated power and that the total emission rate coefficient $\mathcal{R}_\epsilon$ of W over the $1-3\,\mathrm{keV}$ temperature range in the mantle region is almost constant $\sim 4.5 \times 10^{-31}\,\mathrm{Wm}^3$, the average W concentration over the mantle region $\langle C_W \rangle_{man}$ can also be estimated from the expression: $\langle C_W \rangle_{man} \sim P_{Rad}^{man}/(V_{man}\mathcal{R}_\epsilon\bar{n}_e^2)$. Typically, $\langle C_W \rangle_{man} \sim 2 - 3 \times 10^{-4}$ in these plasmas, e.g. as shown in Fig. 6 (a).

An example of the application of this ELM-flushing analysis to the the high-power, $3\,\mathrm{MA}$ ITER-baseline pulse #92432 is presented in the following section §2.5.

2.5. ELM W flushing and 'radiation event' in pulse #92432

The evolution of the high-power, $3\,\mathrm{MA}$ ITER-baseline pulse #92432 with $32\,\mathrm{MW}$ of additional heating power and gas fuelling only at a rate of $\Gamma_{D2} \sim 2.3 \times 10^{22}\,\mathrm{e/s}$, is shown in Fig. 6 both as an example of the application of the ELM W flushing analysis described above but also to illustrate the profound effect that the strong W radiation can have on the evolution of such high-power H-mode pulses in JET-ILW.

Provided the W impurities remain primarily in the outer, mantle region of the plasma, their effect on the core fusion performance is relatively benign and their radiation helps distribute the power exhaust over the vessel walls. For this situation to persist, two criteria

must be satisfied: firstly, the ELMs must flush out enough of the W that crosses the separatrix between ELMs to maintain a constant impurity content; secondly, the T_e and n_e gradients in the mantle must stay aligned such that the impurity convection is directed outwards, i.e. $\langle \zeta_{NC} \rangle_{man} > 0$, so that the W impurities are screened from the plasma core.

During the early ELMy phase of the pulse ($\lesssim 10\,\text{s}$) these conditions are fulfilled, however, later the ELM frequency slows and they then cease at $\sim 10.2\,\text{s}$. During the subsequent,
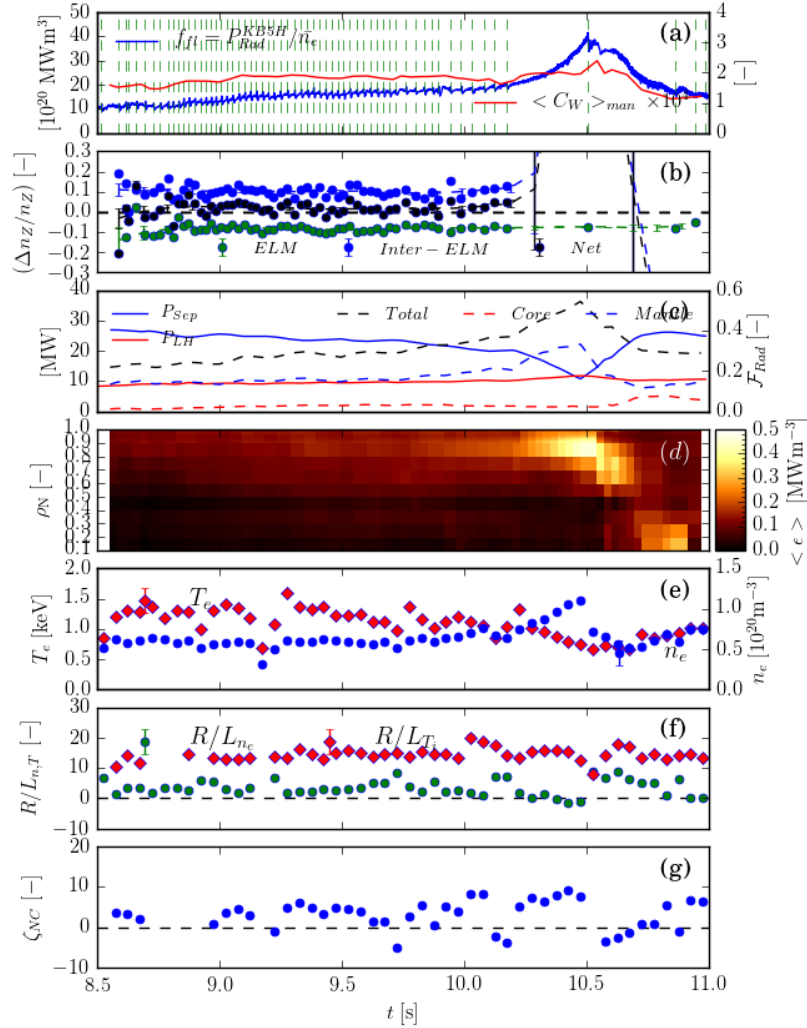
Figure 6: *The evolution of JET-ILW pulse #92432 illustrating the effect of W radiation on the mantle: (a) the signal $f_{fl} = P_{Rad}^{Hor}/\bar{n}_e$ (blue), the average W concentration in the mantle $\langle C_W \rangle_{man}$ (red) and the ELM times (red dashed); (b) the relative changes to the W content in the mantle $\Delta n_W/n_W$ caused by ELM flushing (red), the influx between ELMs (blue) and the net change over the ELM cycle (black); (c) the separatrix loss power $P_{Sep} = P_{in} - P_{Rad}^{Pl}$ (blue-solid) and the L/H-transition threshold power P_{LH} [44]; and the fractions of radiated power $\mathcal{F}_{Rad}$ (RHS-dashed) from the confined plasma (black), the mantle (blue) and the core ($\rho_N \leq 0.5$) (red); (d) the flux-surface averaged emissivity $\langle \epsilon_m \rangle (\rho_N)$; (e) the electron temperature T_e (♦) and density n_e (•) at $\rho_N = 0.9$; and (f) the neo-classical convection parameter $\langle \zeta_{NC} \rangle_{man}$ averaged over the mantle region.*

ELM-free H*-phase, the density $\bar{n}_e$, W content ($\bar{n}_W \propto P_{Rad}^{man}/\bar{n}_e$) and the associated radiation primarily from the mantle increase strongly, to a fraction $\mathcal{F}_{Rad} \gtrsim 70\%$ of the input power (see Fig. 6 (c)). The slowing of the ELMs prior to the H*-phase is caused by an increase in the gas puffing rate by the control system, which is intended to *increase* f_{ELM}, i.e. this has the opposite effect to that expected. The phenomenology of these events is discussed further in §3.

The consequent reduction of the net power crossing the separatrix $P_{Sep} = P_{l,th} - P_{Rad}^{Pl}$ below L/H-transition threshold power P_{LH} [44] triggers a subsequent back transition to L-mode (see Fig. 6 (c)).

As shown in Fig. 6 (f, g), the resulting peaking of the n_e profile due to the loss of the density pedestal after the transition to L-mode results in a sudden reduction of the neo-classical screening ($\zeta_{NC} \to 0$). As is evident from the evolution of the total emissivity $\langle \epsilon_{tot} \rangle$ shown in Fig. 6 (d) this reduction in screening then causes sudden accumulation of the W impurities the plasma core, resulting in a reduction of the stored energy W_{pl} by $\sim 30\%$.

The influence of the strong mantle radiation on the electron power balance is evident from Fig. 6 (e), which shows that there is a significant reduction of T_e just inside the pedestal top (at $\rho_{tor} = 0.9$) and a corresponding increase of n_e as the level of mantle radiation increases (see Ref. [8] for a detailed discussion of the electron and ion power balance in this pulse).

The resulting changes to the n_e and T_e gradients in the mantle initially causes $\langle \zeta_{NC} \rangle_{man}$ to increase (see Fig. 6 (f)), driving the impurities more strongly outwards. At the H/L-transition at 10.5 s, $\langle \zeta_{NC} \rangle_{man}$ suddenly decreases to ~ 0, when the normalised density gradient R/L_{n_e} in the mantle region steepens, causing the W impurities to rush into in the plasma core. This behaviour is evident from the evolution of the total emissivity distribution $\langle \epsilon_{tot} \rangle$, which is shown in Fig. 6 (d).

During the ELMy H-mode phase, as shown in Fig. 6 (a), while the W concentration in the mantle ($\langle C_W \rangle_{man} \sim P_{Rad}^{man}/(V_{man}\mathcal{R}_\epsilon \bar{n}_e^2)$) remains quite constant at $\langle C_W \rangle_{man} \sim 2 \times 10^{-4}$, there is a gradual increase in the W content $\bar{n}_W \propto P_{Rad}^{man}/\bar{n}_e$, causing a concomitant increase in the mantle radiation P_{Rad}^{man} (see Fig. 6 (c)). This gradual increase is a result of a delicate balance between the flushing of the W impurities by the ELMs from the confined plasma and their influx across the pedestal between the ELMs.

The W flushing efficiency $\Delta\bar{n}_W/\bar{n}_W$ and inter-ELM W fluence $(\Delta\bar{n}_W/\bar{n}_W)_{i-ELM}$ evaluated for each ELM are shown in Fig. 6 (b), together with the net, relative change in the W content over each ELM cycle, i.e. $(\Delta\bar{n}_W/\bar{n}_W)_{net} = (\Delta\bar{n}_W/\bar{n}_W)_{i-ELM} - (\Delta\bar{n}_W/\bar{n}_W)_{i-ELM}$. It is evident that, while $\sim 5-10\%$ of the W content is flushed by each ELM, a similar amount is convected across the pedestal from the SOL and re-enters the plasma between the ELMs. The small, net change results in a gradual change on a timescale $1/\gamma_W^{net} \sim \mathcal{O}(1\,\text{s})$.

In this pulse, ELMy H-mode does resume at the end of the period shown but the high-Z impurities remain in the plasma core and the stored energy does not fully recover to the level prior to the radiation event. The use of ELM-pacing pellets in such pulses alters the characteristics of the ELMs and allows the duration such high-performance, ITER-baseline pulses to be extended. The behaviour of 3.5 MA ITER-baseline, H-mode pulses with ELM pacing pellets is discussed in the following section §2.6.

2.6. *ELM flushing and W behaviour in* 3.5 MA *pulses*

In this section, we investigate the ELM flushing and W behaviour in the three 3.5 MA ITER-baseline pulses with different gas and/or pellet fuelling that we discussed previously in §2. Results of the ELM W flushing analysis for these pulses are presented in Fig. 7.

Considering first, the pulse #94915 with the lower rate of gas fuelling ($\Gamma_{D2,gas} \sim 1.5 \times 10^{22}$ e/s) alone, we see that this pulse is non-stationary, exhibiting three H*-phases, during which the mantle W radiation increases, just as occurred in pulse #92432, described in §2.5 above. The W concentration of W in the mantle $\langle C_W \rangle_{man} \sim 2 \times 10^{-4}$ is similar in both of these gas-only fuelled pulses.

The strong mantle radiation does not result in an H/L-transition as in pulse #92432, instead the H*-phase is terminated by a single large amplitude ELM, which is followed by a
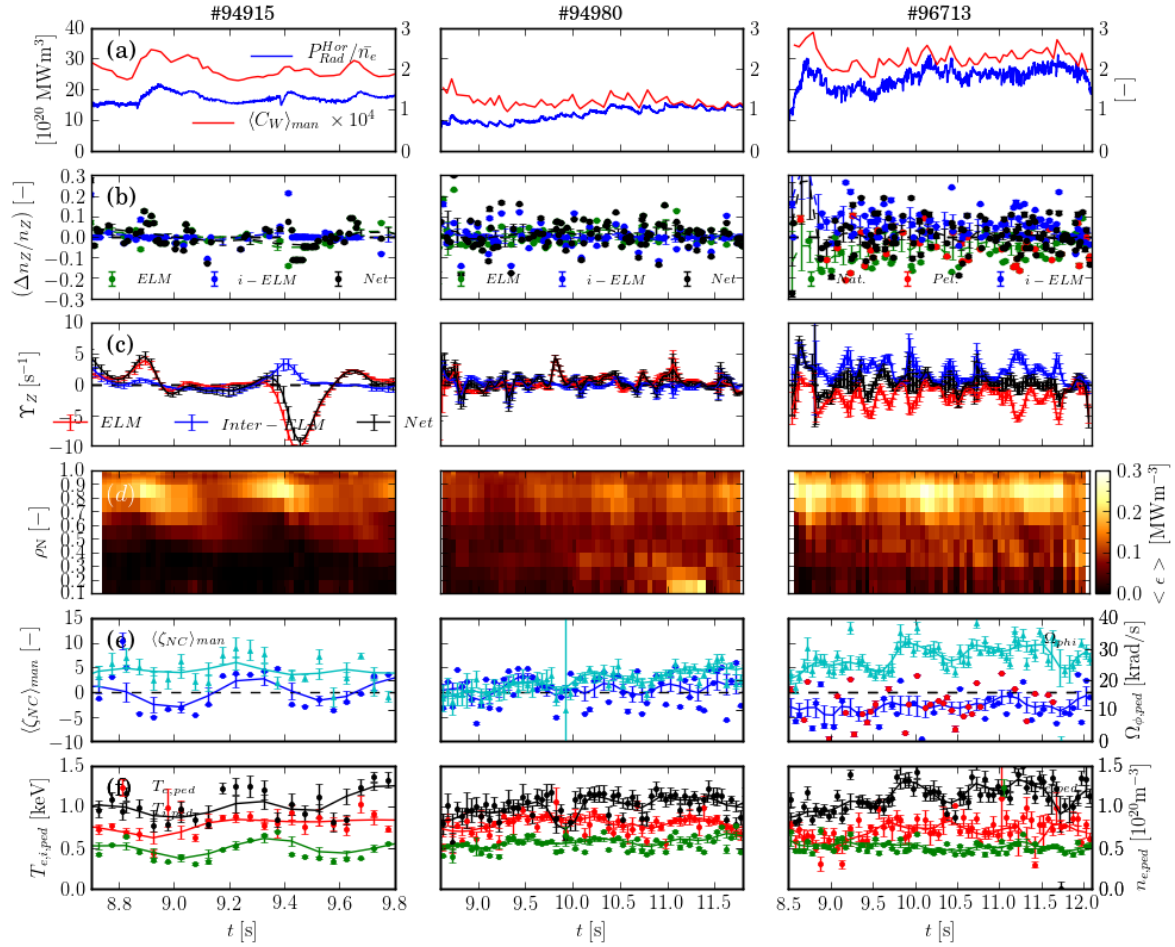
Figure 7: *A comparison for the three high-power,* $3.5\,\mathrm{MA}/3.3\,\mathrm{T}$ *baseline-scenario JET-ILW pulses of Fig. 1 (key parameters given in Table 1), showing the evolution of: (a) the signal* $f_{fl} = P_{Rad}^{Hor}/\bar{n}_e$ *(blue) and the estimated average W concentration over the mantle region* $\langle C_W \rangle_{man}$ *(red); (b) the fraction of W flushed per ELM* $(\Delta \bar{n}_W/\bar{n}_W)_{ELM}$ *for natural (•) and pellet-triggered (•) ELMs, the inter-ELM W influx* $(\Delta \bar{n}_W/\bar{n}_W)_{i-ELM}$ *(•) and the net fractional change in W content per ELM cycle (•); (c) the respective rates of change of the W content* $\gamma_W = d(\Delta \bar{n}_W/\bar{n}_W)/dt$ *due to the ELM flushing (*γ_W^{ELM}*– red), the inter-ELM influx (*γ_W^{i-ELM}*–blue) and the resulting net rate of change (*γ_W^{net}*–black), (d) the flux-surface-averaged total emissivity* $\langle \epsilon_{tot} \rangle$ *from bolometry; (e) the neo-classical convection parameter* $\langle \zeta_{NC} \rangle_{man}$ *averaged over the mantle region (blue & •, •following pellet-triggered ELMs) and the toroidal rotation rate* $\Omega_{\phi,ped}$ *(▲) measured by CXRS at the top of the density pedestal; and (f) the electron* $T_{e,ped}$ *(•) and ion* $T_{i,ped}$ *(•) pedestal temperatures and the pedestal density* $n_{e,ped}$ *(•).*

sustained burst of small, type-III ELMs (see Fig. 1 (e)). During these phases, the n_e gradient in the mantle region increases, resulting in a reversal of the neo-classical convection from outward to inward, as shown in Fig. 7 (e). This reversal allows the W to migrate deeper into the plasma core, as is evident from the evolution of the total emissivity shown in Fig. 7 (f)), however, the impurities do not accumulate in the plasma core.

The combined effect of the few, large and frequent, small ELMs does provide sufficient flushing of the W to maintain a reasonably constant W concentration. However, during the final H*-phase, a strong increase of the total radiated power P_{Rad}^{tot} triggered an early 'pulse-stop', which initiated an increase in the gas fuelling rate. During the ramp-down phase of this pulse, there was a disruption, resulting in vessel forces exceeding 350 T. This non-stationary nature of high-power, ITER-baseline pulses with a low rate of gas fuelling leads to a high fraction of pulses disrupting, which is clearly unacceptable.

Increasing the D_2 gas puffing rate, as in pulse #94980 ($\Gamma_{D2,gas} \sim 2.3 \times 10^{22}$ e/s), provides a safe means of controlling the W impurity level, and thereby reducing the disruptivity, but at the cost of decreased energy confinement. The more frequent ELMs induced by the increased gas puffing flush out more W, significantly reducing the W concentration to $\langle n_W \rangle_{man} \sim 1 - 1.5 \times 10^{-4}$. Note, however, that there is a gradual buildup of the W content due to the increasing $\bar{n}_e$ (see Fig. 7 (a)). The W impurities are also not so well screened from the core because of the reduced core T_i and hence weaker R/L_{T_i}, resulting in the neo-classical convection parameter $\zeta_{NC} \sim 0$ in the mantle region.

Comparison of the pedestal parameters shown in Fig. 7 (e,f), shows that the increased gas puffing in pulse #94980 does not significantly reduce $T_{e,ped}$, or indeed increase $n_{e,ped}$, compared to those in pulse #94915. There is, however, a significant reduction in toroidal rotation rate $\Omega_{\phi,ped}$ at the top of the density pedestal caused by the increased gas puffing rate in pulse #94980. In both pulses, the ion temperature $T_{i,ped}$, here defined as T_i at the top of the density pedestal¶, is significantly higher ($\sim 20\%$) than $T_{e,ped}$.

As already discussed above, the use of ELM-pacing pellets in pulse #96713 allows the duration of the high-performance phase to be extended without degrading the energy confinement. The main beneficial effect of the pellets is to trigger regular ELMs under conditions which would otherwise result in ELM-free H*-phases, as occur in pulse #94915. This allows pulse #96713 to be run with an even lower gas puffing rate ($\Gamma_{D2,gas} \sim 1.0 \times 10^{22}$ e/s) than that used in pulse #94915 ($\sim 1.5 \times 10^{22}$ e/s). The danger with such a strategy is that we rely on reliable operation of the pellet injector to deliver a regular stream of pellets for the pulse to run without risk of a radiation induced disruption.

Although the total D_2 fuelling rate from gas and pellets, i.e. $\Gamma_{D2} \sim 2.3 \times 10^{22}$ e/s, is the same in pulse #96713 as used in pulse #94980, the performance is of the pulse is superior in terms its the overall energy confinement. We will see that the origin of this lies not in significantly higher $T_{e,ped}$ but in increased toroidal rotation and hence rotational shear from the pedestal top, inwards across the core plasma and hence increased core ion energy confinement.

From Fig. 7 (a), we can see that the W concentration of $\langle C_W \rangle_{man} \sim 2.5 \times 10^{-4}$ is in fact as high in pulse #96713 as in pulse #94915. As evident from the evolution of the total emissivity shown in Fig. 7 (d), the W is also not as well screened from the plasma core as in pulse #94915. Averaged over the mantle region, the neo-classical convection parameter is

¶ As the ion temperature from the edge CXRS system typically does not exhibit a clear 'knee' at the pedestal, we do not fit the profile with an mtanh() function [46] as is done for the T_e profile but instead take the pedestal value of T_i to be that at the top of the n_e pedestal.

slightly negative $\zeta_{NC} \sim -20$, i.e. weakly inwards (see Fig. 7 (e)). However, the full radial profiles shown in Fig. 4 (b), show that $\zeta_{NC} > 0$ at mid-radius, hence the N-C convection still acts to screen the W from the core.

Comparison of the pedestal parameters in Fig. 7 (e,f), show that whereas $T_{e,ped}$ is similar in the three pulses, while $n_{e,ped}$ is slightly lower in the pulse #96713 with the pellets, there is a significant difference in the ion parameters ($T_{i,ped}$ and $\Omega_{\phi,ped}$) from the edge CXRS measurements. In pulse #96713, there is a greater ratio of $T_{i,ped}/T_{e,ped} \sim 1.6$, than in the other two pulses (~ 1.4) and the rotation at the pedestal top $\Omega_{\phi,ped}$ is also $\sim \times 1.4$ higher.

In §2.1 above, we showed that this enhanced rotation in the pulse #97913 with pellets and the lower rate of gas fuelling, in fact occurs right across the plasma from the pedestal to the core. This perhaps arises from reduced CX damping of the toroidal momentum due to the lower D^0 atomic density resulting from the reduced gas puffing into the main chamber.

In the following section §2.7, the dependence of the W flushing efficiency $\Delta\bar{n}_W/\bar{n}_W$ on the fractional ELM density losses $\Delta\bar{n}_e/\bar{n}_e$ is investigated, classifying the data according to whether the ELMs are spontaneous or pellet-triggered events.

2.7. Influence of ELM type on W flushing efficiency

By identifying whether the ELMs are either spontaneous *aka* 'natural' or 'pellet-triggered' events, the data for the relative W flushing efficiency $\Delta\bar{n}_W/\bar{n}_W$ and inter-ELM fluence $(\Delta\bar{n}_W/\bar{n}_W)_{i-ELM}$ can be classified according to ELM type. This classification is performed by determining whether the occurrence of the ELMs is coincident with the arrival of the pellets at the plasma edge, as described in §Appendix A.

Such data is shown in Fig. 8 for six 3.5 MA baseline-scenario pulses with 30-37 MW of additional heating power, three with only D_2 gas fuelling at rates of $\Gamma_{D2,gas} \sim 1.5$, 2.3 & 3.0×10^{22} e/s and three with both gas fuelling ($1 - 1.5 \times 10^{22}$ e/s) and $\varnothing 2$ mm ELM pacing pellets ($f_{Pel} \sim 35$ Hz). The W flushing $\Delta\bar{n}_W/\bar{n}_W$ and inter-ELM fluence $\Delta\bar{n}_W/\bar{n}_W$ data are plotted as a function of the relative ELM density losses $\Delta\bar{n}_e/\bar{n}_e$, which are determined from the decrease at the ELMs of the line-average density $\bar{n}_e$ from channel #5 of the FIR interferometer passing diagonally through the lower, outer half of the plasma cross-section.

To better quantify the differences in these parameters between the different classes of ELMs, histograms, i.e. probability density functions (PDFs), of the distributions of the data are plotted on the corresponding axis. These histogram plots also show the mean and standard deviation of the data for each class of ELMs. While the 'natural' ELMs typically result in density losses $\Delta\bar{n}_e/\bar{n}_e \sim 5 - 10\%$, the density losses due to pellet-triggered ELMs are smaller and some of the pellets result in a small net fuelling.

Note that these ELM-pacing pellets are smaller (20%) than those used for fuelling, i.e. of $\varnothing 2$ mm c.f. $\varnothing 4$ mm for the fuelling pellets, and are hence mostly ablated before reaching the pedestal top. Typical particle contents of the pacing and fuelling pellets are $\sim 4 \times 10^{20}$ e$^-$ and $\sim 2 \times 10^{21}$ e$^-$ respectively.

Average values and standard deviations of the data show in Fig. 8 are stated in Table 4. For the natural ELMs, the average density losses $\langle\Delta\bar{n}_e/\bar{n}_e\rangle \sim -2.6 \pm 0.2\%$ are similar in both the gas-only and gas+pellet-fuelled pulses. However, for the pellet-triggered ELMs, on-average the density losses are considerably smaller $\langle\Delta\bar{n}_e/\bar{n}_e\rangle \sim -0.7 \pm 0.1\%$, i.e. there is significant net fuelling of the confined plasma by many of the pacing pellets.

There is a large scatter in the ELM flushing $(\Delta\bar{n}_W/\bar{n}_W)_{ELM}$ and inter-ELM fluence $(\Delta\bar{n}_W/\bar{n}_W)_{i-ELM}$ data for several reasons. Firstly, the measurement method gives only an approximate measure and is prone to error. Also, while some ELMs are followed by ELM-free
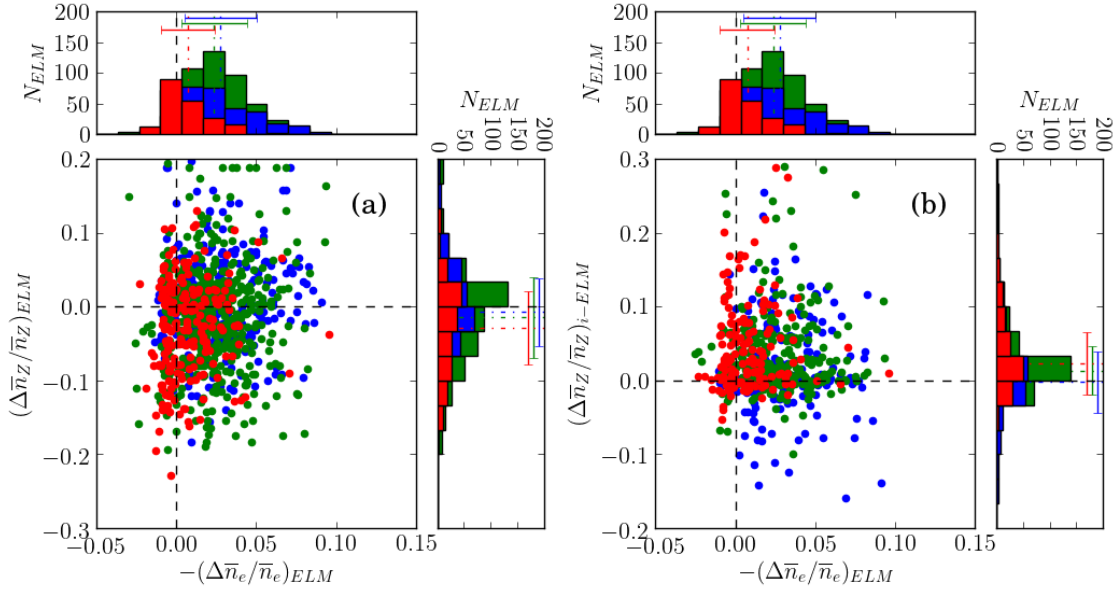
Figure 8: *Comparison of data from six* $3.5\,\mathrm{MA}/3.3\,\mathrm{T}$ *baseline-scenario pulses with* $30 - 37\,\mathrm{MW}$ *of additional heating power with: only gas fuelling (#94915 ($\Gamma_{D2} \sim 1.5 \times 10^{22}\,\mathrm{e/s}$), 94964 ($3.0 \times 10^{22}\,\mathrm{e/s}$) & 94980 ($2.3 \times 10^{22}\,\mathrm{e/s}$) •) and with both gas fuelling ($1 - 1.5 \times 10^{22}\,\mathrm{e/s}$) and pacing pellets ($f_{Pel} \sim 35\,\mathrm{Hz}$) and (#96536, 96713 & 96750 – •, •, for pellet triggered (•) and natural (•) ELMs, showing: (a) the relative change in W content of the confined plasma due to ELMs $(\Delta\bar{n}_W/\bar{n}_W)_{ELM}$ and (b) the inter-ELM fluences $(\Delta\bar{n}_W/\bar{n}_W)_{i-ELM}$. Histograms on the x- and y-axes show PDFs of the respective quantities for the different ELM types: in gas-only pulses (•) and pulses with pacing pellets for natural (•) and pellet-triggered (•) ELMs), where the dashed lines and error bars represent the average values and standard deviations of the data points.*

periods of significant duration, others are followed by the groups of rapid small ELMs, which complicates the measurement. In spite of these difficulties with the measurement, it may well be that some ELMs do result in a net *increase* in the W content as a result of an interchange component of the ELM instability [47], which could mix some cold plasma from the SOL containing W back into the confined plasma.

There are significant differences in the average ELM W flushing efficiency for the three ELM types. The ELMs in the gas fuelled pulses are on-average, about half as efficient at flushing the W than the natural ELMs in the pellet fuelled pulses, while the pellet triggered

Fuelling	ELM type	$\langle\Delta\bar{n}_e/\bar{n}_e\rangle$ [%]	$\langle\Delta\bar{n}_W/\bar{n}_W\rangle$ [%]	
-	-	ELM	ELM	inter-ELM
Gas-only	Natural	-2.8 ± 0.1	-0.7 ± 0.3	0.2 ± 0.3
Pel & Gas		-2.4 ± 0.2	-1.4 ± 0.2	1.3 ± 0.2
	Pellet	-0.7 ± 0.1	-2.9 ± 0.4	2.3 ± 0.3
-	All	-2.2 ± 0.1	-1.4 ± 0.2	0.9 ± 0.2

Table 4: *Average values of data shown in Fig. 8 by fuelling source and ELM type for high-power,* $3.5\,\mathrm{MA}/3.3\,\mathrm{T}$ *ITER-baseline pulses.*

ELMs are more efficient at flushing the W than the natural ELMs with either fuelling method. This is not simply a result of change to the the density losses $\Delta \bar{n}_e / \bar{n}_e$, which show the opposite trend with ELM type. Although the pellets result in lower net density losses following the triggered ELM, more W is flushed from the plasma than after natural ELMs.

There are also significant differences in the inter-ELM W fluence data between the natural and pellet triggered ELMs. On average, considerably more W is able to enter the plasma following the pellet triggered ELMs. Also, more W enters the plasma after the either ELM type in pellet+gas fuelled pulses than gas-only fuelled pulses. Note that the average magnitudes of the ELM W flushing and inter-ELM ingress are similar, so the net change in the W content of the plasma is a delicate balance between these processes. In §2.9 below, we investigate how differences between the pedestal and mantle gradient parameters might affect the transport of W in the edge plasma.

2.8. Influence of ELM type on sputtered impurity sources

Other than affecting the ELM W flushing efficiency and inter-ELM ingress of W into the plasma, the pellets might also affect the sources of impurities sputtered by the ELMs from the plasma facing components. In this section, we compare relative intra-ELM fluences, i.e. influxes integrated over the duration of the ELM peak in the line intensity signal, of Be and W impurities $\Phi_{Be,W}$ sputtered from the inner and outer divertor targets by the interaction with the ELMs.

A relative measure of these fluences can be estimated from time-integrated Be II (527 nm) and W I (401 nm) line intensities measured by a multi-chord spectrometer viewing the HFS, and LFS divertor targets. The lines of sight of this spectrometer are shown in Fig. E1 (a) of §Appendix E. Profiles of the Be II (527 nm) and W I (401 nm) line intensities time-integrated over the ELM peak are shown in Fig. E1 (b) as a function of the distance S along the divertor target. The most intense interaction with the ELM is with the top of the inner and outer vertical targets *aka* 'domes' and also at the strike points [45]. Also shown in Fig. E1 (c,d) are the evolution of the Be II (527 nm) and W I (401 nm) line intensities, summed over channels viewing the inner and outer divertor targets, over the duration of a typical type-I ELM, indicating the period over which the intra-ELM fluences are integrated.

Note that the inner strike point is hidden from view in this corner-corner (C-C) configuration in which the both strike points are close to the divertor pumping throats, so these measurements are unable to detect the impurity influxes from the vicinity of outer strike point. It has been shown from the analysis of spectrally filtered, fast-camera imaging data from JET-ILW that the intra-ELM sputtered W^0 influx is almost an order of magnitude larger than the time-integrated inter-ELM influx from the strike-point regions [49].

In Fig. 9 (a, b), relative, intra-ELM Be^+ fluences Φ_{Be}^{ELM} estimated (assuming constant ionisations/photon, S/XB) from the time-integrated Be II (527 nm line intensity data summed over the HFS and LFS divertor targets respectively, plotted versus the relative ELM density losses $\Delta \bar{n}_e / \bar{n}_e$. Similar data for the relative W^0 atomic, intra-ELM fluences Φ_W^{ELM} are shown in Fig. 10. Average values of these fluences $\langle \Phi_{Be} \rangle$ and $\langle \Phi_W \rangle$ with their standard deviations are stated in Table 5. The bremsstrahlung contribution to the W I line, detected by a LOS viewing through the x-point, which does not view a region of the target with significant interaction with the SOL plasma, is estimated to be $\lesssim 10\%$ during the intra-ELM periods.

The high degree of scatter in the relative ELM-sputtered Φ_{Be}^{ELM} and W^0 fluence data is shown in Fig. 9 and Fig. 10 is due to the similarly large spread in the ELM amplitudes. The averaged values over the whole data set, classified by fuelling source and ELM type, reveal
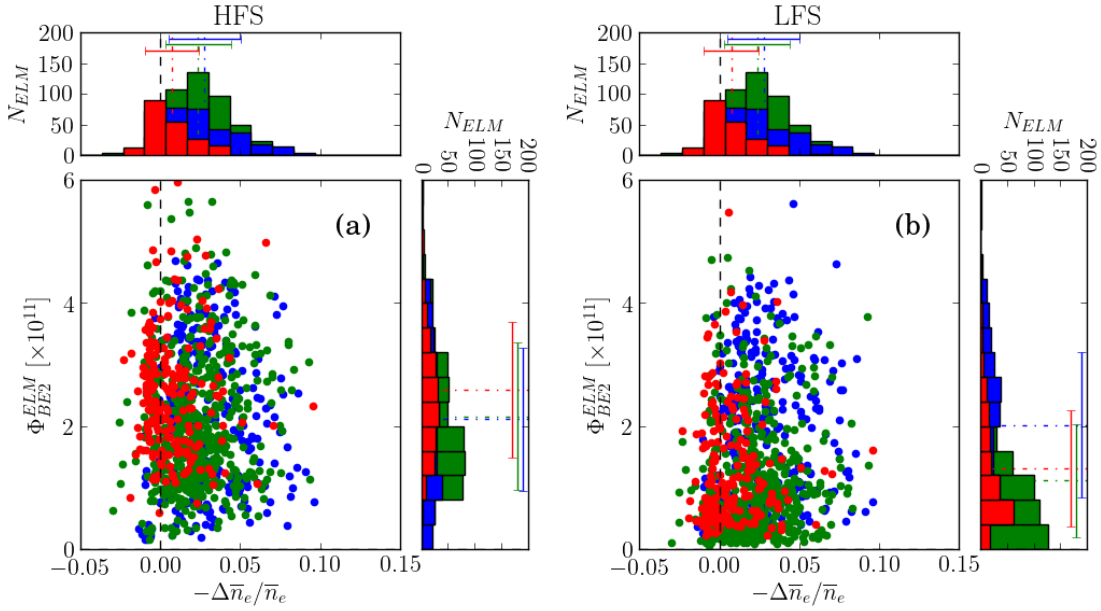
Figure 9: *Comparison of data from the same high-power, $3.5\,\mathrm{MA}/3.3\,\mathrm{T}$ pulses as for Fig. 8 with only gas (●) and with pellet and gas fuelling (●, ●), for pellet-triggered (●) and natural (●, ●) ELMs, showing: relative, time-integrated, intra-ELM fluences of Be^+ ions Φ_{Be}^{ELM} measured by a multi-channel visible-range spectrometer (KS3) viewing the divertor region, spatially integrated over: (a) the HFS and (b) the LFS divertor targets. As in Fig. 8, the histograms show PDFs of the respective quantities for the different ELM types.*

little significant difference between these fluences at the HFS target between these cases, except that the natural ELMs sputter slightly less W impurities ($\sim \times 0.8$) and the pellet-triggered ELMs slightly more Be ($\sim \times 1.15$) than the average over all ELMs. This is reversed at the LFS target, where the natural ELMs in the gas-only fuelled pulses do sputter significantly more W and Be ($\sim \times 1.2$ & 1.4 respectively) than the average over all ELMs.

Note that the ADAS spectroscopic data in Fig. E2, shows that the values of ionisations/photon (S/XB) for these Be and W lines increases with both T_e and n_e, as does the fraction of W^+ ions promptly redeposited at the surface [3]. However, without T_e and n_e data with sufficient temporal ($\mathcal{O}(100\,\mu\mathrm{s})$) and spatial resolution $\mathcal{O}(1\,\mathrm{cm})$ measured at the divertor target surface, it is impossible to evaluate absolute influxes from the measured intensities.

Fuelling	ELM type	HFS		LFS		Total	
-	-	$\langle\Phi_W\rangle$	$\langle\Phi_{Be}\rangle$	$\langle\Phi_W\rangle$	$\langle\Phi_{Be}\rangle$	$\langle\Phi_W\rangle$	$\langle\Phi_{Be}\rangle$
-	-	[a.u.]	[a.u.]	[a.u.]	[a.u.]	[a.u.]	[a.u.]
Gas-only	Natural	1.15 ± 0.03	2.11 ± 0.07	0.73 ± 0.02	2.02 ± 0.07	1.88 ± 0.05	4.13 ± 0.12
Pel & Gas		1.48 ± 0.03	2.16 ± 0.05	0.52 ± 0.02	1.11 ± 0.04	2.00 ± 0.04	3.27 ± 0.10
	Pellet	1.46 ± 0.03	2.59 ± 0.08	0.60 ± 0.03	1.32 ± 0.07	2.06 ± 0.05	3.91 ± 0.13
-	All	1.38 ± 0.02	2.23 ± 0.04	0.60 ± 0.01	1.42 ± 0.03	1.97 ± 0.03	3.65 ± 0.07

Table 5: *Average values of the relative intra-ELM Be^+ and W^0 fluence data $\langle\Phi_{Be}\rangle$ and $\langle\Phi_W\rangle$, classified by fuelling source and ELM type for the data shown in Fig. 9 and Fig. 10 from high-power, $3.5\,\mathrm{MA}$ pulses. The sum of these fluences from both HFS and LFS targets is also stated.*
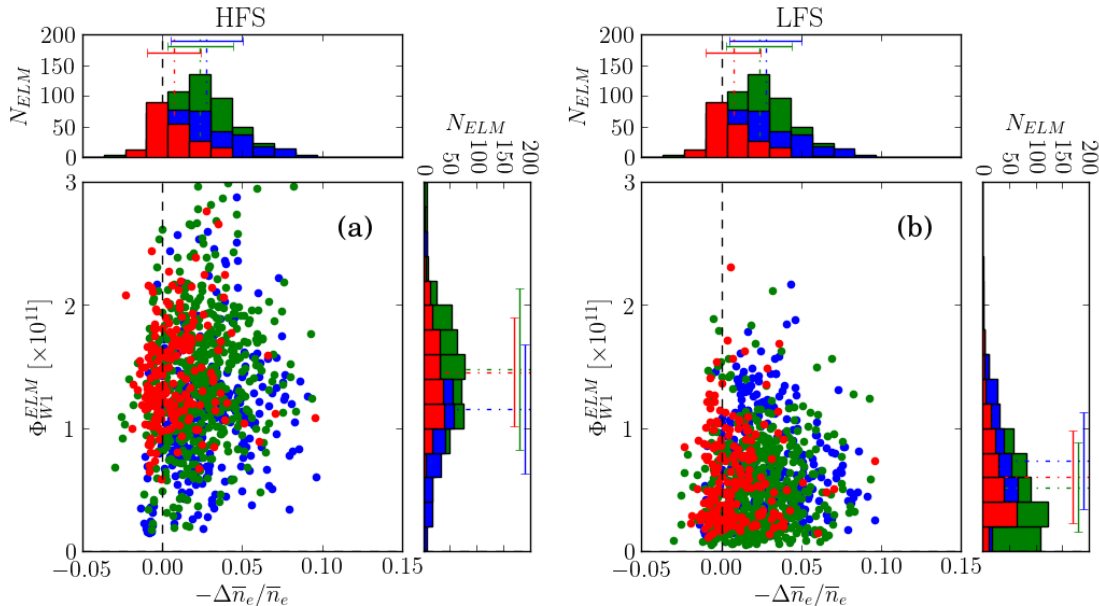
Figure 10: *Comparison of data from the same high-power,* $3.5\,\mathrm{MA}/3.3\,\mathrm{T}$ *pulses as for Fig. 8 with only gas (●) and with pellet and gas fuelling (●, ●), for pellet-triggered (●) and natural (●, ●) ELMs, showing: relative, time-integrated, intra-ELM fluences of* W^0 *atoms* Φ_W^{ELM} *measured by a multi-channel visible-range spectrometer (KS3) viewing the divertor region, spatially integrated over: (a) the inner (HFS) and (b) the outer (LFS) divertor targets. As in Fig. 8, the histograms show PDFs of the respective quantities for the different ELM types.*

By assuming fixed values of S/XB and assuming that the measured Be^+ influx is equal to the incident flux at the targets, i.e. assuming a balance between erosion and redepositon, it is possible to calculate an effective sputtering yield for W by Be^+ ions $\gamma_{Be^{4+}\rightarrow W}$ from the data presented in Fig. 10 and Fig. 9. Results from such a simplified calculation are presented in Fig. E3 of §Appendix E, which result values for the yield $\gamma_{Be^{4+}\rightarrow W} \sim 0.5-1.0$, which are consistent with values shown in Fig. 9 of Ref. [50], which were obtained using the same diagnostic, assumed S/XB values and spectrometer on JET-ILW.

In Ref. [50], it was shown that such high values for $\gamma_{Be^{4+}\rightarrow W} \sim 0.5-1.0$ are higher than that possible for Be^+ ions on W from physical sputtering, which has a maximum yield of $\gamma_{Be^{4+}\rightarrow W} \sim 0.4$. It was therefore concluded that there must be a significant contribution from W sputtering by the incident D^+ fuel ions during type-I ELMs at the prevailing pedestal temperatures in JET-ILW. Note that the data shown in Fig. E3 shows no significant difference in the measured sputtering yield $\gamma_{Be^{4+}\rightarrow W}$ for the different classes of ELMs.

2.9. Effect of pellets on pedestal & mantle parameters

We have seen above in §2.3 that the amount of W in the plasma is a result of a delicate balance between the influx across the pedestal driven by inward neo-classical convection and the flushing of the W by the ELMs. Also, the in the high-power ITER-baseline pulses investigated here, the W is typically localised by outward neo-classical convection to the outer, mantle region, hence mitigating the tendency for this to accumulate in the plasma core.

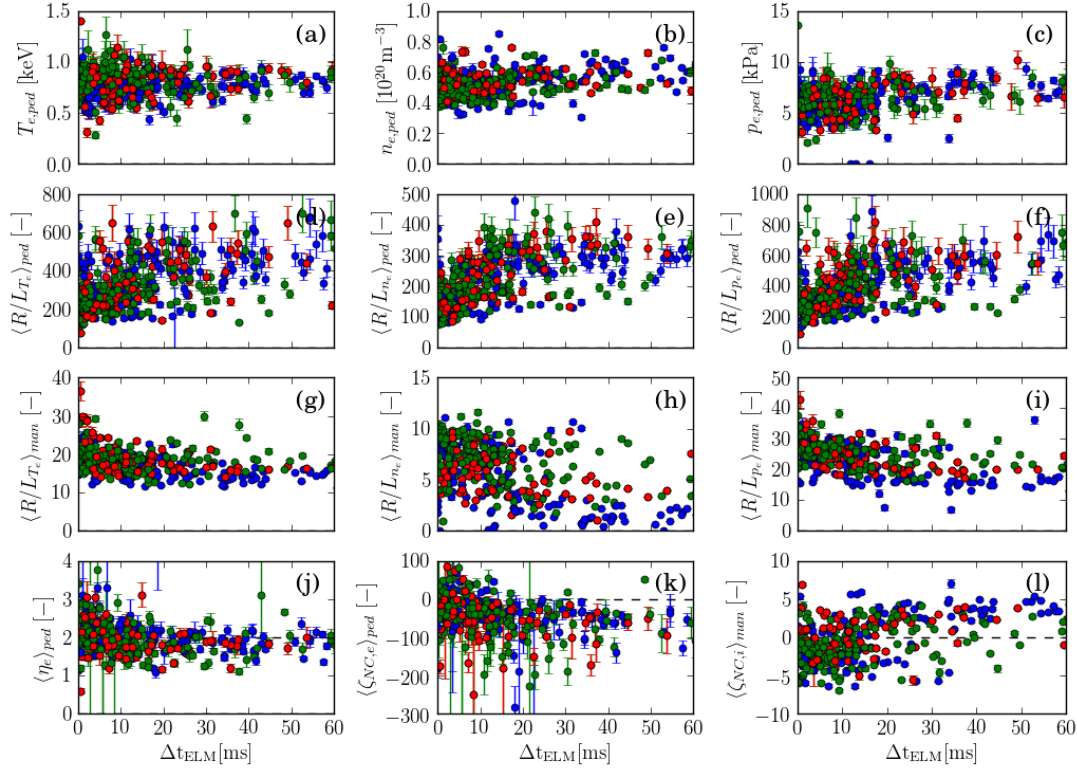In this section, we quantify the effect of the ELM pacing pellets on the density and

Figure 11: *Inter-ELM evolution of parameters determined from fits to HRTS n_e and T_e profile data as a function of the time from the previous ELM Δt_{ELM} for the same six $3.5\,\text{MA}/3.3\,\text{T}$ ITER-baseline pulses as analysed in §2.7, showing: the pedestal top parameters $T_{e,ped}$, $n_{e,ped}$ and $p_{e,ped}$ (a-c); their normalised gradients R/L_{T_e}, R/L_{n_e} and R/L_{p_e} averaged over the pedestal $\langle...\rangle_{ped}$ (d-f) and mantle regions $\langle...\rangle_{man}$ (g-i); and the parameter $\langle\eta_e\rangle_{ped}$ averaged over the pedestal region (j) and the neo-classical convection parameter averaged over the pedestal $\langle\zeta_{NC}\rangle_{ped}$ (k) and mantle regions $\langle\zeta_{NC}\rangle_{man}$ (l). The colors indicate the previous ELM type: natural ELMs in the gas fuelled pulses (•); natural ELMs (•) or pellet triggered ELMs (•) in pulses with pellet+gas fuelling.*

temperature gradients in the pedestal and mantle regions during the inter-ELM periods following the pellet triggered ELMs, comparing the derived quantities ζ_{NC} and $\eta_e = L_{n_e}/L_{T_e}$ (which govern the neo-classical impurity convection and provide the drive for electron-temperature-gradient (ETG) driven turbulence, respectively) during inter-ELM periods following the pellet-triggered or natural, spontaneous ELMs.

Pedestal characteristics $T_{e,ped}$, $n_{e,ped}$ and $p_{e,ped}$ and gradient parameters derived from $mtanh()$ fits to n_e and T_e profile data from the high-resolution, Thomson scattering system (HRTS) [38] are shown in Fig. 11. Values of the gradient parameters R/L_{T_e}, R/L_{n_e} and R/L_{p_e} and the derived parameters ζ_{NC} and η_e are spatially averaged over the pedestal $\langle...\rangle_{ped}$ and mantle $\langle...\rangle_{man}$ regions. In this figure the color represents the type of the ELM preceding the HRTS measurement, i.e. whether the ELMs are pellet-triggered or natural ELMs in either gas-only or pellet+gas fuelled pulses.

In order to determine whether the ELM-pacing pellets have any statistically significant effect on the average values of the parameters ζ_{NC} and η_e over the pedestal and mantle regions,
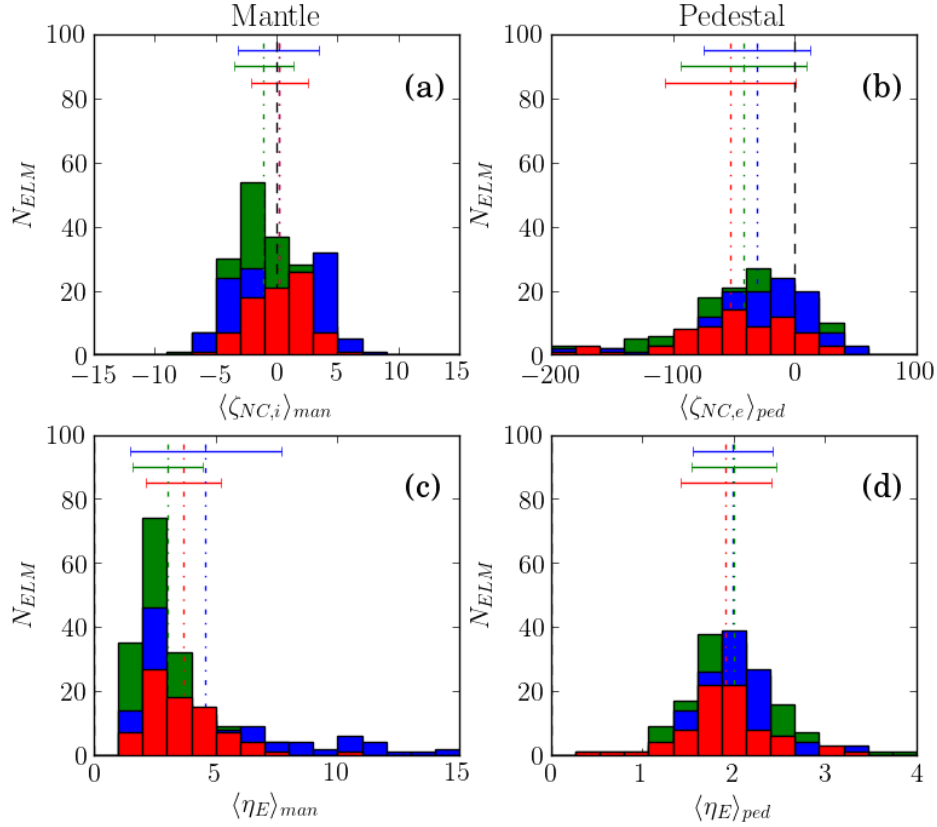
Figure 12: *PDFs of the gradient parameters: (a, b - top) ζ_{NC} and (c, d - bottom) η_e shown in Fig. 11 for 3.5 MA ITER-baseline pulses, spatially-averaged over the mantle (a, c - left) and density pedestal (b, d - right) regions, where the data points have been selected by the ELM type preceding the HRTS measurement times: natural ELMs in the gas fuelled pulses (•) and natural ELMs (•) or pellet triggered ELMs (•) in pulses with pellet+gas fuelling.*

the data shown in Fig. 11 is plotted in Fig. 12 in the form of histograms, where the data is distinguished according to the preceding ELM type. Average values and standard deviations of the data (σ_{data}), also shown in Fig. 12, are stated in Table 6.

Referring to the values of $\langle \zeta_{NC} \rangle_{ped}$ in Table 6, we see that on-average there is relatively strong inward impurity convection ($\langle \zeta_{NC} \rangle_{ped} \sim -(30-50)$) across the pedestal during the inter-ELM periods. However, the time-resolved data shown in Fig. 11 shows that, during the first ~ 10 ms after the pellet-triggered and natural ELMs in the pellet fuelled pulses (•, •) there is some tendency for this convection to weaken (and sometimes even reverse) due to the relatively higher $\langle R/L_{n_e} \rangle_{ped}$ following these ELMs. There is hence some tendency for the pacing pellets to reduce the inward W influx just after the ELMs.

In the mantle region, the overall average value of $\langle \zeta_{NC} \rangle_{man} \sim 0.14$ following all of the ELMs is much weaker than that prevailing in the pedestal region ($\langle \zeta_{NC} \rangle_{ped} \sim -(30-50)$). On-average, there is a somewhat higher, positive value of $\langle \zeta_{NC} \rangle_{man} \sim 0.24$ following the pellet triggered ELMs due to the fuelling at the pedestal top by the pellets reducing $\langle R/L_{n_e} \rangle_{man}$. However, after the natural ELMs in the pellet fuelled pulses, there is a slightly negative average value of $\langle \zeta_{NC} \rangle_{man} \sim -1.1$, driving inward impurity convection. This probably arises because of relatively low level of gas fuelling in the pellet fuelled pulses results in a slightly lower $n_{e,ped}$

than in the gas fuelled pulses and hence a higher value of $\langle R/L_{n_e}\rangle_{man}$, which favours inward impurity convection. Hence, while the ELM pacing pellets do modify the pedestal gradients on-average such as to slightly reduce the convection of W (and other impurities) across the pedestal, they also modify the mantle gradients to reduce the screening of these impurities from the plasma core.

Somewhat as an aside to the topic of this paper, the average values of η_e in the pedestal and mantle regions are worthy of note. As was discussed in [8] with respect to the high-power, 3 MA ITER-baseline pulse #92432, the value of η_e averaged over the steep density gradient region ($\rho_{N,ped} \leq \rho_{tor} \leq 1.0$) of $\langle \eta_e \rangle_{ped} \sim 2$ is similar to that also found in pulse #92432, which may indicate that there may be a degree of stiffness of the electron heat transport in the pedestal, predominantly due to the slab branch of ETG turbulence, which is destabilised at a critical $\eta_e \sim \mathcal{O}(1)$. Note that, on-average, there is also an increase in $\langle \eta_e \rangle_{ped}$ during the first $\sim 10\,\mathrm{ms}$ following the ELMs, providing a stronger drive for turbulent electron heat transport at this time.

However, in the mantle ($0.7 \leq \rho_{tor} \leq \rho_{N,ped}$), the average value of $\langle \eta_e \rangle_{man} \sim 3-5$ is larger than in the pedestal region, which may be consistent with the higher values of η_e required to destabilise the toroidal branch of ETG turbulence at the relatively low values of $\langle R/L_{n_e}\rangle_{man} \sim 5-10$ prevailing in the mantle compared to those in the pedestal region ($\langle R/L_{n_e}\rangle_{ped} \sim \mathcal{O}(-100)$). For further discussion of this topic see §4 of Ref. [8].

3. Summary & Discussion

3.1. Summary of results

Before discussing the mechanism underlying the effect of the strong W radiation on the evolution of these high-power, ITER-baseline pulses in JET-ILW, in §3.2, we summarise the main results from the previous sections:

§2: *Comparison of high-power, 3.5 MA pulses with different fuelling sources*

Comparing the performance of three, high-power 3.5 MA ITER-baseline pulses with different fuelling scenarios, it is evident that, although the energy confinement is higher with a lower rate of D_2 gas fuelling, such pulses are non-stationary, exhibiting long periods of ELM-free H*-mode which follow a large, type-I ELM and subsequent periods of rapid, type-III ELMs. During the long H*-phases, the increasing $n_{e,ped}$ causes a strong increase in $\mathcal{F}_{Rad}$, which can exceed the threshold to initiate an early pulse termination or sometimes cause an immediate disruption.

Increasing the gas fuelling rate from $\Gamma_{D2} \sim 1.5$ to $2.3 \times 10^{22}\,\mathrm{e/s}$ induces more frequent, compound ELMs interspersed by shorter H*-phases. Consequently, the increased rate of

Fuelling	ELM type	ζ_{NC}		η_e	
-	-	Pedestal	Mantle	Pedestal	Mantle
Gas-only	Natural	-30 ± 4	0.16 ± 0.2	2.0 ± 0.4	4.5 ± 0.3
Pel & Gas		-42 ± 4	-1.1 ± 0.2	2.0 ± 0.4	3.1 ± 0.1
	Pellet	-52 ± 6	0.24 ± 0.3	1.9 ± 0.6	3.7 ± 0.2
-	All	-40 ± 2	0.14 ± 0.2	2.0 ± 0.3	3.7 ± 0.2

Table 6: *Average values of data shown in Fig. 12 by fuelling source and ELM type for high-power, 3.5 MA ITER-baseline pulses.*

flushing of W impurities, which dominate the radiation losses, maintains $\mathcal{F}_{Rad} \lesssim 30\%$, thereby prolonging the duration of the ELMy H-mode phase. The effect of the higher gas-puffing rate is, however, to reduce the normalised confinement from $H_{98,y2} \sim 1.0$ to ~ 0.8.

Whether these pulses are fuelled only by gas or by gas and the ELM pacing pellets has little effect on $\bar{n}_e$, which corresponds to a normalised Greenwald fraction $f_{GW} \lesssim 0.7$ in the pulses investigated. The most pronounced effect of increasing the gas fuelling rate is to reduce the axial $T_{i,0}$ from $\sim 8\,\text{keV}$ to $\sim 6\,\text{keV}$, which causes a much larger reduction of the D-D neutron rate by $\sim 50\%$. Whether this increase in confinement is due to an improvement in the pedestal or core confinement of the ions and/or electrons was investigated in §2.1.

The injection of the ELM-pacing pellets allows the duration of such high-power ITER-baseline pulses to be extended, while maintaining the high confinement associated with a low gas fuelling rate. Comparing a pulse with pacing pellets injected at $f_{Pel} \sim 45\,\text{Hz}$, with the same total fuelling rate but with $\sim 40\%$ of the D_2 gas-puffing rate as the high-gas rate pulse, albeit with $\sim \times 1.15$ the input power, the normalised confinement is restored to $H_{98,y2} \sim 1.0$. By triggering ELMs, in spite of the increased $\mathcal{F}_{Rad}$ compared to that with the higher gas fuelling rate, long ELM-free H*-phases are avoided and the duration of the ELMy H-mode phase extended.

Although most but not all of the pellets trigger ELMs, the ELM frequency is not locked to that of the pellets but is typically higher, i.e. $f_{ELM} > f_{Pel}$, and the ELMs also remain of a mixed, compound nature. The considerably higher $\sim \times 1.5$ D-D neutron rate achieved in the pellet+gas fuelled pulse is attributable to the higher $\sim \times 1.6$ axial ion temperature. The cause of the improvement in core ion confinement is also investigated in the following section.

§2.1: *Comparison of energy confinement in pulses #94980 and #96713*

A comparison of results of interpretive, power-balance analysis of the pulses #94980 with a high gas-fuelling rate and pulse #96713 with the same fuelling rate from pellets+gas, shows that the much higher $T_{i,0}$ and axial rotation rate Ω_ϕ is not due to an increase in the pedestal confinement, with similar $\langle T_{e,ped} \rangle$, $\langle T_{i,ped} \rangle$ and $\langle \Omega_{\phi,ped} \rangle$ in the two pulses. What does change on reducing the gas-fuelling rate, is a reduced $n_{e,ped}$, which at the same $\bar{n}_e$ corresponds to a more peaked density profile, i.e. $\bar{n}_e/n_{e,ped} \sim 1.5$ c.f. ~ 1.35 at the higher gas puffing rate. The $\sim \times 1.3$ increase in W_{pl} in the pellet+gas fuelled pulse is primarily due to an increased ratio of energy stored in the ions to that in the electrons, i.e. $\langle W_i \rangle / \langle W_e \rangle \sim 1.3$ c.f. ~ 1.05 in the gas-fuelled pulse.

§2.2 *Comparison of core heat and momentum transport in pulses #94980 and #96713*

Comparison of the transport of heat and toroidal momentum in pulses #94980 and #96713 reveals significant differences. In the gas+pellet fuelled pulse #96713 the ion and electron heat fluxes across the core plasma are almost equal, with $q_e/q_i \sim 1$ right across the plasma. In contrast, in the gas fuelled pulse #94980 inside mid-radius, the ion heat transport is more virulent than the electron heat transport. In both pulses, the ion thermal diffusivity is well above the ion neo-classical level, with $\chi_i/\chi_{i,NC} \gtrsim \mathcal{O}(10)$. It is likely that the higher $E \times B$ flow shear ($\sim \times 3$) in the pulse #96713 at mid-radius results in stronger suppression of the level of turbulent ion heat transport compared to that in pulse #94980. This is a consequence of the more central deposition of ion heating and torque due to the increased density peaking in the pellet+gas fuelled pulse.

§2.3 *W impurity behaviour in* $3.5\,\text{MA}$ *baseline pulses*

It has been shown in a previous paper [8] that the radiation losses in such high-power, ITER-baseline pulses in JET-ILW is dominated by that from W impurities, which can account for $\gtrsim 95\%$ of the radiated power. During the ELMy H-mode phase of such plasmas, these impurities are typically concentrated in the peripheral mantle region of the plasma, from where

$\sim 70\%$ of the total radiation is emitted. Centrifugal forces due to the toroidal rotation [36] concentrate the W impurities forming an intense, radiating 'blob' at the outer mid-plane.

Neo-classical, radial convection of the impurities is controlled by the gradients of n_i and T_i, with a peaked n_i profile favouring core accumulation unless there is adequate screening due to a sufficiently peaked T_i profile. If the parameter $\zeta_{NC} = R/2L_{T_i} - R/L_{n_i} < 0$, the impurities will tend to accumulate in the plasma core.† In these ITER-baseline plasmas, the relatively high pedestal density, which is a consequence of operating at higher high-current and lower-q than e.g. in hybrid-scenario plasmas [1], results in a weakly peaked, rather flat n_e profile. Consequently, the much weaker normalised n_e gradient R/L_{n_e} in comparison to that of the ion temperature R/L_{T_i} favours outward convection $\zeta_{NC} > 0$ right across the plasma core, which concentrates the W impurities in the mantle region, just inside the pedestal top.

Note that, in the pedestal region, the steeper n_e gradient relative to that of T_i results in strong inward impurity convection $|\zeta_{NC}| > \mathcal{O}(10 - 100)$, which sweeps the impurities into the confined plasma, across the pedestal towards the pedestal top. Even operating baseline-scenario pulses at 3 or 3.5 MA with increased heating power up to ~ 37 MW does not increase $T_{i,ped}$ sufficiently to reverse the inward impurity convection across the pedestal.

Any weakening of the n_e gradient in the mantle region relative to that of T_i will also weaken the screening of the W and other impurities from the plasma core. This is the case in the pellet+gas fuelled pulse #96713, in which the frequent small ELMs somewhat reduce the degree of n_e peaking. Hence, the W is not so well screened from the core in this pulse than in the comparison gas-fuelled pulse #94980.

Also, an H/L-mode transition causes a collapse of $n_{e,ped}$, increasing R/L_{n_e} in the peripheral mantle region, causing rapid accumulation of the W impurities, as is illustrated in §2.5 with reference to such an event in pulse #92432.

§2.4: *Evaluation of ELM W 'flushing' efficiency*

While the W (and other high-Z) impurities are localised to the mantle region, they can be efficiently flushed from the core plasma by the ELMs. Because radiation from W dominates the total radiated power and the emissivity coefficient $\mathcal{R}_\epsilon$ of W is approximately constant across the mantle region, a measure of the relative ELM flushing efficiency $(\Delta \bar{n}_W / \bar{n}_W)_{ELM}$ and the inter-ELM influx $(\Delta \bar{n}_W / \bar{n}_W)_{i-ELM}$ can be obtained from bolometric measurements of the radiated power, as can the average concentration of W in the mantle region $\langle C_W \rangle_{man}$.

§2.5: *ELM W flushing and 'radiation event' in pulse #92432*

Results from the high-power 3 MA baseline-scenario pulse #92432, show that the regular, type-I ELMs flush $\sim 5 - 10\%$ of the W impurities per ELM, while a similar amount enters the confined plasma between ELMs, which maintains $\langle C_W \rangle_{man} \sim 2\%$ throughout the pulse. Core accumulation of W later in this pulse, following an H/L-transition, which is caused by excessive radiation during an ELM-free H*-phase, ends the high-performance phase of this pulse. This rather clear example of such an event illustrates how excessive W radiation can frequently lead to early termination or disruptions in high-power H-mode pulses in JET-ILW. A more detailed explanation of the phenomenology of such events is given in §3.2.

§2.6: *ELM flushing and W behaviour in 3.5 MA pulses*

Comparison of the behaviour of the W radiation in three 3.5 MA baseline pulses at similar input powers shows that:

---

† Following the treatment in Ref. [51], assuming the impurity transport is governed by effective diffusivity D_I and radial convective velocity $V_{c,I}$, integrating the steady-state particle balance equation outward from the axis gives the relative impurity density profile as $n_I(r)/n_I(0) = \exp\left\{\int_0^r (V_{c,I}/D_I)dr\right\}$. Hence, inward neo-classical convection results in a peaked impurity density profile and vice versa.

 – With insufficient D_2 gas fuelling, such pulses are non-stationary due to the effect of excessive W radiation from the mantle. By reducing the power crossing the separatrix P_{Sep}, this can either cause a change from large-amplitude type-I to rapid type-III ELMs, thereby reducing the R/L_{n_e} in the mantle, resulting in less screening of the W from the core, or induce long H*-phases, which lead to even stronger mantle radiation and subsequent early pulse termination or a disruption.

 – A higher, 'conservative' ($\sim \times 1.5$) rate of gas fuelling, recovers a stationary ELMy H-mode with more frequent, small-amplitude ELMs, which maintain a lower W concentration and hence lower $\mathcal{F}_{Rad}$. However, this is at the expense of core energy confinement, particularly in the ion channel, which results in weaker screening of the W from the core plasma due to reduced R/L_{T_i} at mid-radius. The reduced core T_i, is likely due to less $E \times B$ shear stabilisation of ion-scale turbulent transport. Reduced toroidal rotation Ω_ϕ, starting at the pedestal top is probably a result of decreased CX damping on a lower edge D^0 density.

 – Regular injection of ELM-pacing pellets $f_{Pel} \sim 45\,\text{Hz}$, allows steady ELMy H-mode operation at a much reduced ($\sim \times 40\%$) D_2 gas fuelling rate, while maintaining a higher normalised energy confinement $H_{98,y2} \sim 1$. Most of the pacing pellets trigger ELMs, hence preventing the occurrence of the H*-phases. A more detailed investigation of the effect of the pacing pellets and also the gas fuelling rate on the ELM characteristics are presented in §Appendix A. The improved energy confinement achieved with the pacing pellets seems to arise from a lower $n_{e,ped}$ and hence increased n_e peaking, which results in more central deposition of power and torque from the NBI heating, particularly to the ions.

§2.7: *Influence of ELM type on W flushing efficiency*

While the 'natural' ELMs typically result in density losses $\sim 5 - 10\%$, the density losses due to pellet-triggered ELMs are smaller and some pellets result in a small $\sim 1\%$ net fuelling of the pedestal. On-average the W flushing efficiencies of the ELMs is $(\Delta \bar{n}_W / \bar{n}_W)_{ELM} \sim 2 \pm 1\%$, with natural ELMs flushing less ($\sim 1 \pm 0.3\%$) W than pellet triggered ELMs ($\sim 3 \pm 0.5\%$). A similar amount of W is found to enter the plasma between ELMs, with significantly more influx following pellet-triggered ELMs.

§2.8 *Influence of ELM type on sputtered impurity sources*

The averaged values of spectroscopically measured, inter-ELM fluences (time-integrated influxes) of Be^+ and W^0 over several high-power 3.5 MA pulses, for ELMs classified by fuelling source and ELM type, reveal little significant difference between these fluences at the HFS target, except that the natural ELMs in the gas-only fuelled pulses sputter slightly less W ($\sim \times 0.8$) and the pellet-triggered ELMs slightly more Be ($\sim \times 1.15$) impurities. At the LFS target, the opposite is the case, where the natural ELMs in the gas-only fuelled pulses sputter significantly more W and Be ($\sim \times 1.2$ & 1.4 respectively) than the average over all ELMs.

Assuming the ELM-sputtered Be^+ fluence is the same as that of the incident Be^{4+} ions, values for the $Be^{4+} \to W$ sputtering yield of $\langle \gamma_{Be^{4+} \to W} \rangle \sim 0.5 \to 1.0$ are estimated from the influx measurements. No significant difference in the measured yields was found for the different classes of ELMs. Such values of $\langle \gamma_{Be^{4+} \to W} \rangle$ are higher than possible for physical sputtering, for which the maximum yield for the $Be^{4+} \to W$ is ~ 0.4 [50], which implies that there must be a significant contribution from physical sputtering of W by the incident D^+ fuel ions.

§2.9 *Effect of pellets on pedestal & mantle parameters*

Values of the neo-classical convection parameter ζ_{NC} and $\eta_e = L_{n_e}/L_{T_e}$ averaged over the pedestal and mantle regions have been evaluated from HRTS and CXRS T_e, n_e and T_i profile measurements during the inter-ELM periods. These parameters drive the neo-classical impurity convection and the electron-scale (ETG) turbulence respectively:

Neo-classical impurity convection:

- On-average, there is relatively strong inward impurity convection ($\langle\zeta_{NC}\rangle_{ped} \sim -(30-50)$) across the pedestal during the inter-ELM periods. However, in the pellet-fuelled pulses, during the first $\sim 10\,\mathrm{ms}$ after the ELMs $\langle\zeta_{NC}\rangle_{ped}$ weakens and sometimes reverses due to a relatively lower value of R/L_{n_e}. Hence, just after the ELMs, there is some tendency for the pacing pellets to reduce the inward W influx across the pedestal.

- In the mantle, the average value after all ELMs of $\langle\zeta_{NC}\rangle_{man} \sim 0.14$ is much weaker than in the pedestal region. Following the pellet-triggered ELMs, there is a higher, positive value of $\langle\zeta_{NC}\rangle_{man} \sim 0.24$ due to the fuelling at the pedestal top by the pellets reducing $\langle R/L_{n_e}\rangle_{man}$. However, during the subsequent periods with small, rapid ELMs, the average value of $\langle\zeta_{NC}\rangle_{man} \sim -1.1$ is negative, favouring inward impurity convection.

Hence, while the ELM pacing pellets do modify the average pedestal gradients such as to slightly reduce the convection of W (and other impurities) across the pedestal, they also modify the mantle gradients, reducing the screening of these impurities from the core.

ETG turbulent drive:

- The value of η_e averaged over the steep density gradient region of the pedestal is limited to a value of $\langle\eta_e\rangle_{ped} \sim 2$, which may indicate that there is some degree of stiffness of the electron heat transport, predominantly due to the slab branch of ETG turbulence, which is destabilised at a critical $\eta_e \gtrsim 1$.

- In the mantle, the average, prevailing value of $\langle\eta_e\rangle_{man} \sim 3-5$ is larger than in the pedestal region, which may be consistent with the higher values of η_e required to destabilise the toroidal branch of ETG turbulence.

Note that the above observations are consistent with similar results for the high-power, $3\,\mathrm{MA}$ pulse #92432, discussed in detail Ref. [8], where a simple, heuristic model for the pedestal temperature $T_{e,ped}$, based on stiff ETG turbulent heat transport, is discussed.

3.2. Proposed mechanism for the influence of W radiation the evolution of high-power, ITER-baseline pulses in JET-ILW

As mentioned in the introduction, sustained H-mode operation of JET-ILW pulses requires fuelling by gas puffing to mitigate the detrimental effect of W impurities sputtered from the divertor targets, predominantly but not exclusively by the extremely high instantaneous powers deposited by the ELMs. The beneficial effect of the gas puffing on this process is illustrated systematically in Fig. 13.

Although the physics underlying each step is not always well understood, the underlying mechanism can be explained as follows:

A) *Effect of increased gas fuelling on ELMs:*

More gas fuelling typically increases the ELM frequency f_{ELM} and reduces the ELM energy losses ΔW_{ELM} (at approximately constant $\langle P_{ELM}\rangle$), resulting in a lower sputtered
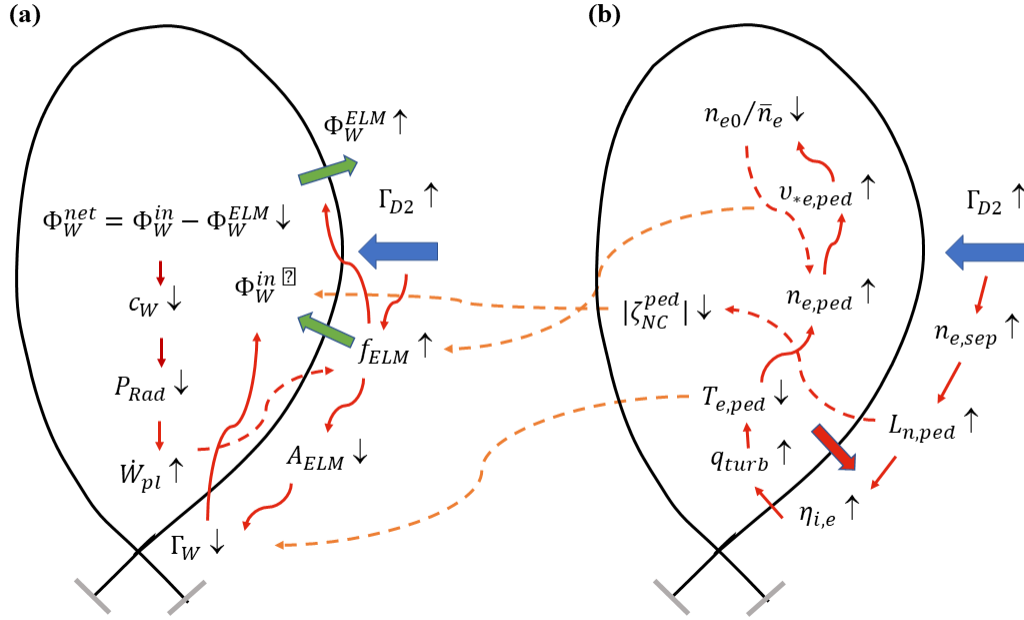
Figure 13: *Schematic representation of the effect of gas puffing on: (a) the ELM behaviour and W radiation and (b) the inter-ELM pedestal characteristics.*

W source S_W from the divertor targets. A lower W concentration c_W in the SOL then reduces the impurity influx to the confined plasma between ELMs Φ_W^{in} and the higher ELM frequency flushes more W out again Φ_W^{ELM}. A lower W concentration in the confined plasma then reduces the radiated power P_{Rad}^{Pl}, thereby increasing the rate of increase of stored energy dW_{pl}/dt between the ELMs. This causes $p_{e,sep}$ to reach the MHD pressure limit faster, triggering the ELMs earlier and thereby increasing their frequency f_{ELM}. The chain of causality of the effects of increased gas fuelling are illustrated in Fig. 13 (a).

B) *Effect of increased gas fuelling on pedestal and confinement:*

Although the effect of the gas fuelling on the inter-ELM pedestal structure is beneficial in terms of further mitigating the W contamination, it also reduces the energy confinement by degrading the pedestal temperature, which reduces the temperature over the whole plasma due to stiffness of core heat transport. An increase in turbulent heat flux across the pedestal due to changes in its structure caused by the gas puffing is now well established as the most plausible explanation for the low pedestal temperature in JET-ILW pulses [10, 12, 14, 52, 53] and this is illustrated schematically in Fig. 13 (b).

Increased gas puffing raises the separatrix density $n_{e,sep}$, which decreases the density gradient across the pedestal, increasing L_{n_e} and hence $\eta_{i,e}$ across the ETB, providing a stronger drive for turbulent heat transport. With the residual power through the ETB P_{Sep}^{iELM} determined by the heating power, radiation and ELM losses, an increase in the heat turbulent heat diffusivity χ_{eff} must reduce the pedestal temperature $T_{e,ped}$.

As a consequence of reducing $T_{e,ped}$, a higher pedestal density $n_{e,ped}$ is required for $p_{e,ped}$ to reach the peeling-ballooning limit at which ELMs are triggered. The lower $T_{e,ped}$ and

higher $n_{e,ped}$ increases the effective collisionality $\nu_{eff} \propto n_e/T_e^2$ at the pedestal top. This then reduces the density peaking $n_{e,0}/\bar{n}_e$, which is driven by a turbulent particle pinch, thereby reinforcing the higher $n_{e,ped}$ [54].

Conversely, less gas fuelling is required with the pellets, resulting in reduced $n_{e,ped}$ and higher $T_{e,ped}$ and lower ν_{eff}, which favours density peaking. This is then further reinforced by the more central beam ionisation source resulting from the reduced $n_{e,ped}$, which is known to play an important role in peaking the density profile in JET-ILW [55].

C) *Feedback loops between gas puffing, ELMs and W behaviour:*

As indicated in Fig. 13, there is coupling between the changes to the pedestal structure, the ELM behaviour and the W transport, which reinforce the effects of the gas puffing. Firstly, the higher L_{n_e} reduces the magnitude of the inward convection ζ_{NC} across the ETB, which reduces the W influx Φ_W^{in} into the confined plasma. Secondly, the lower $T_{e,ped}$ and higher $n_{e,ped}$ reduces T_e at the W targets during the ELM crashes, decreasing the incident ion energies and hence the physical sputtering yield and thereby reducing the W source. Also, more gas puffing typically increases f_{ELM}, flushing more impurities from the plasma.‡

3.3. Understanding the evolution of pulse #92432:

We can try to use this insight into the effect of gas puffing on the pedestal and the W flushing by the ELMs to understand the evolution of the high-power, 3 MA baseline-scenario pulse #92432, which was discussed in detail in §2.5. A schematic representation of the causality of the underlying mechanisms is shown in Fig. 14. A breakdown of this mechanism follows:

i) Initially, the rate of gas fuelling was probably too low, causing a gradual buildup of the W content, increasing P_{Rad}^{Pl}, decreasing dW_{pl}/dt and hence causing a reduction of the ELM frequency f_{ELM} (see Fig. 6).

ii) In response to the decrease in f_{ELM}, the plasma control system initiated an increase in the gas puffing rate Γ_{D_2}, which had the opposite effect to that desired. More gas fuelling raised $n_{e,ped}$, consequently increasing P_{Rad}^{Pl}, reducing dW_{pl}/dt and hence further reducing f_{ELM}, eventually stopping the ELMs entirely.

iii) Cessation of the ELMs caused $n_{e,ped}$ to rise faster, resulting in an even faster increase in mantle radiation $P_{Rad}^{man} \propto \langle C_W n_e^2 \rangle_{Man}$, hence strongly reducing $P_{Sep}^{iELM} = P_{l,th} - P_{Rad}^{Pl}$.

iv) Once P_{Sep}^{iELM} falls sufficiently, this triggers an H/L-transition, which rapidly reduces $n_{e,ped}$ and increases R/L_{n_e} in the mantle region.

v) The increased $\langle R/L_{n_e} \rangle_{man}$ then causes sudden reversal of the neo-classical convection ($\langle \zeta_{NC} \rangle_{man} < 0$), driving the W impurities into the plasma core, causing a reduction in $T_{e,0}$, a collapse in W_{pl}, ending the high-performance phase of the pulse.

Note that this particular pulse does in fact recover from the W accumulation event. The L-mode phase is followed by another period of ELMy H-mode, albeit with higher P_{Rad} and reduced energy confinement.

‡ Stability analysis reveals that at high puffing rates, when the pedestal collisionality $\nu_{\star,e}$ is higher, the ELMs are triggered at well below the peeling-ballooning boundary and have more the character of resistive, type-III than type-I ELMs [10].
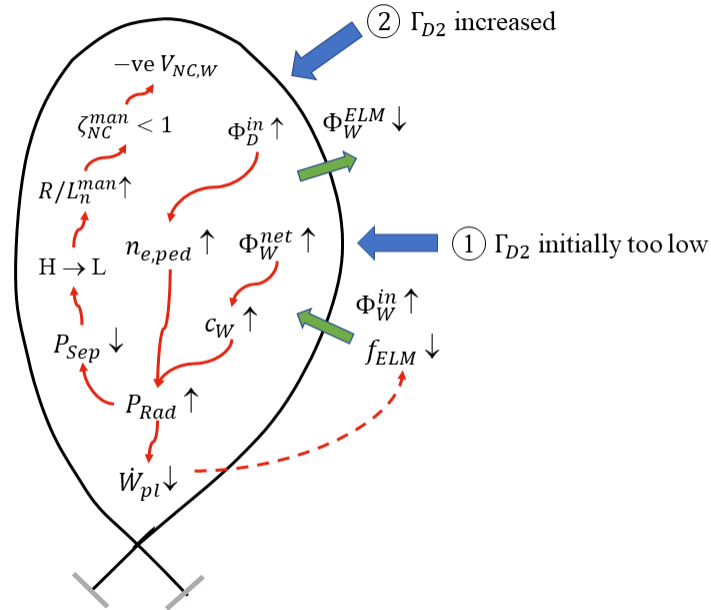
Figure 14: *Schematic representation of the factors affecting the evolution of the high-power baseline scenario JET-ILW pulse #92432 at: (1) the initial phase and (2) after the feedback system increases the gas puffing rate Γ_{D_2} to try to control the W influx.*

3.4. W impurity retention and redeposition in the divertor

The fraction of radiated power $\mathcal{F}_{Rad}$ is higher in the pellet+gas-fuelled pulse #96713 compared to that in the gas-fuelled pulse #94980, in spite of the fact that on-average, the level of inter-ELM Be influx $\langle\Gamma_{Be}\rangle$ from the target is comparatively lower (see Fig. 1 (f,g). Although the level of ELM-sputtered W from the targets is lower in in pulse #96713, the W concentration in the mantle $\langle C_W\rangle_{man}$ is higher than in pulse #94980 (see Fig. 7 (a)). This implies that the retention [56, 58] and/or prompt re-deposition [3] of the sputtered W in the divertor is less efficient in pulse #96713, which has a lower ($\sim 45\%$) gas fuelling rate than that in pulse #94980.

The process of prompt redeposition of the sputtered W^0 is due to singly ionized W^+ ions being redeposited with their first Larmor orbit onto the target. This occurs because the Larmor radius ρ_{W^+} of the heavy ($m_W/m_p \sim 183$) W^+ ions can be larger than the ionization length $L_0\S$ of the sputtered W^0 atoms [3]. The fraction of ions redeposited to the target f_{dep} decreases with the ratio $p = L_0/\rho_{W^+}$, which decreases with increasing density $n_{e,t}$ and electron temperature $T_{e,t}$ at the target. It is hence difficult to predict the effect of increasing the gas puffing on f_{dep} without complex modelling, e.g. with the kinetic impurity simulation code ERO [59], and knowledge of how $n_{e,t}$ and $T_{e,t}$ respond to the changes in fuelling.

The relatively higher $\sim \times 1.5$ concentration of W in the pellet+gas fuelled pulse #96713 compared to that in the gas fuelled pulse #94980 might also be a sign of reduced retention

$\S$ The ionisation length is defined as $L_0 = v_0/(S_0 n_e)$, where S_0 is the ionisation rate coefficient of the W_0 atoms and v_0 is their speed.)

of the sputtered W in the divertor. Modelling the transport of W ($Z_W = 74$), which has many ionisation states, in the SOL plasma is computationally extremely complex. Some insight into the processes involved can be gleaned from inspection of the parallel force balance on the impurity ions, which is stated as Eq. 1 of Ref. [56]. The relevant terms (where I represents impurity ions) are: (i) $m_i n_i n_I \langle \sigma_i v \rangle (U_{\parallel,i} - U_{\parallel,I})$ representing friction with other ion species; and (ii) $\alpha_{I,i} Z_I^2 n_I \nabla_\parallel T_I$ and $\alpha_{I,e} Z_I^2 n_I \nabla_\parallel T_e$ representing thermal forces due to the parallel temperature gradients of the ions and electrons. Here, $U_{\parallel,i/I}$ are the average parallel flow speeds of the respective ions i/I, $\langle \sigma_i v \rangle$ is the momentum exchange rate between ions and impurities and the $\alpha_{I,i/e}$ are coefficients for the ion/electron thermal forces.

It might be expected that, with an increased gas fuelling rate $\Gamma_{D2,gas}$ into the main chamber, that with the increased flow of D^+ ions through the SOL to the divertor, the parallel friction force (i) might increase, thereby enhancing the retention of the W impurities in the divertor. A higher parallel temperature gradient in the SOL would, however, act to reduce the impurity retention by increasing the thermal forces (ii), which are directed away from the target. Without detailed modelling with a SOL transport code, it is not easy to determine how $\nabla_\parallel T_e$ will change along the SOL in response to changes in the fuelling and how these changes will influence the impurity retention.

In conclusion, it may well be that increased W retention and also an increase in the prompt redeposition fraction with a higher $n_{e,t}$ at higher fuelling rate might explain the lower W concentration in pulse #94980 c.f. that in pulse #96713. Exhaustive modelling, e.g. with a SOL transport code such as SOLPS [60] or the latest ITER version SOLPS-ITER [61], is required to elucidate these effects further.

Finally, it is worth noting that, if there is a balance between the incident Be flux to the target and that sputtered during the inter-ELM periods, the comparatively lower intra-ELM Be influx in pulse #96713 implies, a lower rate of Be sputtering by the ELMs from the main chamber walls, which are faced with Be tiles. The ELM-sputtered Be influx from the walls might be expected to decrease with a lower neutral gas density in the plasma-wall interspace, resulting from reduced gas puffing into the main chamber in pulses with pellet+gas fuelling.

4. Conclusions

ITER-baseline scenario pulses typically operate at a higher plasma current I_p and consequently, lower $\beta_N = \beta_T(B_t/aI_p) \sim 1.8 - 2$† and lower edge safety factor $q_{95} \sim 3$, e.g. than hybrid-scenario pulses, which operate at lower I_p and hence higher $\beta_N \sim 2 - 3$ and $q_{95} \sim 4$. Because the pedestal density $n_{e,ped}$ increases with I_p [11], the higher $I_p \leq 4\,\mathrm{MA}$ of baseline-scenario pulses results in a relatively higher $n_{e,ped}$ and less peaked n_e profile ($n_{e,0}/\bar{n}_e \sim 1.3$) than in hybrid-scenario pulses with $n_{e,0}/\bar{n}_e \sim 2.2$.

The high $n_{e,ped}$ and low n_e peaking in baseline-scenario pulses has a fortuitous effect on the impurity transport and hence the radiation, which favours steady-state ELMy H-mode operation. The weak n_e gradient and hence low normalised gradient R/L_{n_i} across the core plasma compared to that of T_i, typically results in outward neo-classical impurity convection $\zeta_{NC} = R/2L_{T_i} - R/L_{n_i} > 0$ and hence a hollow impurity density profile. This localises the strongly radiating W impurities to the mantle region, where they can be efficiently flushed from the confined plasma by the ELMs.

This strong W radiation from the mantle has a dominant effect on the electron power

---

† The normalised plasma pressure (toroidal beta) is defined as $\beta_T = \langle p_{pl} \rangle / (B_{t,0}/2\mu_0)$, where $\langle p_{pl} \rangle$ is the volume-averaged total plasma pressure.

balance there and, without sufficiently efficient flushing by the ELMs, this can reduce the power crossing the separatrix P_{Sep}, hence slowing and even stopping the ELMs altogether, which often causes a runaway radiation event, an H/L-transition and sudden impurity accumulation. This is one of the main causes of the higher disruptivity of high-power, H-mode pulses in JET-ILW [5].

Note that, because hybrid-scenario pulses are run at lower I_p and higher β_N, these operate with a lower $n_{e,ped}$ and hence more peaked n_e profile. Consequently, such pulses are more prone to core W accumulation and can often suffer from radiation collapse of the central electron temperature, leading to a disruption. In such pulses, which are characterised by a broad, elevated q profile with $q_0 \gtrsim 1.5$, the W accumulation is usually triggered by low-n neo-classical tearing modes (NTMs), which are destabilised at low-order rational surfaces, e.g. $m/n = 3/2, 4/3, ...$ The physics of this process has been investigated in detail in Ref. [16].

As mentioned earlier, it has recently been demonstrated that optimised gas fuelling during the initial current ramp phase, can result in a hot, low collisionality pedestal, which effectively screens out the high-Z impurities from the confined plasma [17]. Similar analysis of the ELM flushing in such optimised, high-performance hybrid-scenario pulses has shown that the behaviour of the W impurities is quite different to that observed in baseline pulses, i.e. the ELMs do not flush but instead allow W to enter the confined plasma, which is then removed during the inter-ELM periods by outward neo-classical convection across the pedestal [78].

This 'vicious circle', i.e. the strong mantle radiation slowing and thereby stopping the ELMs flushing out the W impurities, in baseline-scenario pulses as illustrated by the radiation 'event' in pulse #92432 (see §2.5), can be avoided by maintaining regular ELMs by the injection of small ELM-pacing pellets. The primary, beneficial effect of the ELM-pacing pellets, at a frequency $f_{Pel} \sim 25 - 45\,\mathrm{Hz}$ into such pulses, is to maintain a regular ELM frequency $f_{ELM} \gtrsim f_{Pel}$, preventing the occurrence of ELM-free H*-phases longer in duration than $\tau_{Pel} = 1/f_{Pel} \sim 20 - 40\,\mathrm{ms}$, which can lead to an H/L-transition and subsequent W accumulation or sometimes a disruption due to the strong radiation from the mantle.

A secondary, beneficial effect is that the use of the pacing pellets, which also fuel the plasma, allows operation with a reduced D_2 puffing rate into the main chamber, e.g. in pulse #96713 the 45 Hz pellets provide $\sim 60\%$ of the total D_2 fuelling rate. It is well established that an increased rate of gas fuelling is detrimental to the pedestal confinement and hence to the overall energy confinement, so the use of the pacing pellets allows the duration of the ELMy H-mode phase to be extended, while also maintaining good overall energy confinement.

The capability to run high-power plasmas with $P_{in} \lesssim 40\,\mathrm{MW}$, yielding a D-D neutron rate of $\Gamma_{n,DD} \gtrsim 5 \times 10^{16}\,\mathrm{n/s}$ (equivalent to a D-T fusion power $P_{DT} \sim 15\,\mathrm{MW}$) sustained for 5 s is one of the key performance indicators (KPI) for the JET-ILW C38 campaign, which is preparing for the forthcoming D-T campaign (DTE2). The evolution of the best performing, unseeded ITER-baseline scenario pulse #96482 achieved so far with pellets+gas fuelling is shown in Fig. 15. This pulse achieved a maximum D-D neutron rate of $\Gamma_{n,DD} \sim 4.15 \times 10^{16}\,\mathrm{n/s}$, with an average over the 5 s period $8-13\,\mathrm{s}$ of $\langle \Gamma_{n,DD} \rangle \sim 2.6 \times 10^{16}\,\mathrm{n/s}$‡.

It should be noted that record performance for an ITER-baseline scenario pulse in JET-ILW has been achieved so far using Ne impurity seeding in the $3\,\mathrm{MA}/2.8\,\mathrm{T}$ pulse #96994 with 31 MW heating power [17]. With a Ne seeding rate of $\Gamma_{Ne} \sim 0.5 \times 10^{22}\,\mathrm{e/s}$ and 45 Hz D_2 ELM pacing pellets, this pulse achieved a confinement enhancement factor $H_{98,y2} \sim 1.1$ and a D-D neutron yield of $\langle \Gamma_{n,DD} \rangle \sim 3.1 \times 10^{16}\,\mathrm{n/s}$ averaged over 5 s.

In such high-power, pellet+gas fuelled, ITER-baseline pulses, the improved energy

---

‡ Over the 3 s period of pulse #96482, $10-13\,\mathrm{s}$, $\Gamma_{n,DD} \sim 3.1 \times 10^{16}\,\mathrm{n/s}$.
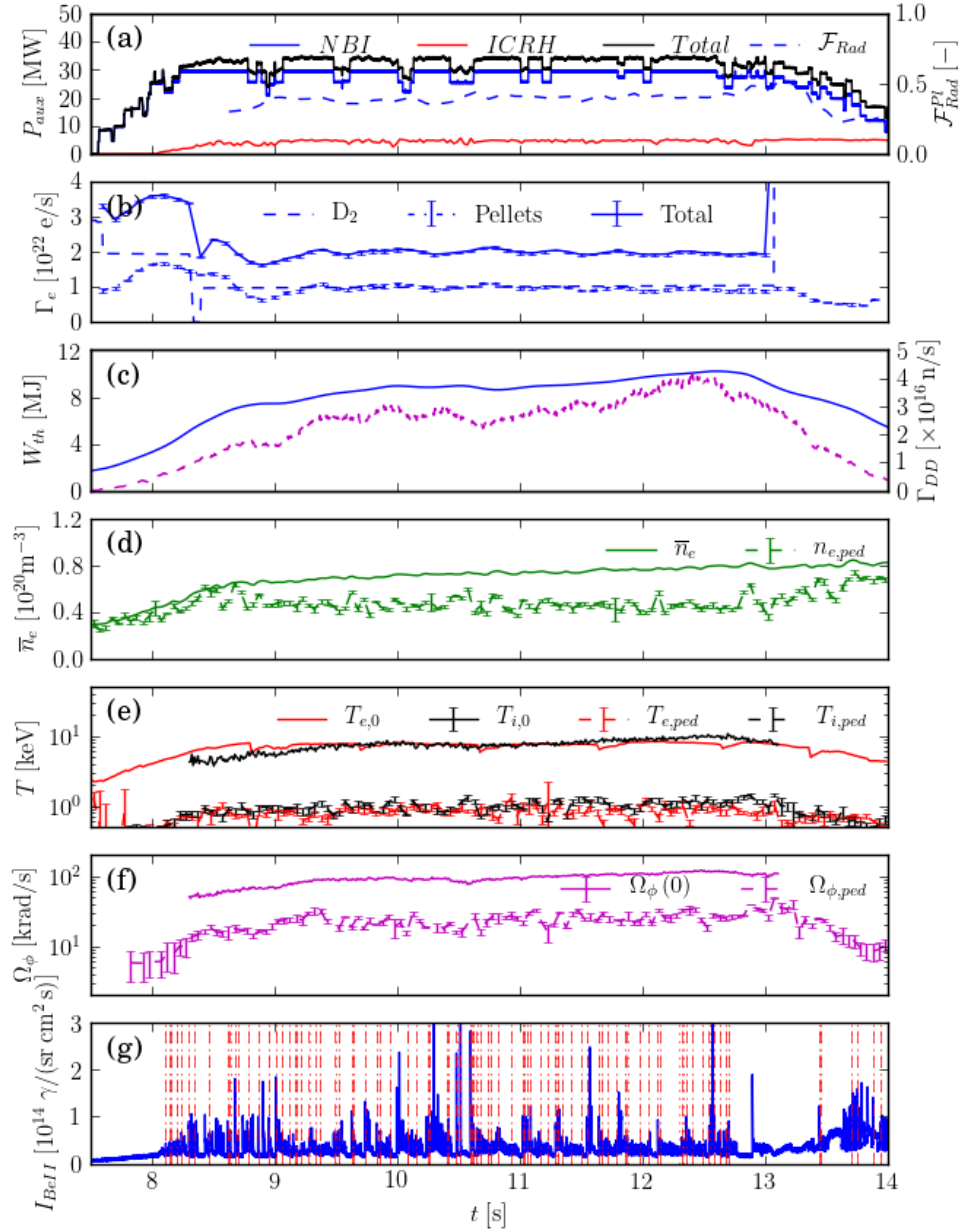
Figure 15: *Evolution of high-performance* $3.5\,\mathrm{MA}/3.3\,\mathrm{T}$ *ITER-baseline scenario pulse #96482 with the record averaged 'flat-top' D-D neutron rate for an unseeded pulse, showing: (a) total absorbed additional heating power* P_{abs} *(solid) and radiated power fraction* $\mathcal{F}_{Rad} = P_{Rad}/P_{abs}$ *(dashed); (b)* D_2 *gas fuelling rate* $\Gamma_{D2,gas}$ *(dashed), smoothed pellet fuelling rate* $\Gamma_{D2,pel}$ *(dot-dashed) and total fuelling rate* $\Gamma_{D2} = \Gamma_{D2,gas} + \Gamma_{D2,pel}$ *(solid); (c) total MHD stored energy* W_{th} *(solid) and H-mode confinement enhancement factor* $H_{98,y2}$ *(dashed); (d) mid-plane, line-averaged density* $\bar{n}_e$ *(solid) and D-D neutron rate* $\Gamma_{n,DD}$ *[e/s] (dashed); (e) axial electron and ion temperatures* $T_{e,0}\&T_{i,0}$ *(solid) and pedestal temperatures* $T_{e,ped}\&T_{i,ped}$ *(dashed), (f) axial* $\Omega_{\phi,0}$ *and pedestal* $\Omega_{\phi,ped}$ *toroidal rotation rates, (g) the ELM behaviour from a visible* $\mathrm{Be\,II}$ *line viewing the outer divertor target.*

confinement is mainly caused by a increase in the ion energy confinement in the plasma core, relative to that of the electrons, rather than increased pedestal energy confinement [23]. This has several causes: (i) Decreased $n_{e,ped}$ and hence increased n_e peaking, results in more central NBI power and torque deposition; (ii) Increased toroidal rotation rate Ω_ϕ, and hence increased $E{\times}B$ flow shear across the core gradient region; (iii) A higher T_i/T_e ratio across the core plasma, which results in an increased fraction of beam heating of the ions and is also stabilising to ITG turbulence and hence reinforces turbulence suppression by the $E{\times}B$ flow shear. As well as these effects, in high-power JET-ILW pulses, the fast particle pressure p_{fp} can also play a role in stabilisation of ITG turbulence [79, 80].

A 'virtuous circle' due to synergy between the increase in core core confinement and pedestal stability was suggested in Ref. [62]. The proposed mechanism is that a larger Shafranov shift due to higher β_N favours pedestal stability [60], thereby allowing a higher $p_{e,ped}$, which can then lead to an improvement of core confinement if the core heat transport is 'stiff'. Note, however, that the time-averaged pedestal energy $\langle W_{th,ped} \rangle$ is not significantly higher in the pellet+gas fuelled pulse #96713 compared to that in the gas fuelled pulse #94980 investigated here. Also, the improved core confinement in #96713 is likely due instead to *decreased* stiffness [63] of ion heat transport due to the relatively higher rotational $E{\times}B$ shear in pulse #96713.

There are other, more subtle and mainly beneficial effects of the ELM-pacing pellets. The change in ELM characteristics to typically smaller amplitude, compound ELMs reduces time-averaged ELM-sputtered impurity influxes. There is also a temporary effect of the pellets on the pedestal gradients, decreasing the impurity convection across the pedestal and increasing their localisation to the mantle. However, the effect of the subsequent small, rapid ELMs on the mantle gradients is to reduce the efficacy of neo-classical impurity screening from the core.

Further pulses are to be run during the C38 campaign on JET-ILW at higher plasma current $I_p \lesssim 3.6 - 4.0$ MA, so it will be of interest to determine whether this increase results in an overall improvement in energy confinement. Whereas the $ITER - H98P(y, 2)$ scaling predicts increased energy confinement ($\tau_{E,th} \propto I_p^{0.9}$), this may be offset by a broader NBI power deposition profile with the increased pedestal density expected at high plasma current [11]. Higher $n_{e,ped}$ will increase the outward neo-classical convection of the W impurities, hollowing their density profile, and hence promote their flushing from the confined plasma by ELMs.

A risk with relying on pellet injection to control the W impurity content by promoting frequent ELMs is that any 'missing' pellets due to malfunction of the injector or pellets shattering in the flight tube would result in longer ELM-free phases, risking the occurrence of a radiation induced disruption. This places high demand on the reliability of the pellet injectors on ITER or a future fusion reactor.

It should be noted that high-performance H-mode operation is possible in JET-ILW without any gas or pellet fuelling during the ELMy H-mode phase. The evolution of such a 'zero-gas' 3 MA pulse with 27 MW heating power is shown in Fig. F1 of §Appendix F, which ran at low $f_{GW} \gtrsim 0.5$ and exhibited high $T_i \lesssim 10$ keV across core and pedestal and very high toroidal rotation $\Omega_\phi \lesssim 115$ krad/s. Some ELMs and neo-classical impurity screening due to the high core T_i gradient did allow this pulse to run without severe W accumulation [81]. However, in such pulses the radiated power fraction $\mathcal{F}_{Rad}$ continually increases, eventually resulting in a disruption unless strong gas puffing is used to initiate a controlled termination.

Acknowledgements

References

[1] Garzotti L *et al* 2019 *Nucl. Fusion* **59** 076037
[2] Hinnov E *et al* 1978 *Nucl. Fus.* **18** 1305
[3] Naujoks D *et al* 1996 *Nucl. Fus.* **36** 671
[4] Lux H *et al* 2014 *ADAS Workshop 2014, Cosner's House, Abingdon, UK*
[5] Pucella G *et al* 2021 *Nucl. Fusion* **61** 046020
[6] Lerche E *et al* 2016 *Nucl. Fusion* **56** 036022
[7] Giroud C *et al* 2013 *Nucl. Fusion* **53** 113025
[8] Field A R *et al* 2020 *Plasma Phys. and Contr. Fusion* **62** 055010
[9] Hatch D R *et al* 2019 *Direct gyrokinetic simulations of JET-ILW and JET-C pedestal transport* submitted to Nucl. Fusion.
[10] Maggi C F *et al* 2015 *Nucl. Fusion* **55** 113031
[11] Kallenbach A *et al* 2002 *Nucl. Fusion* **42** 1184
[12] Hatch D R *et al* 2016 *Nucl. Fusion* **56** 104003
[13] Hatch D R *et al* 2017 *Nucl. Fusion* **57** 036020
[14] Kotchenreuther M *et al* 2017 *Nucl. Fusion* **57** 064001
[15] Joffrin E *et al* 2019 *Nucl. Fusion* **59** 112021
[16] Hender T C *et al* 2016 *Nucl. Fusion* **56** 066022
[17] Garcia J, Casson F J, Challis C *et al Integrated scenario development at JET for DT operation and ITER risk mitigation*, 2020 IAEA Fusion Energy Conference, ??/??.
[18] Geraud A *et al* 2012 *27th SOFT Conf. (Liège, Belgium)* P1.31 and http://sciconf.org/soft2012/ip/topic/c/session/p1/paper/31
[19] Lang P T *et al* 2013 *Nucl. Fusion* 53 073010
[20] Lawson J D 1955 *Proceedings of the Physical Society*, **B 70 (1)** 6–10
[21] ITER physics Expert Group on Confinement and Transport *et al* 1999 *Nucl. Fusion* **39** 2175
[22] Field A R *et al* 2004 *Plasma Phys. Control. Fusion* 46 981
[23] Kim H T *et al* 2018 *Nucl. Fusion* **58** 036020
[24] Hawryluk R 1979 *An empirical approach to tokamak transport, Physics of plasmas close to thermonuclear conditions (Varenna, Italy, 27 Aug-8 Sept 1979)*
[25] Lao L *et al* 1985 *Nucl. Fusion* **25** 1611
[26] Appel L *et al* 2006 *Proc 33rd Conf. on Contr. Fusion and Plasma Phys., Rome, EPS Geneva (2006)* **??** VI ??
[27] Ingesson L C *et al* 1998 *Nucl. Fus.* **38** 11 1675
[28] Huber A *et al* 2007 *Proc. 24th Symp. on Fusion Technology SOFT-24, Fusion Eng. and Design* **82** 5–14 1327–1334
[29] Goldston R 1985 *'Topics on confinement analysis of tokamaks with auxilliary heating', in Basic Processes of Toroidal Fusion Plasmas (Proc. Course and Workshop Varenna, Italy, 1985) EUR-10418-EU, Brussels 1986, Vol. 1, p. 165*
[30] Connor J W and Wilson H R 1994 *Plas. Phys. Control. Fusion* **36** 719
[31] Garbet X *et al* 2004 *Plas. Phys. Control. Fusion* **46** B557
[32] Hahm T T and Burrell K H 1995 *et al Phys. Plasmas* **2** 1648
[33] Highcock E G *et al* 2012 *Phys. Rev. Lett.* **109** 265001

[34] Houlberg W A *et al* 1985 *Phys. Plasmas* **4** 3230
[35] Kotschenreuther M *et al* 2019 *Nucl. Fusion* **59** 096001
[36] Wesson J A *et al* 1997 *Nucl. Fusion* **37** 578
[37] Angioni C *et al* 2015 *Phys. Plasmas* **22** 055902
[38] Pasqualotto R *et al* 2004 *Rev. Sci. Inst.* **75** 10 3891–3893
[39] Andrew Y *et al* 2006 *Rev. Sci. Inst.* **77** 10E913
[40] Angioni C *et al* 2014 *Plasma Phys. and Contr. Fusion* **56** 124001
[41] Fedorczak N *et al* 2015 *J. Nucl. Mat.* **463** 85-90
[42] Summers H P *et al* 2006 *Plasma Phys. and Contr. Fusion* **48** 263
[43] Henderson S S *et al* 2017 *Plasma Phys. and Contr. Fusion* **59** 055010
[44] Martin Y R *et al* 2008 *J. Phys.: Conf. Series* **123** 012033
[45] Field A R *et al* 2017 *Plas. Phys. Control. Fusion* **59** 095003
[46] Dickinson D *et al* 2011 *Plasma Phys. and Contr. Fusion* **53** 115010
[47] Fundamenski W and Pitts R A 2007 *J. Nucl. Mater.* **363-365** 319
[48] Snyder P B *et al* 2007 *Nucl. Fusion* **47** 961
[49] Huber A 2019 *et al Nucl. Mat. Energy* **18** 118-124
[50] Den Harder N 2016 *Nucl. Fusion* **56** 026014
[51] Fussmann G *et al* 1991 *Plasma Phys. Control. Fusion* **33** 1677
[52] Maggi C F *et al* 2017 *Nucl. Fusion* **57** 11612
[53] Hatch D P *et al* 2018 *Plas. Phys. Control. Fusion* **60** 084003
[54] Weisen H *et al* 2005 *Nucl. Fusion* **45** L1
[55] Garzotti L, Valovič M, Garbet X *et al* 2006 *Nucl. Fusion* **46** 994
[56] Senichenkov I U *et al* 2019 *Plasma Phys. and Contr. Fusion* **61** 045013
[57] Kirchner A *et al* 2019 *Nucl. Mat. Energy* **18** 239-244
[58] Stangeby P 2000 *IOP Physics Publishing, Bristol & Philadelphia* ISBN- **7503 0559 2**
[59] Naujoks D *et al* 1994 *J. Nucl. Mater.* **210** 43
[60] Schneider R *et al* 2006 *Contrib. Plasma Phys.* **46** 3-191
[61] Wiesen S *et al* 2015 *J. Nucl. Mater.* **463** 480-4
[62] Challis C *et al* 2015 *Nucl. Fusion* **55** 053031
[63] Mantica P *et al* 2009 *Phys. Rev. Lett.* **102** 175002
[64] Field A R *et al* 1996 *Nucl. Fusion* **36** 119
[65] Behringer K *et al* 1985 *Plas. Phys. Control. Fusion* **31** 2059
[66] Born M and Wolf E 1980 *Principles of Optics, Permagon Press*, ISBN **978-0-08-026482-0**
[67] Borodin D *et al* 2016 *Nucl. Mat. & Energy* **9** 604-609
[68] Brezinsek S *et al* 2011 *Phys. Scr.* **T145** 014016
[69] Beigman I *et al* 2007 *Plas. Phys. Control. Fusion* **49** 1833
[70] Hawkes N C and Peacock N J *et al* 1992 *Rev. Sci. Inst.* **63** 5164
[71] Simpson J *et al* 2019 *Nucl. Mat. Energy* **20** 100599
[72] Pankin A *et al* 2004 *Comp. Phys. Comm.* **159** 157–184
[73] Brambilla M 1999 *Plas. Phys. Control. Fusion* **41** 1
[74] Sertoli M *et al* 2018 *Rev. Sci. Inst.* **89** 113501
[75] Newton S and Helander P 2006 *Plasma Phys. and Contr. Fusion* **13** 012505
[76] Lee J *et al* 2014 *Nucl. Fusion* **54** 022002
[77] Hawryluk R J *et al* 1979 *Nucl. Fusion* **19** 1307
[78] Field A R *et al* , *Screening of high-Z impurities by low-collisionality pedestal in high-performance, hybrid-scenario H-mode plasmas in JET-ILW*, paper in preparation.
[79] Citrin J, Jenko F, Mantica P *et al* 2013 *Phys. Rev. Lett.* 111 155001
[80] Citrin J, Garcia J, Görler *et al* 2015 *Plasma Phys. Control. Fusion* 57 014032
[81] Garcia J, de la Luna E, Sertoli M *et al New plasma regimes with small ELMs and high confinement at the Joint European Torus* submitted to *Phys. Rev. Lett.* April 2021

Appendices

Appendix A. Effect of gas puffing and pacing pellets on ELM behaviour

In this section, the influence of the gas fuelling rate on the ELM behaviour and also their response to the ELM-pacing pellets at different pellet injection frequencies is investigated by a statistical analysis of their amplitudes and frequencies.

Rather than the ELM energy losses ΔW_{ELM}, which is difficult to evaluate from magnetic measurements on JET-ILW, particularly at high ELM frequency f_{ELM} [8], here, the peak intensity of a visible Be II line observed viewing the outer divertor target is used as a metric for the ELM amplitude A_{ELM}. As sputtering of W by Be^{4+} ions is expected to dominate over that by D^+ ions, this also provides a relative measure of the ELM-sputtered impurity source. The instantaneous ELM frequency is defined as $f_{ELM} = 1/\tau_{ELM}$, where τ_{ELM} is the time duration from the peak of the Be II intensity signal to that of the preceding ELM. Note that by averaging the inter-ELM durations, a meaningful measure of the average ELM frequency can be calculated, i.e. $\langle f_{ELM} \rangle = 1/\langle \tau_{ELM} \rangle$, where $\langle \tau_{ELM} \rangle$ is the average inter-ELM period over a given time period.

Histograms of the ELM amplitude A_{ELM} and instantaneous frequency f_{ELM} for four
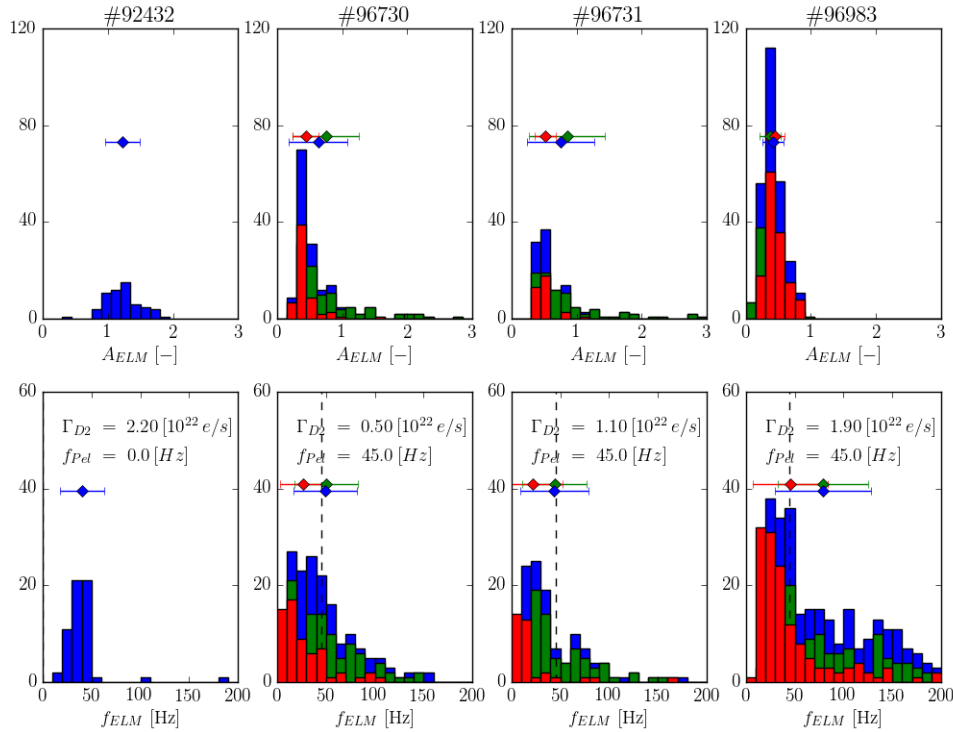

Figure A1: *PDFs of the ELM amplitude A_{ELM} (peak Be II line intensity viewing the outer divertor target – bottom) and instantaneous ELM frequency ($f_{ELM} = 1/\tau_{ELM}$, where τ_{ELM} is the ELM period – top) for four high-power, 3 MA/2.8 T JET-ILW baseline pulses at different fuelling rates Γ_{D2} without pellets (#92432 @ 2.2×10^{22} e/s) and with pacing pellets (requested $f_{Pel} \sim 45 - 35$ Hz): #96730 @ 0.5×10^{22} e/s, #96731 @ 1.1×10^{22} e/s & #96983 @ 1.9×10^{22} e/s (vertical dashed line). Separate PDFs are shown for all ELMs (blue) and pellet-triggered (red) and natural (green) ELMs in pulses with pacing pellets. The error bars show the mean and standard deviation of the A_{ELM} and f_{ELM} data for each PDF (♦).*

$3\,\mathrm{MA}/2.7\,\mathrm{T}$ high-power, ITER-baseline scenario pulses with $31-34\,\mathrm{MW}$ of additional heating power are shown in Fig. A1. The pulse #92432 has only D_2 gas fuelling at a rate of $\Gamma_{D2} \sim 2.2 \times 10^{22}\,\mathrm{e/s}$ and exhibits quite regular, type-I ELMs at an average frequency $f_{ELM} \sim 40\,\mathrm{Hz}$. Note that later in this pulse, the ELM period increases due to a gradual increase in radiation from W impurities (see §2.5).

The other three pulses shown in Fig. A1 (b-c) all have ELM-pacing pellets injected at a requested frequency $f_{Pel} \sim 45-35\,\mathrm{Hz}$. Separate histograms are shown for: all ELMs (blue), pellet-triggered (red) and natural (green) ELMs. Whether or not the ELMs are pellet triggered is determined from the coincidence (within a time window $-1\,\mathrm{ms} \leq \Delta t \leq 5\,\mathrm{ms}$) of the peak ELM amplitude and the arrival time of the pellets at the separatrix, which is estimated from the time they pass the final microwave cavity in the flight tube and their injection speed ($\sim 300\,\mathrm{m/s}$). Average values and standard deviations of A_{ELM} and f_{ELM} are indicated by the upper data points with the horizontal error bars for each ELM type.

The three pulses with the $45-35\,\mathrm{Hz}$ ELM-pacing pellets have different D_2 fuelling rates of $\Gamma_{D2,gas} \sim 0.5, 1.1\,\&\,1.9 \times 10^{22}\,\mathrm{e/s}$. In the pulses with pacing pellets the pellet-triggered ELM frequency is about half that for the natural ELMs, i.e. $f_{ELM}^{PT} \sim f_{ELM}^{Nat}$. Only at the highest fuelling rate ($1.9 \times 10^{22}\,\mathrm{e/s}$) is the pellet-triggered ELMs frequency equal to that of the pellets, i.e. $f_{ELM}^{PT} \sim f_{Pel}$. At the lower fuelling rates, $f_{ELM}^{PT} \sim 0.5 \times f_{Pel}$, while for the natural ELMs $f_{ELM}^{Nat} \sim f_{Pel}$. As there are some missing pellets ablated in the flight tube and because not
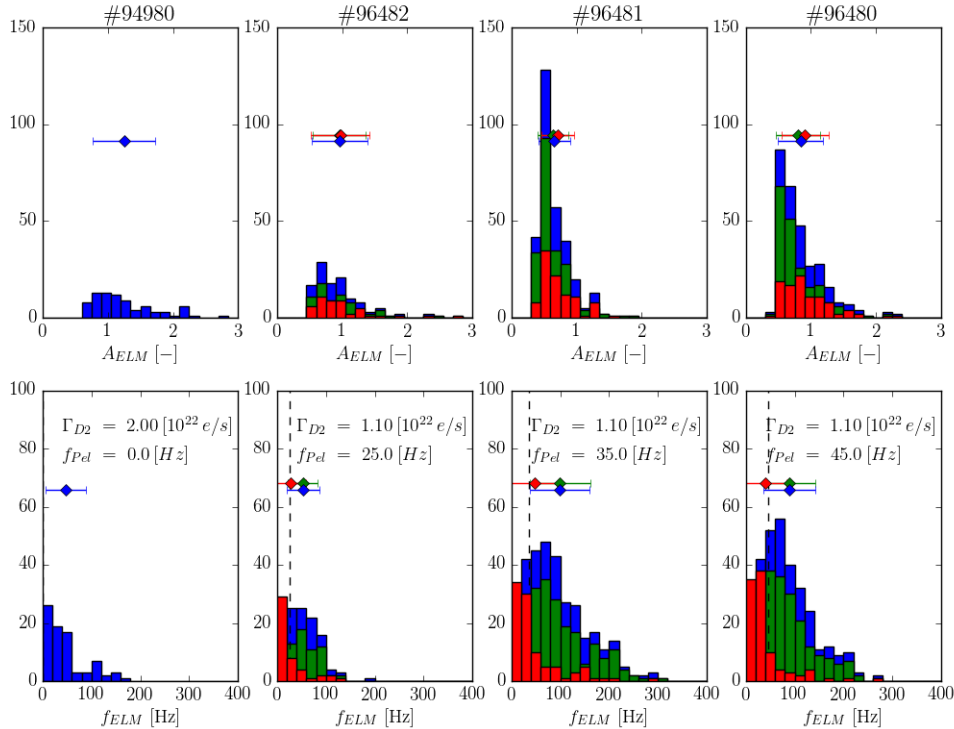

Figure A2: *Similarly to Fig. A1, PDFs of the ELM amplitude A_{ELM} (bottom) and ELM frequency f_{ELM} (top) for four high-power, $3.5\,\mathrm{MA}/3.35\,\mathrm{T}$ JET-ILW baseline pulses at different fuelling rates without pellets (#94980, $\Gamma_{D2} = 2 \times 10^{22}\,\mathrm{e/s}$) and at a lower fuelling rate $\Gamma_{D2} = 1.1 \times 10^{22}\,\mathrm{e/s}$ with different requested pacing pellet frequencies f_{Pel}: (#96482 @ 25 Hz, #96481 @ 35 Hz & #96480 @ 45 Hz).*

all pellets trigger ELMs, the most frequent 'modal' ELM frequency is always below f_{Pel}. The distributions are also skewed to higher f_{ELM} by the many small amplitude, high frequency ELMs, giving a 'compound' nature to the ELMs in pulses with pacing pellets, e.g. as shown in Fig. 1 (g).

As the gas fuelling rate is increased, the relative number of the small, high frequency ELMs increases and there are fewer of the larger amplitude ELMs that are present at lower fuelling rates or in the pulse without pellets. Note that the time-averaged fuelling rate from the pellets is estimated to be $\Gamma_{D2,pel} \sim 1.3 \times 10^{22}$ e/s, so for the pulse #96731 with the mid-range gas-puffing rate, the total fuelling rate is about the same as that in the gas-only pulse #92432. In spite of this, the pulse with the pellets exhibits the compound ELMs, i.e. the bursts of small ELMs following the pellet-triggered ELMs.

The effect of increasing the requested pellet frequency f_{Pel} on the ELM characteristics is investigated in Fig. A2, which shows similar histograms to those shown in Fig. A1 but for a series of $3.5\,\text{MA}/3.35\,\text{T}$ ITER-baseline scenario pulses with $31-35\,\text{MW}$ of additional heating power. All three pulses with the ELM-pacing pellets have the same gas fuelling rate of $\Gamma_{D2,gas} \sim 1.1 \times 10^{22}$ e/s. The fuelling rate for the pulse #94980 without pellets of $\Gamma_{D2,gas} \sim 2.3 \times 10^{22}$ e/s approximately matches that for the pulse #96480 with the $45\,\text{Hz}$ pellets.

It is evident that, even at the lowest pellet frequency $f_{Pel} \sim 25\,\text{Hz}$, the pellets cause a change in the ELM character to a compound nature. Also, as the pellet injection frequency and hence the total fuelling rate is increased, there are more, small amplitude, high-frequency ELMs. In these higher-current $3.5\,\text{MA}$ pulses, the frequency of the pellet-triggered ELMs is close to that of the pellets, i.e. $f_{ELM}^{PT} \sim f_{Pel}$, while the natural ELMs have a higher frequency $f_{ELM}^{N} \sim 2 \times f_{Pel}$. It is not known why the pellets are less efficient at triggering ELMs in the lower-current $3\,\text{MA}$ pulses, in which only about half of the pellets appear to trigger ELMs, at least at the lower fuelling rates.

Appendix B. Definition of terms in the TRANSP power balance

The equations governing the power and particle balances that underlie the TRANSP calculations are stated in Ref. [24] and the balance of toroidal angular momentum is described in detail in Ref. [29]. Note that there is also a similar equation for the balance of rotational, kinetic energy W_{rot}, which couples the ion energy and momentum balances [29].

Appendix B.1. Ion and electron power balances

The power balances are expressed in terms of power densities Q and divergence of the conducted and convected heat fluxes $\nabla \cdot (q_{cond} + q_{conv})$ with units [Wm^{-3}]. For the ions, the power balance can be expressed in terms of power densities as:

$$\dot{W}_i = Q_{i,heat} + Q_{ie} - \nabla \cdot (q_{cond,i} + q_{conv,i}) - Q_{cx,net} + Q_{rot}$$

, where $\dot{W}_i = \frac{d}{dt}(\frac{3}{2}n_i T_i)$ is the rate of change of ion thermal energy density, $Q_{i,heat}$ is the total power heating the ions, Q_{ie} is the exchange power density from the electrons to the ions, $Q_{cx,net}$ is the net CX loss power and Q_{rot} is the rotational heating. The electron-ion exchange power is given as: $Q_{ie} = \frac{3}{2} n_e \frac{(T_e - T_i)}{\tau_{ie}}$, where $\tau_{ie} \propto T_e^{3/2}/n_e$ and is hence larger in the outer regions where the T_e is lower than in the core. The rotational heating Q_{rot} due to convection and friction is typically negligibly small compared to the other terms.

Each of the terms Q_X in this equation can be volume integrated $P_X(\rho'_N) = \int_0^{\rho'_{tor}} Q_X (dV/d\rho_{tor}) \, d\rho_{tor}$ to give the associated power deposited within or leaving the ρ'_{tor} flux surface. The rate of change of ion thermal energy W_i within this flux surface can then be expressed in terms of equivalent powers as:

$$\dot{W}_i = P_{heat,i} + P_{ie} - (P_{cond,i} + P_{conv,i}) - P_{cx} + P_{rot}$$

For the electrons the power balance can be similarly expressed in terms of power densities or volume integrated quantities as:

$$\dot{W}_e = Q_{e,heat} + Q_{ei} - \nabla \cdot (q_{cond,e} + q_{conv,e}) - Q_{0,ion} - Q_{Rad}$$
$$\dot{W}_e = P_{heat,e} + P_{ei} - \nabla \cdot (P_{cond,e} + P_{conv,e}) - P_{0,ion} - P_{Rad}$$

, where $Q_{0,ion}$ is the power required to ionise the neutrals and Q_{Rad} is the total radiated power density, i.e. that available from the bolometer tomography as $\langle \epsilon_{tot} \rangle$. Obviously, the ion-electron exchange power is balanced by that from the electrons to the ions, i.e. $Q_{ei} = -Q_{ie}$.

We can define two further powers for the ions: the loss power due to ion heat transport $P_{tran,i} = P_{cond,i} + P_{conv,i}$ and the total loss power from the ions $P_{loss,i} = P_{tran,i} + P_{cx}$. Similarly for the electrons: the power due to electron heat transport $P_{tran,e} = P_{cond,e} + P_{conv,e}$ and the total loss power from the electrons, including ionisation and radiation $P_{loss,e} = P_{tran,e} + P_{0,ion} + P_{Rad}$. The total transport loss power is $P_{tran} = P_{tran,e} + P_{tran,i}$.

Appendix B.2. Toroidal angular momentum balance

The balance of angular momentum of a toroidal plasma with neutral-beam-injection (NBI) heating due to toroidal rotation of the ions Ω_ϕ is described in detail in Ref. [29]. The balance between the toroidal angular momentum $L_\phi = I_\phi \Omega_\phi$, where I_ϕ is the toroidal moment of inertia of the plasma, and the net toroidal torque T_ϕ on the plasma is described by:

$$\frac{d}{dt}(I_\phi \Omega_\phi) = T_\phi$$

$$I_\phi \quad = \int \sum_i n_i m_i R^2 dV$$

$$T_\phi \quad = \int \sum_k F_k R dV$$

, where F_k are the various forces on the plasma imposed by the beam (friction with the injected fast ions, $j \times B$ forces due to fast-ion currents and thermalisation forces) and V is the plasma volume.

This balance can be expressed in terms of that of the local, flux-surface averaged, toroidal angular momentum density l_ϕ on a flux surface labeled by the normalised radial coordinate $\rho = r/a$ as:

$$\dot{l}_\phi = \tau_{\phi,in} + \tau_{\phi,iz} - \tau_{\phi,CX(net)} - \tau_{\phi,\delta} - \nabla \cdot (\Pi_{\phi,visc} + \Pi_{\phi,conv}) \tag{B.1}$$

$$l_\phi = \sum_i n_i m_i \left\langle R^2 \right\rangle \Omega_\phi \tag{B.2}$$

, where the units are $[\mathrm{Nm}^{-2}]$ and $\langle ... \rangle$ represents a flux surface average†

The various torque densities are: that due to the toroidal torque applied to the plasma by the neutral beams $\tau_{\phi,in}$, the torque due to ionisation of rotating neutral atoms and recombination of rotating ions $\tau_{\phi,iz}$, the net torque due to charge exchange reactions between the ions and cold neutral atoms $\tau_{\phi,CX(net)}$ and any torque due to toroidal field ripple $\tau_{\phi,\delta}$. Note that the term $\tau_{\phi,iz}$ is typically negligible compared to the other terms and we also neglect the ripple loss torque $\tau_{\phi,\delta}$ in the analysis presented here.

The final term $\nabla \cdot (\Pi_{\phi,visc} + \Pi_{\phi,conv})$ is the divergence of the viscous and convected fluxes of toroidal angular momentum. These fluxes can be represented in terms of the respective momentum diffusivities $\chi_{\phi,visc}$ and $\chi_{\phi,conv}$ in units of $[\mathrm{m}^2/\mathrm{s}]$ as:

$$\Pi_\phi = -\sum_i n_i m_i \chi_\phi R^2 |\nabla \rho| \partial \Omega_\phi / \partial \rho$$

Similarly to the electron and ion power balances, the local form of the toroidal momentum balance Eq. (B.1) can be radially integrated to give the toroidal momentum balance of the plasma contained within a flux surface in units of $[\mathrm{Nm}]$ as:

$$\dot{L}_\phi = T_{\phi,in} + T_{\phi,iz} - T_{\phi,CX(net)} - T_{\phi,\delta} - S(\Pi_{\phi,visc} + \Pi_{\phi,conv})$$

, where S is the surface area of the flux surface with radial coordinate ρ.

Note that there is a similar balance equation for the rotational kinetic energy $W_{rot} = \frac{1}{2} I_\phi \Omega_\phi^2$, which is obtained by taking the scalar product of Eq. (B.1) with $U_\phi = R\Omega_\phi$ (see §C of Ref. [29]). An associated additional viscous heating term, representing the work done by rotational shear against viscosity, $Q_{rot} = R_0 \Omega_\phi \nabla \cdot (\Pi_{\phi,visc} + \Pi_{\phi,conv})$, which appears in the ion energy balance, can typically be neglected compared to the other terms in Eq. (B.1).

Appendix C. Power and momentum balance analysis of #94980 and #96713

In this section results on the power balances of the ions and electrons and the balance of toroidal angular momentum for the two 3.5 MA pulses: #94980 with the high rate of gas

† The flux-surface average of any quantity X is defined as: $\langle X \rangle = [2\pi \oint dl_p (\frac{XR}{|\nabla \rho|})][\partial V/\partial \rho]^{-1}$, where l_p is the distance along a poloidal flux contour.

fuelling alone and #96713 with a similar total fuelling rate from gas and ELM pacing pellets, are presented and compared.

The primary input data for the transport analysis are the kinetic profiles (T_e, n_e, T_i and Ω_ϕ), which are obtained by fitting the raw data from the high-resolution Thomson scattering system (HRTS) [38] and the core and edge CXRS systems [39, 70]. The fits use an mtanh() function to represent the profiles over the pedestal region [46] and a third-order polynomial for the core region. Examples of the raw profiles at 11 s are shown in Fig. C1 (a) and Fig. C2 (a). As the T_i and Ω_ϕ data from the edge CXRS system on JET-ILW is considered more reliable than that from the core system, the outer two points of the core CXRS (not shown) are excluded from the fit.

Pressure constrained EFIT++ equilibrium reconstructions [26] are used to map the measurement data from major radius to the normalised flux coordinate, i.e. $\rho_{tor}(R_m)$ (where $\rho_{tor} = \sqrt{\Phi_N}$ and Φ_N is the normalised toroidal flux). Using these equilibria for the profile mapping, meaningful results can be obtained in the pedestal region with no additional constraint required to ensure a reasonable value for $T_{e,sep}$, which is typically $\sim 100\,\mathrm{eV}$ (see Ref. [71]).

For these interpretive transport calculations, time-dependent, radial profiles of flux-surface averaged densities of Be, Ni and W impurities are input to TRANSP, which are obtained from an integrated analysis described in Ref. [74], as for similar analysis presented in a previous study [8]. This analysis self-consistently fits bolometric measurements of the total emissivity, muti-channel soft x-ray (SXR) measurements and a horizontal, visible bremsstrahlung measurement of the line-average Z_{eff}, taking account of the poloidal redistribution of the impurity ions over the flux surfaces by centrifugal forces due to the toroidal rotation.

These calculations, which assume a radially constant concentration of Be impurities, yield the volume averaged quantities for the principle Be, Ni and W impurities, summarised in Table C1.

Pulse	$\langle Z_{eff} \rangle$	$\langle C_Z \rangle$ [%]			$\langle \Delta Z_{eff} \rangle$			$\mathcal{F}_{Rad,Z}$ [%]			C_{min} [%]	
#	-	Be	Ni	W	Be	Ni	W	Be	Ni	W	H	^{3}He
94980	1.6 ± 0.03	3.8	0.02	0.005	0.61	0.11	0.05	3.6	17.3	75.5	1	2.5
96713	1.6 ± 0.03	2.1	0.04	0.01	0.35	0.23	0.12	1.52	12.9	82.5	3	-

Table C1: *Time-averaged quantities over $10 - 12$ s from the integrated analysis of impurity radiation described in Ref. [74] for the two pulses for which interpretive TRANSP analysis has been performed here, stating volume-averages $\langle ... \rangle$ of: total Z_{eff} and Be, Ni and W impurity concentrations C_Z, with their incremental contributions ΔZ_{eff} to Z_{eff} and their contributions $\mathcal{F}_{Rad,Z}$ to the total radiated power. The H and ^{3}He minority ion concentrations C_{min} assumed for the TORIC calculations of the ICRH power deposition are also stated.*

For both pulses the volume-averaged $\langle Z_{eff} \rangle \sim 1.6$. Pulse #94980 has twice the concentration of Be ($C_{Be} \sim 4\%$) than pulse #96713 ($\sim 2\%$). Conversely, the volume-averaged concentrations of the heavy impurities Ni and W, which are $\mathcal{O}(10^{-4})$ are twice as high in pulse #96713 than in pulse #94980 and in both pulses the concentration of Ni is $\sim \times 4$ that of W. In spite of this, the W radiates $\gtrsim 75\%$ and the Ni $\lesssim 20\%$ of the total radiated power in both pulses. Although the Be radiates only a few % of the power, this species makes the largest contribution to Z_{eff}.

Power deposition profiles from the NBI and ICRH heating systems are calculated by the codes NUBEAM [72] and TORIC [73]. The ICRH heats the bulk plasma by means of the

cyclotron resonance of the RF waves with a minority ion species. In pulse #96713 there is a single H minority at a concentration of $\sim 3\%$, while for pulse #94980 there are both H and ^{3}He minority ions at average concentrations of $\sim 1\%$ and $\sim 2.5\%$ respectively. The presence of the heavier ^{3}He minority species is to increase fraction of ICRH power heating to the D^+ ions.

The neutral D^0 influx at the plasma boundary, which determines the edge ionisation source, is determined from a horizontal, mid-plane D_α intensity measurement by assuming a ratio of ionisations/photon $S/XB = 10$. Note that the TRANSP runs from which the results are reported here do not account for the particle source from the ablation of the D^0 pacing pellets, which are injected at the upper-HFS of the main vessel.

Appendix C.1. Results of power balance analysis

Results from the interpretive, power balance analysis of the high-power 3.5 MA pulse #94980 with the high gas fuelling rate ($\Gamma_{D2} \sim 2.3 \times 10^{22}$ e/s) are shown in Fig. C1. The derived profiles are shown averaged over the period $10 - 12$ s of the ELMy H-mode phase, while the measured raw data in Fig. C1 (a) is shown at 11.1 s.
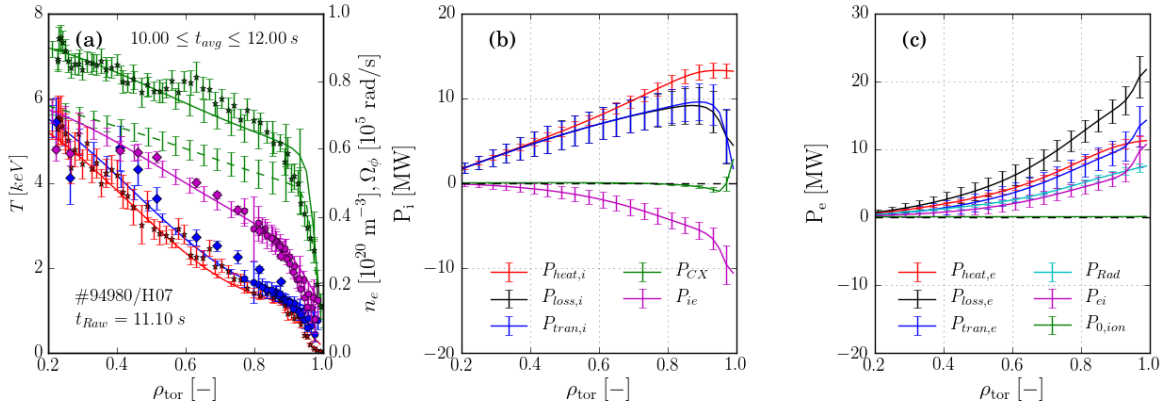
Figure C1: *Results of interpretive, power balance analysis using TRANSP of pulse #94980 (H07) showing: (a) fitted kinetic profiles T_e (red), n_e (green, solid) and n_i (green, dashed) from HRTS, T_i (blue) and Ω_ϕ (magenta) from the core and edge CXRS systems; radially integrated powers of components of the power balances of the ions (b) and the electrons (c), where the profiles are averaged over the time period $10.0 \leq t \leq 12.0$ s and the error bars represent the standard deviations of the data σ_{data}. A 'snapshot' of the raw measurement data is shown at $t_{Raw} = 11.1$ s. The various terms in the power balances are explained in §Appendix B.1.*

Components of the radially-integrated ion and electron power balances are shown in Fig. C1 (b-c). While T_i only slightly exceeds T_e across the full plasma radius, collisional exchange transfers significant power from the ions to the electrons, i.e. integrated out the pedestal top $P_{ie} \sim 6$ MW, i.e. about $\sim 50\%$ of the total ion heating $P_{heat,i}$. Consequently, at the pedestal top, similar powers are conducted through the electron and ion channels, with $P_{tran,e} \sim P_{tran,i} \sim 10$ MW, in spite of the fact that at mid-radius the integrated power heating and conducted by the ions are twice those in the electron channel. Almost half of the total loss power through the electron channel $P_{loss,e}$ is radiated, i.e. $P_{Rad}/P_{loss,e} \sim 40\%$, predominantly by the strong W emission from the mantle region.

Note that on including the heavier ^{3}He ion species in the TORIC calculations, significant ICRH power is deposited to the D^+ ions, with a ratio of on-axis power densities in [MW/m^3] of $Q_{i,RF}/Q_{e,RF} \sim 0.15/0.04 \sim 3$, while (wrongly) assuming instead a single H (3%) minority species results in insignificant core ion heating).

Results from the interpretive, power balance analysis of the high-power 3.5 MA pulse #96713 with the lower gas fuelling rate ($\Gamma_{D2,gas} \sim 1.0 \times 10^{22}$ e/s) and the $f_{Pel} \sim 45$ Hz ELM-pacing pellets, with a similar total fuelling rate as pulse #94980 are are shown in Fig. C2.
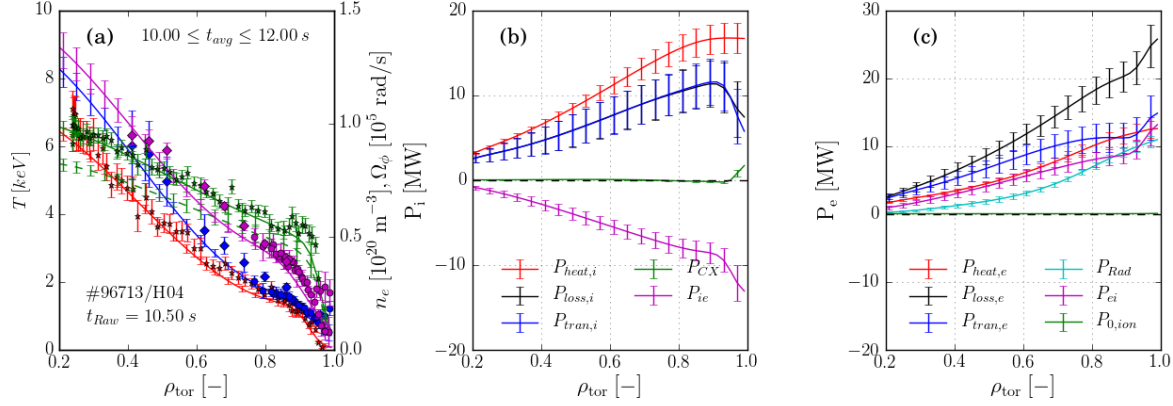
Figure C2: *Results of interpretive, power balance analysis using TRANSP of pulse #96713 (H04), where the profiles are averaged over the period $10.0 \leq t \leq 12.0$ s and a snapshot of the raw data is shown at $t_{Raw} = 10.5$ s. The definition of the quantities plotted are the same as in Fig. C1.*

The most striking difference between the kinetic profiles for these two pulses is the much higher ($\sim \times 2$) toroidal rotation rate of $\Omega_{\phi,0} \lesssim 130$ krad/s in pulse #96713, c.f. ~ 70 krad/s in pulse #94980. Also, there is a higher ratio of $T_i/T_e \sim 1.3$ across the core plasma. Quoting values at the pedestal top, the exchange heating $P_{ie} \sim 9$ MW transfers $\sim 50\%$ of the total ion heating $P_{heat,i} \sim 18$ MW to the electrons. In fact, the exchange heating of the electrons P_{ei} almost equals that from the external electron heating $P_{heat,e} \sim 11$ MW and equals the radiated power from the electrons P_{Rad}.

Hence, accounting for the ion-electron exchange power and radiation, the net transport loss power through the ion channel $P_{tran,i} \sim 12$ MW is similar in magnitude to that transported through the electron channel $P_{tran,e} \sim 11$ MW. The increased radiation in #96713 ensures that about 50% of the total electron loss power $P_{loss,e} \sim 20$ MW through the electron channel is lost by radiation (again quoting values at the pedestal top).

In both pulses, the profiles of power deposition *density* to the ions and electrons differ in that, whereas $Q_{i,heat}$ peaks on-axis, $Q_{e,heat}$ peaks in the mantle region. This is because the fraction of NBI power heating the ions ($Q_{NB,i}/(Q_{NB,i} + Q_{NB,e})$) increases with the ratio of T_e to the injection energy E_0, with $Q_{NB,e}/Q_{NB,i} > 1$ for $E_0/T_e > 15$. Consequently, the ratio of heating power to the ions relative to that to the electrons P_i/P_e is higher and also more peaked in #96713 in which $T_i/T_e > 1$ than in pulse #94980, i.e. $P_i/P_e \sim 1.33$ c.f. ~ 1.18. In spite of the fact that this pulse has only H (1%) minority ions, more ICRH power is deposited into the D^+ ions than into the electrons, with a ratio of on-axis power densities in [MW/m^3] of $Q_{i,RF}/Q_{e,RF} \sim 1.1/0.4 \sim 2.8$.

The cause of the more peaked power deposition and greater fraction of ion heating in pulse #96713 with the pellet+gas fuelling is in part the increased density peaking $\bar{n}_e/n_{e,ped}$,

mentioned in §2.1. This, together with the higher overall heating power $\sim \times 1.15$ in this pulse compared to that in pulse #94980 results in higher rotational shear and a higher T_i/T_e ratio. Because of the relatively higher radiated power in pulse #96713, the ratio of ion to electron heat fluxes q_i/q_e is close to unity at the pedestal top in both pulses. Transport in these two pulses are compared in §2.2, revealing modest differences in the heat and momentum diffusivities and hence changes to the prevailing transport mechanisms induced by the difference in fuelling method.

Appendix C.2. Results of momentum balance analysis

Results of the interpretive toroidal angular momentum balance analysis using TRANSP for the same two high-power, $3.5\,\text{MA}$ pulses #94980 and #96713 are shown in Fig. C3 and Fig. C4. Torque densities $\tau\,[\text{Nm/m}^3]$ are shown in (a), radially integrated torques $T\,[Nm]$ in (b) and gyro-Bohm normalised momentum and ion heat diffusivities in (c).
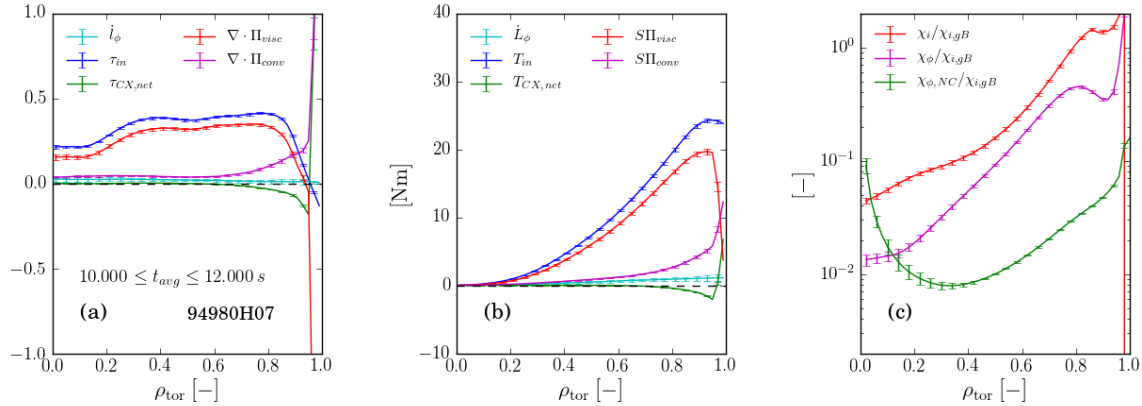

Figure C3: *Results of interpretive, momentum balance analysis using TRANSP of pulse #94980 (H07) showing: (a) input and net CX torque densities τ_{in} and $\tau_{CX,net}$, rate of change of angular momentum $\dot{l}_\phi$ and divergences of viscous and convected momentum fluxes $\nabla \cdot \Pi_{visc}$ and $\nabla \cdot \Pi_{conv}$; (b) the quantities shown in (a) volume integrated out to radius ρ_{tor}; (c) the ion thermal and momentum diffusivities, normalised to the ion-gyro-Bohm thermal diffusivity, i.e. $\chi_i/\chi_{i,gB}$ and $\chi_\phi/\chi_{i,gB}$, where the TRANSP profiles are averaged over the sustained ELMy H-mode phase ($10.0 \leq t \leq 12.0\,$s). The various terms in the momentum balance are explained in §Appendix B.1.*

The dominant source of input torque $T_{\phi,in} \sim 25 - 30\,\text{Nm}$ is from the NBI heating. Note that because of the more peaked density profile in pulse #96713, the torque density profile $\tau_{\phi,in}$ is somewhat more peaked than in pulse #94980, which is partly responsible for the increased toroidal rotation rate. Note that in both pulses, the rate of change of angular momentum $\dot{L}_\phi$ is small, i.e. there is a steady rate of toroidal rotation during the averaging period.

In the gas-fuelled pulse #94980, in which $T_i \sim T_e$, the momentum and ion diffusivities are very similar, i.e. the Prandtl number $Pr = \chi_\phi/\chi_i \sim 1$ except near the pedestal top. Except in the very core, both the ion thermal and momentum diffusivities are much larger than the ion-neoclassical level, i.e. $\chi_i/\chi_{i,NC}$ and $\chi_\phi/\chi_{i,NC} \sim \mathcal{O}(10)$ across the plasma.

As discussed further in §2.2, in pulse #96713 with the pellet+gas fuelling, the ion thermal diffusivity is slightly less than that for the electrons, $\chi_i/\chi_e \sim 0.8$, both remaining $\sim \mathcal{O}(10)\chi_{i,NC}$. However, there is a more significant reduction in χ_ϕ, with the Prandtl number below $Pr \lesssim 0.5$, particularly further into the core.
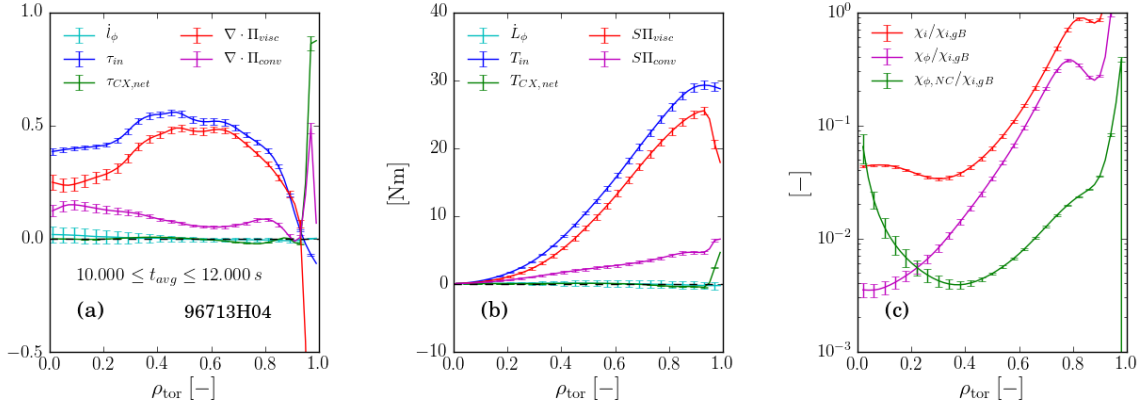
Figure C4: *Results of interpretive, momentum balance analysis using TRANSP of pulse #96713 (H04), where the TRANSP profiles are averaged over the sustained ELMy H-mode phase (10.0 ≤ t ≤ 12.0 s). The definition of the quantities plotted are the same as in Fig. C3.*

In the pedestal region ($\rho_{N,ped} \sim 0.96 \leq \rho_N \leq 1$), charge-exchange collisions with cold neutral D^0 atoms results in a radially-integrated, frictional torque $T_{\phi,CX(net)} \sim \mathcal{O}(10)\,\text{Nm}$, which opposes the torque imposed by the NBI. This torque $T_{\phi,CX(net)}$ is $\sim \times 1.5$ (and $\tau_{\phi,CX(net)} \sim \times 3$) higher in the gas-fuelled pulse #94980 than in the pellet+gas fuelled pulse #96713, primarily because the D^0 influx at the LFS is higher in the gas fuelled pulse.

The large CX torque density ($\tau_{\phi,CX(net)} \sim \mathcal{O}(1)\,\text{Nm}^{-2}$) necessitates a large negative viscous momentum flux $\Pi_{\phi,visc}$ across the pedestal to achieve momentum balance. This implies the presence of a strong momentum 'pinch' that can arise from neo-classical effects [75] and/or be driven by turbulence [76]. While the presence of this momentum pinch is worthy of more detailed study, it is beyond the scope of this paper.

Appendix D. Signal processing algorithm for estimating radiated power

We can decompose the fast bolometer signal P_{Rad}^{Hor} into low- and high-pass filtered components: P_{Rad}^{HP} and P_{Rad}^{LP}, with a common cutoff frequency of 10 Hz. By scaling the high-pass filtered signal P_{Rad}^{HP} by the ratio of the more reliable $\langle P_{Rad}^{man} \rangle$ signal from the tomographic reconstructions to the low-pass P_{Rad}^{LP} signal and adding the scaled signal to $\langle P_{Rad}^{man} \rangle$ we can construct a signal that retains the time response of the fast signal and also has the correct magnitude, i.e. $P_{Rad}^{Pl} = \langle P_{Rad}^{man} \rangle + (\langle P_{Rad}^{man} \rangle / P_{Rad}^{LP}) \times P_{Rad}^{HP}$. Note that in this expression, each binary arithmetic operation implies interpolation of the signal on the RHS of the operator onto that on the LHS, i.e. of the signal with the faster time base onto that with the slower time base.

Appendix E. Spectral measurements of ELM-sputtered Be and W influxes

Comparison of relative sputtered Be and W fluences Φ_{Be}^{ELM} and Φ_{Be}^{ELM} due to the different ELM types, as presented in §2.8, did not require calculation of absolute impurity influxes from the measured spectral line intensities. As explained in §Appendix E.1, such a calculation requires knowledge of the local T_e and n_e where the impurities enter the plasma to determine the number of ionised ions per detected photon. Such measurements are not available with sufficient temporal ($\mathcal{O}(10\,\mu s)$) and spatial ($\mathcal{O}(1\,cm)$) resolutions to determine absolute impurity influxes spectroscopically during the intra-ELM periods.

In §Appendix E.1 we explain how the relevant Be and W impurity line intensities are measured on JET-ILW and how these can be related related to the impurity influxes. Then, in §Appendix E.2, these measurements are used to determine an effective sputtering yield $\gamma_{Be^{4+} \to W}$ for the Be^{4+} ions incident onto the divertor W target material. The resulting yield data is the conditionally averaged according to the ELM type to investigate whether there is any difference between the averaged sputtering yield $\langle \gamma_{Be^{4+} \to W} \rangle$ between the pellet-triggered and natural ELMs.

Appendix E.1. Spectroscopic measurement of Be^+ *and* W^0 *influxes from the divertor targets.*

As explained in Ref. [64], when viewing perpendicular to an influx Γ_I [m^{-2}s^{-1}] of impurity ions I into a plasma, the intensity‡ of line emission I_γ [γm^{-2}sr^{-1}s^{-1})] emitted from a low ionisation stage with ionisation energy $E_{ion} << T_e$, is related to the influx by the relation:

$$\Gamma_I = 4\pi(S/XB)I_\gamma$$

, where the quantity S/XB is the ratio of the rate coefficients for ionisation S and excitation of the spectral line XB (X is the excitation rate of upper level and B the branching ratio). Provided the atomic data is available for the ionisations/photon S/XB, this provides a convenient means of measuring the impurity influx [65].

On JET-ILW a multi-channel, visible range spectrometer views the lower, divertor region of the vessel. The 20 lines of sight, which view both the inner and outer divertor targets, are shown in Fig. E1 (a). Light from this system is split between three arrays of fast, photomultiplier detectors, with band-pass, interference filters chosen to select particular, visible range spectral lines. Here, we use the Be II (527.9 nm) and W I (400.9 nm) lines for measurement of the Be^+ and W^0 influxes respectively.

In Fig. E1 (c,d), the intensity evolution of these two lines summed over channels viewing the HFS and LFS targets respectively, are shown during the occurrence of a single, type-I ELM. It is evident that there is a sharp increase in the impurity influx during the first $\sim \mathcal{O}(100\,\mu s)$ of the ELM crash, when the initial flux of hot electrons, with $T_e \sim T_{e,ped}$ expelled from the confined plasma by the ELMs, reaches the target. Following this initial sharp peak, there is a smaller influx on a timescale of $\sim \mathcal{O}(1\,ms)$, probably due to the incident ions, which reach the target on a slower, parallel transit time the SOL plasma, $\tau_{i,\parallel} \sim L_\parallel/c_s$, where $L_\parallel$ is the parallel connection length from the mid-plane to the target and c_s is the sound speed. The time period of a few *ms* encompassing the ELM duration, used for the time-integration of the intensity to determine the intra-ELM photon fluences Φ_γ is indicated in these figures.

‡ Strictly, in photometry this quantity is referred to as the spectral radiance, when expressed in units [W/m^{2}sr] [66]
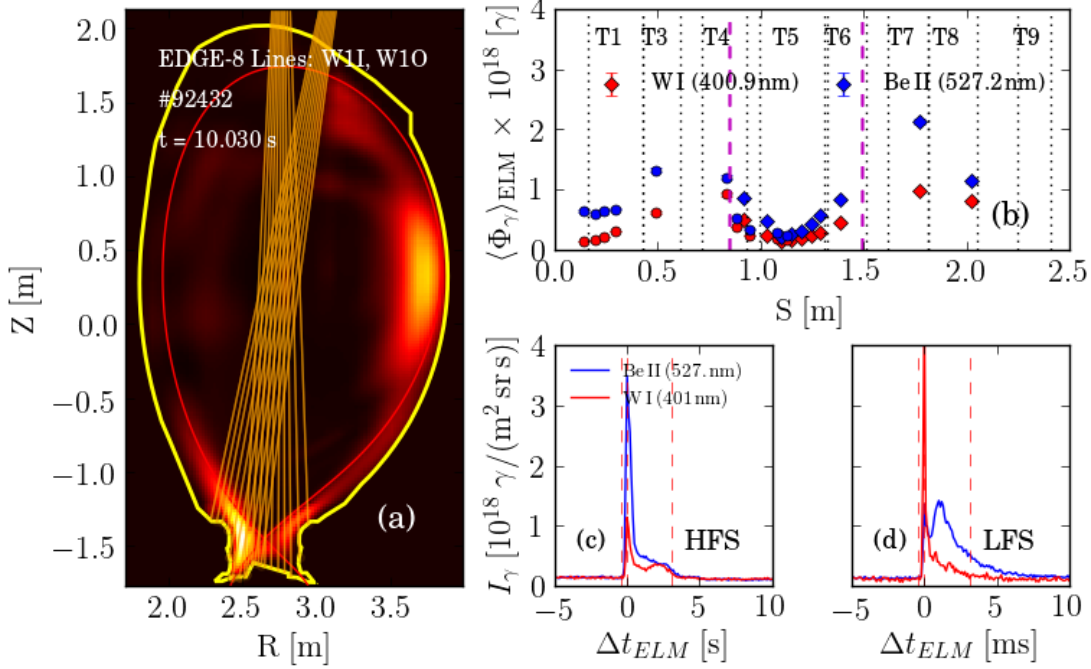
Figure E1: *Bolometric total radiation and spectroscopic impurity influx data for the high-power, 3 MA JET-ILW pulse #92432 showing: (a) tomographic reconstruction of total emissivity $\epsilon_m(R,z)$ at the peak of an ELM crash (t = 10.035 s) and lines of sight (LoS) of the multi-channel, visible range spectrometer system (KS3) viewing the divertor region (orange), where the intensity of the orange dots at the ends of the LoS represent the normalised W I (400.9 nm) line intensity detected by each channel; (b) intra-ELM photon fluences $\langle\Phi_\gamma\rangle$ averaged over the period $8.5 \leq t \leq 11$ s of the W I (400.9 nm) •and Be II (527.9 nm) •lines vs' the S-coordinate along the divertor target surface (the symbols indicate the LoS groups viewing the LFS (•) and HFS (♦) regions); and (c, d) time evolution over a single ELM of the intensity of the same Be II and W I lines summed over the channels viewing the inner (c) and outer (d) divertor regions. In (a) and (b), the vertical lines indicate the locations of the strike points (magenta-dashed) and divertor tile edges (black-dotted).*

Profiles of the intra-ELM photon fluences Φ_{Be}^{ELM} and Φ_W^{ELM} are shown in Fig. E1 (b) for the Be II (527.9 nm) and W I (400.9 nm) lines during the same ELM as shown in Fig. E1 (c, d) as a function of a coordinate S along the divertor targets. The locations of the strike points are also shown in Fig. E1 (b) (dashed) as are the edges of the divertor tile segments (dotted).

Note that in the corner-corner (C/C) magnetic configuration of these ITER-baseline pulses in JET-ILW, the outer strike point is located on tile #6 (T6), close to the divertor pumping throat. Hence, the outer strike point is hidden from view by the multi-channel spectrometer (see Fig. E1 (a)), which is consequently insensitive to the emission from any impurity influx close to the outer strike point, which is expected to be the main region of interaction during the inter-ELM periods.

It has been shown in Ref. [45], that type-I ELMs in JET-ILW extend far from the separatrix and interact with the full extent of the inner and outer vertical targets and 'domes' on the upper divertor surfaces, which are in fact dominant sources of impurity influxes during the ELMs. Previous studies of sputtered impurity sources at the divertor targets in JET-ILW using filtered visible imaging [49] have indeed shown that the time-averaged, ELM-sputtered

impurity influx is almost an order of magnitude larger than the inter-ELM influx at the strike points.

The contribution of visible Bremsstrahlung emission emitted from the relatively cold and dense SOL plasma in the divertor that is detected within the bandwidth of the interference filters can be estimated from the intensity detected by the lines of sight viewing the horizontal target tile #5 (T5), where there is very little interaction with the SOL plasma. It can be seen from Fig. E1 (b) that these channels (at $S \sim 1.2\,\mathrm{m}$) detect $\lesssim 10\%$ of that in the channels viewing the regions of maximum interaction with the ELMs, i.e. on the vertical targets and at the inner strike point.

Appendix E.2. Measurement of effective intra-ELM $Be^+ \to W$ *sputtering yield*

Although, we do not evaluate absolute impurity influxes over the divertor targets, we do evaluate the effective sputtering yield $\gamma_{Be^{4+} \to W}$ for the Be^{4+} ions incident onto the divertor W target material during the intra-ELM periods, as has been reported previously for H-mode plasmas in JET-ILW [50]. Note that it was also found in Ref. [50] that the time-averaged ELM-sputtered W influx was $\sim \times 18$ the influx during the inter-ELM periods.

By assuming that the flux of Be^{4+} ions incident onto the divertor W target during the ELMs is equal to the measured Be^+ influx Γ_{Be}, i.e. that there is no net Be re-deposition or erosion, the intra-ELM sputtering yield $\gamma_{Be^{4+} \to W}$ can be estimated by the ratio of the measured W^0 and Be^+ influxes, Γ_W and Γ_{Be}. Using Eq. (Appendix E.1) this can be evaluated from:

$$\gamma_{Be^{4+} \to W} = \frac{\Gamma_W}{\Gamma_{Be}} = \frac{(S/XB)_{WI}}{(S/XB)_{BeII}} \left[\frac{\Phi_W^{ELM}}{\Phi_{Be}^{ELM}} \right]$$

, where $(S/XB)_W$ and $(S/XB)_{Be}$ are the relevant values of ionisations/photon S/XB for the W I (400.9 nm) and Be II (527.9 nm) lines respectively.
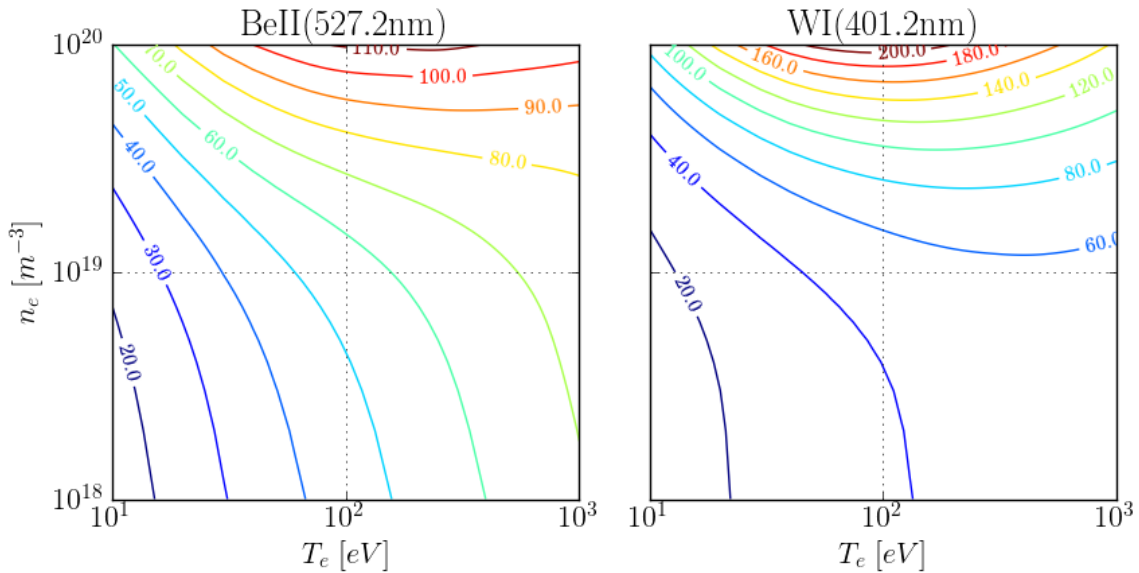

Figure E2: *Ionisations per emitted photon (S/XB) data for the visible* Be II (527.2 nm) *and* W I (400.9 nm) *emission lines as a function of* n_e *and* T_e *from the ADAS database of spectroscopic data [42,43].*

Values of S/XB for these lines from the ADAS database of atomic data [42] are shown in Fig. E2 as a function of T_e and n_e. For intra-ELM conditions, the values of S/XB used in Ref. [50] for the same W I (400.9 nm) and Be II (527.9 nm) lines at $T_e = 100$ eV are 53 and 58 respectively, giving a ratio of $(S/XB)_{WI}/(S/XB)_{BeII} = 0.91$. Here, we use the S/XB values from the ADAS database shown in Fig. E2 at $T_e = 100$ eV and $n_e = 10^{19}$ m^{-3} of $(S/XB)_{WI} = 46.7$ and $(S/XB)_{BeII} = 52.5$, giving a corresponding ratio 0.89.

Using this ratio $(S/XB)_{WI}/(S/XB)_{BeII} = 0.89$, effective sputtering yields $\gamma_{Be^{4+} \to W}$ can be evaluated from the average, intra-ELM photon fluences $\langle \Phi_W \rangle$ and $\langle \Phi_{Be} \rangle$ shown in Fig. E3 (a,b) for six 3 MA, high-power, ITER-baseline pulses in JET-ILW with ~ 30 MW of heating power, three with gas-fuelling alone and three with pellet+gas fuelling. The data are conditionally averaged according to the ELM type, i.e wither the ELMs are pellet-triggered or spontaneous 'natural' ELMs occurring in gas-only or pellet+gas fuelled pulses.

It can be seen from Fig. E3 (c), that the average, intra-ELM sputtering yields lie in the range $\langle \gamma_{Be^{4+} \to W} \rangle \sim 0.2 - 1.2$. These are consistent with the magnitudes shown for these yields in Fig. 9 of Ref. [50], in which the intra-ELM sputtering yield $\gamma_{Be^{4+} \to W}$ is plotted vs $T_{e,ped}$ for JET-ILW pulses. This plots shows that the measured yield $\gamma_{Be^{4+} \to W}$, which increases from 0.2 to 1.0 over the range $T_{e,ped} \sim 200 - 800$ eV, is larger than that possible for physical sputtering of W by Be^{4+} ions, which reaches a maximum of ~ 0.4 at $T_e \sim 400$ eV. It was
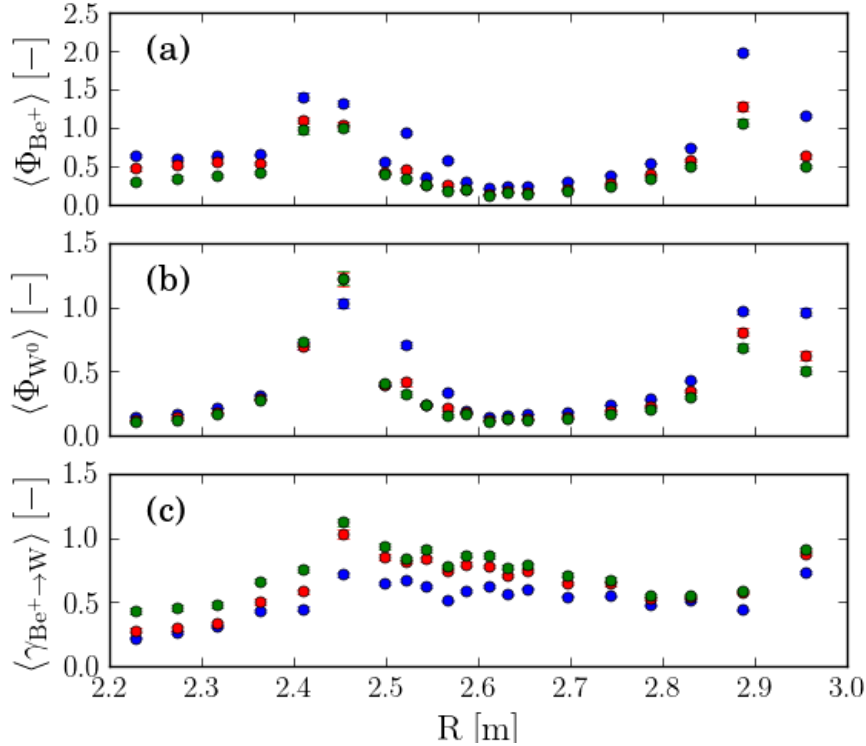

Figure E3: *Comparison of ELM-averaged profiles, as a function of the radius R where the line of sight intersects the divertor targets, from four high-power, 3 MA/2.8 T pulses with ~ 30 MW of heating power, showing: relative, intra-ELM photon fluences of (a) the Be II (527.9 nm) line $\langle \Phi_{Be} \rangle$ and (b) the W I (400.9 nm) line $\langle \Phi_W \rangle$ and (c) the effective sputtering yield $\langle \gamma_{Be^{4+} \to W} \rangle$. The data is conditionally averaged by ELM type, i.e. pellet-triggered (•) ELMs and natural ELMs (•, •) in pulses #92432 & #92433 with gas fuelling only (•) and pulses #92434 & #92436 with gas+pellet-fuelling (•).*

therefore concluded in Ref. [50] that some of the W influx is due to sputtering by the D^+ fuel ions. Ref. [50] also reported a total W influx from the outer target $\sim \times 1.8$ that of the influx from the inner target.

Note that ions at a temperature T_i, accelerated through the sheath potential $V_{sh} \sim 3T_e$ impact the target surface with energy $E_{inc} \sim T_i + 3ZT_e$. Hence, if fast the electron heat flux due to the ELMs cause T_e at the targets to reach $T_e \sim T_{e,ped}$, the D^+ ions will impact the target with energies $E_{inc} \sim 3T_{e,ped} \sim 2 - 3\,\mathrm{keV}$ [58]. At incident D^+ ion impact energies $E_{inc} \gtrsim 1\,\mathrm{keV}$, the yield for W sputtering $\gamma_{D+\to W} \gtrsim 2\%$ [57], so it is quite possible for the ELM-sputtered W influx due to D^+ ions to be comparable to that sputtered by the Be^{4+} ions of typical concentration $n_{Be}/n_e \sim 2\%$, i.e. the higher number of D^+ ions approximately compensates the relatively lower yield.

It is evident from Fig. E3 (c), there is typically little difference in the resulting yields $\langle \gamma_{Be^{4+}\to W} \rangle$ between the ELM types. Where the measured W I (400.9 nm) fluence is weak, there is significant contribution to the signal from bremsstrahlung emission, so the corresponding values of $\langle \gamma_{Be^{4+}\to W} \rangle$ overestimated there. Only at the inner target for the ELMs occurring during the pellet+gas fuelled pulses, are the values of $\langle \gamma_{Be^{4+}\to W} \rangle$ somewhat higher than for those during the gas-only fuelled pulses. This may be because $T_{e,ped}$ is higher in these pulses than in the gas-fuelled pulses but it is not clear why this should not also increase the sputtering yield at the outer target.

Influence of metastable populations on W^0 influx measurement: Although the Be II (Li-like) system does not contain significant metastable levels [67], the complex electronic structure of W^0 atoms has several, for which population balance is achieved on the excitation timescale. The W I (*400.9* nm) $(5d^5(6s)^7S_3 - 5d^5(6s)^7P_4)$ transition is excited from the $^7S_3$ metastable level $(E_{k_0} = 2951\,\mathrm{cm}^{-1}\ (0.366\mathrm{eV}))$ and hence provides a measurement of the influx of W^0 atoms in this metastable state. In principle, measurement of the total influx requires an independent spectroscopic measurement of the flux in each of the five other metastable states $(^5D_{0-4})$.

Laboratory measurements of an effective total ionisations/photon $((S/XB)_{eff})$ for the W I (*400.9* nm) line have been made by means of injection of a known influx of gaseous WF_6 into a tokamak plasma [68]. These measurements yield quite constant values of $(S/XB)_{eff} \sim 85$ for $T_e > 50\,\mathrm{eV}$. This value was found to be in good agreement with atomic physics GKU modelling [69], which assumed a Boltzmann distribution with effective temperature T_W for the metastable populations of the W^0 atoms. For the W I (*400.9* nm) line, these calculations yielded values $51 \lesssim (S/XB)_{eff} \lesssim 139$ over the range $0.1 \le T_W \le 2\,\mathrm{eV}$.

For the W I (*400.9* nm) line, the ratio of the experimental $(S/XB)_{eff} \sim 85$ from Ref. [68] and the value from ADAS assumed here of 46.7 is ~ 1.8. Hence, the yields $\gamma_{Be^{4+}\to W}$ derived here might well underestimate the actual yields by this factor, i.e. probably lie in the range $\gamma_{Be^{4+}\to W} \sim 0.4 - 2$. Hence, our conclusion that there must be significant sputtering of the W by the main D^+ ions remains valid.

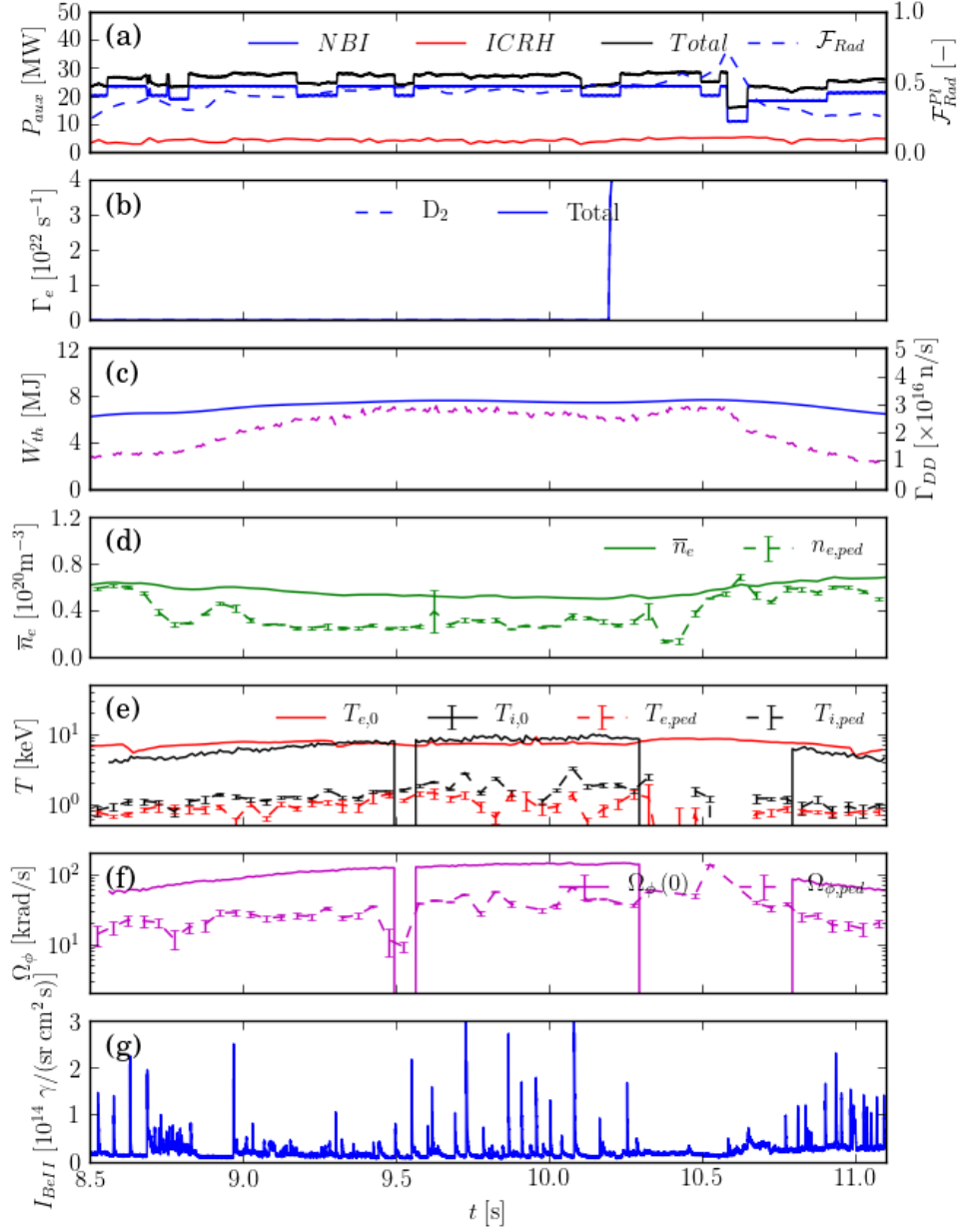## Appendix F. Evolution of $3\,\mathrm{MA}$ 'zero-gas' pulse #94662

Figure F1: *Evolution of $3\,\mathrm{MA}/2.85\,\mathrm{T}$ ITER-baseline scenario pulse #94662 with no fuelling from gas or pellets during the sustained H-mode phase, showing: (a) the total heating power P_{in} (black), from NBI P_{NB} (blue) and from ICRH (red) and the radiated power fraction $\mathcal{F}_{Rad} = P_{Rad}/P_{abs}$ (blue-dashed); (b) the D_2 gas fuelling rate Γ_{D2} [e/s] (solid); (c) total MHD stored energy W_{th} (solid) and the D-D neutron rate $\Gamma_{n,DD}$ [e/s] (dashed); (d) mid-plane, line-averaged density $\bar{n}_e$ (solid) and pedestal density $n_{e,ped}$; (e) the axial electron (red) and ion (black) temperatures $T_{e,0}$ and $T_{i,0}$ (solid) and pedestal temperatures $T_{e,ped}$ and $T_{i,ped}$ (dashed), (f) axial $\Omega_{\phi,0}$ (solid) and pedestal $\Omega_{\phi,ped}$ (dashed) toroidal rotation rates, (g) the ELM behaviour from a visible $\mathrm{Be\,II}$ line viewing the outer divertor target.*